Probing Heat Transport and Energy Conversion at the Atomic and Single Molecule Scale

by

Longji Cui

A dissertation submitted in partial fulfillment
of the requirements for the degree of
Doctor of Philosophy
(Mechanical Engineering)
in the University of Michigan
2018

Doctoral Committee:

Professor Edgar Meyhofer, Co-Chair
Professor Pramod Sangi Reddy, Co-Chair
Associate Professor Vikram Gavini
Professor Arun Majumdar
Professor Ctirad Uher

Longji Cui

longji@umich.edu

ORCID iD: 0000-0003-0469-3230

Acknowledgments

"What's past is prologue."

Over the course of five years I spent at Ann Arbor, I had the opportunity to meet and work with many people from whom I have learnt a lot. These people and the stories behind our interactions have truly shaped my perspective over research, life, and the world in general. Here I would like to acknowledge all of them, say goodbye to our shared journey, and sail off into the next adventure of my life.

First of all, I would like to thank my advisors Prof. Pramod Reddy and Prof. Edgar Meyhofer for offering me the opportunity to study at the University of Michigan. They parented me patiently to grow up from a naïve junior researcher and become a professional scientist and scholar with ambitious yet realistic goals. From many angles they are distinct from each other when working on science and because of that I consider myself extremely fortunate to have learned different ways to critically access and tackle scientific problems. I will remember numerous moments Pramod guided me with great optimism to take a leap of faith and fight my way through the seemingly endless dark tunnels in research. These research projects, all eventually taking me multi-year-long effort, would simply not have been possibly accomplished without his insights and mentoring. I will also remember many hours of time Edgar spent with me in the lab and his office, fixing malfunctioning instruments and circuits, giving me both moral support and guidance on debugging failing experiments, and teaching me a lot about

biophysics, English and western culture. I cherish these moments dearly in my heart. Both Pramod and Edgar supported me with a lot of advice and help during my search for a position in academia. Just like they are always role models to me, I shall try my best to be the same to the younger generation of researchers.

I had a lot of great memories interacting with my coworkers, colleagues and collaborators in the past five years. I would especially like to thank Kyeongtae Kim, Woochul Lee and Bai Song for all that they taught me about being an experimentalist in the beginning of my PhD. I sincerely thank Wonho Jeong, Sunghoon Hur, Ruijiao Miao, Dakotah Thompson, Kun Wang, and Chang Jiang for our close collaboration on various projects. They not only shared my loneliness when working on these difficult experiments but also contributed concretely to our final victory in achieving our goals. I have also been very fortunate to collaborate with many great researchers from all around the world outside of U-M. I would like to thank Prof. Juan Carlos Cuevas, Linda Angela Zotti, Victor Fernandez-Hurtado, Prof. Fabian Pauly, Prof. Peter Nielaba, Manuel Matt, Jan C. Klöckner, Johannes Feist, Prof. Francisco J. Garcia-Vidal, Prof. Sung-Yeon Jang and Zico Junior, for their significant contribution to my research. It would be impossible to get to this point without them. My lab life would be so colorless without my fellow labmates over the years. I would like to thank Seid Sadat, Youngsang Kim, Yashar Ganjeh, Anthony Fiorino, Andrej Lenert, Linxiao Zhu, Ahmet Mazacioglu, Rohith Mittapally, Shen Yan, and Amin Reihani for our shared memory working and laughing in the lab.

I would like to thank many people for the interaction I had with them have indeed made a difference in me in many ways. I thank my committee members, Prof. Vikram Gavini, Prof. Ctirad Uher, and Prof. Arun Majumdar, for taking their time and offering insightful suggestions to improve my research and thesis. I would also like to thank Prof. Xiaogan Liang and Prof. Phil

Roe for sharing their own experience and giving me a lot of advice from both academic and non-academic viewpoints since the beginning of my PhD. I have also found great friendship with many fellow students at Ann Arbor outside of my lab life some of them being Yushu Ma, Chen Li, Shantonio Birch, Daning Huang, Da Li, Lu Wang, Yun Han, Yan Chang and Jian Shi. I thank them for their companionship that definitely made my lengthy PhD life less suffering and even joyful.

My acknowledgement ends with the words I have to my family – my parents and my wife Ju. Their love has harbored me through thousands upon thousands of days and nights across the Pacific Ocean. None of what I have done will be possible or meaningful without them being with me on this journey. I dedicate this thesis to them.

Table of Contents

List of Figures

Abstract

The study of heat transport and energy conversion constitutes an important subject in modern physics and engineering research. The widely-applied Fourier's and Planck's laws have proven to be very useful to describe heat transport via conduction and radiation for macroscale devices and materials. However, at the nanoscale, recent studies have highlighted the breakdown of these laws and important deviations from the macroscale physical pictures. Understanding these emerging properties of thermal energy transport and conversion at the nanoscale is of great fundamental interest, and is expected to be crucial to developing a variety of technologies ranging from nanoelectronics, photonics, to thermoelectrics and photovoltaics. Unfortunately, in contrast to the extensive studies of optical and electronic properties at the nanoscale, the thermal properties of materials and devices ranging in size from the atomic and single-molecule scale to the realm of a few nanometers, have remained largely unexplored due to the challenges in performing experiments with desired resolution.

My research aims to overcome these technical challenges by developing a series of experimental techniques and leveraging them to systematically answer a number of long-standing open questions. These questions include, i) How is heat conducted in atomic-sized objects such as single-atom junctions and single molecules? What are the general heat transport characteristics and microscopic mechanisms at the atomic scale? ii) How is heat converted to electrical energy at the atomic and single molecule level via thermoelectric effects? *Vice versa*,

can we observe the conversion of electrical to thermal energy (heating or cooling) at the fundamental limit of any physical devices? iii) How is thermal energy transferred radiatively in Ångström- to nanometer-sized gaps between surfaces?

To study heat transport in atomic-sized junction, we custom-fabricated extremely sensitive calorimetric scanning thermal microscopy probes with picowatt resolution. These probes enabled us to perform measurements of thermal transport in metallic (gold and platinum) wires only single- or few-atom wide. These measurements enable the first-ever observation of quantized thermal transport at room temperature in single-atom junctions, i.e., the measured thermal conductance is at values corresponding to the multiple integers of universal thermal conductance quantum ($\pi^2 k_B^2 T/3h$, where k_B is the Boltzmann constant, T is the absolute temperature and h is the Planck constant). With these measurements, we were also able to validate the Wiedemann-Franz law, which relates electrical to thermal conductivity of metals at the macroscale and signifies the nature of electron transport, all the way down to the single-atom limit with high accuracy. Furthermore, applying these highly sensitive probes, we performed experiments to quantify heat transport in single molecule junctions to study how phonons transport heat at the molecular limit. Using alkanedithiol molecules of varying length as a prototypical system, we have found that phonon transport in single molecule junctions is ballistic in nature, nearly independent on the molecular length.

Moreover, we developed a unified experimental platform with which multiple transport properties, including energy dissipation, electrical conductance, and Seebeck/Peltier effects, can be measured for various molecular structures and nanomaterials. By leveraging this platform, we have demonstrated molecular scale refrigeration (net cooling) phenomena based on the Peltier effect. We found that by altering the structure of an organic molecule by a few atoms the cooling

characteristics could be dramatically modulated, indicating the intimate relationship between the energy dissipation properties and the electron transmission characteristics in single molecular junctions. Moreover, with nanofabricated STM-based stiff scanning thermal probes, we investigated radiative heat transfer at the atomic scale, i.e. in gaps between two surfaces approaching a few nanometers down to ~2 Ångströms. In this regime, classical Planck's law for blackbody radiation breaks down, giving rise to a dramatically enhanced radiative heat flux. We measured heat flux and found that thermal radiation in nanometer gaps indeed increase, via near-field thermal electromagnetic effects, by several orders of magnitude. Our observations agreed well with the predictions of fluctuational electrodynamics. The experimental techniques and approaches presented in this dissertation set the stage for future explorations of thermal and electrical properties of a broad range of atomic and molecular materials, low dimensional structures, and emerging nanoscale devices.

Chapter 1: Overview and Outlook

1.1 Overview

Atomic-scale structures represent the ultimate limit to miniaturization of any physical devices. The demand for faster and more affordable computing and storage capability has advanced the modern electronics industry over the past half century to continuously shrink individual electronic components such as transistors to the atomic size. Whereas in macroscopic world classical laws can effectively approximate physical phenomena while geometry changes, numerous physical laws have to be modified or rewritten at the fundamental limit (into the quantum regime). Being regarded as a formidable challenge to continue applying well-applied rules and framework, but also an exciting opportunity to enable potentially revolutionary functionalities, the study of transport properties at the atomic scale is of fundamental interest, and hold great promise to improve and transform a variety of contemporary technologies. To date there have been tremendous amount of studies directed towards resolving optical and electrical transport properties and mechanisms in atomic-sized structures and devices. Although central to our understanding of the functionalities and performance of materials, thermal properties at the atomic scale have so far been barely studied. This is mainly due to the fact that relevant thermophysical quantities such as heat flow, energy conversion and dissipation are not readily measurable parameters at such small spatial regime. Developing novel experimental techniques and approaches to characterize heat transport and energy conversion characteristics at the atomic scale arises to be the key challenge in this field.

This dissertation presents the effort to overcome these experimental challenges and enabled the systematic exploration of thermal transport and energy conversion properties of several model physical systems at the atomic scale, including metallic atomic junctions, molecular junctions, and atomic-sized gaps.

In Chapter 2, we present a detailed introduction to and review of both the theoretical and experimental studies of heat transport and energy conversion at the atomic scale, focusing on the studies of atomic and molecular junctions. We summarized the fundamental physical mechanisms of Landauer picture, a theoretical framework to understand energy (thermal and electrical) transport and conversion in the quantum regime. Subsequently, we reviewed the theoretical and experimental progress on our current understanding of thermoelectric effects, thermal conduction, heat dissipation and local heating/cooling in atomic and molecule junctions. We concluded the review by discussing some open challenges and potential directions for future investigation of atomic and molecular scale thermal transport and energy conversion.

In Chapter 3, we report the observation of quantized thermal transport in individual atomic junctions and chains. Probing thermal transport in junctions of atomic dimensions is crucial for understanding the ultimate quantum limits of energy transport. These limits have been explored in a variety of microdevices where it has been shown that, irrespective of the nature of the carriers (phonons, photons and electrons), heat is ultimately transported via discrete channels. However, observations of quantum thermal transport in micro-scale devices were only possible at sub-Kelvin temperatures and other attempts at higher temperature regimes have yielded inconclusive results. In this regard, atomic junctions offer a unique opportunity to explore whether thermal transport can still be quantized at room temperature. Here, by employing novel, custom-fabricated, picowatt-resolution calorimetric scanning probes, we measure the thermal

conductance of gold and platinum metallic wires down to single-atom junctions. Our work reveals that the thermal conductance of gold single atom junctions is quantized at room temperature and shows that the Wiedemann-Franz law relating thermal and electrical conductance is satisfied even in single-atom contacts. Furthermore, we quantitatively explain our experimental results within the Landauer picture for quantum coherent thermal transport.

Following along the line of Chapter 3, Chapter4 presents my ongoing work of quantifying thermal transport in single molecule junctions. Single molecule junctions and chains are paradigmatic platforms to unravel novel charge and energy transport phenomena at the fundamental molecular limit. Recent works have successfully probed a variety of transport properties at the single molecule level such as electrical conduction, light emitting, thermoelectricity, quantum interference, and Joule heating. Although central to our understanding of energy transport and conversion at the nanoscale, heat conduction in single molecule junctions has so far eluded direct detection due to experimental challenges. Moreover, both recent experimental studies and theoretical modeling of heat transport in molecular junctions has yield inconclusive and even contradictory results/predictions. Here, by employing custom developed calorimetric scanning thermal microscopy probes with picowatt resolution, we quantitatively measure the thermal conductance of single molecule junctions and identify the dependency of thermal transport on molecular length. Specifically, our experimental studies, performed in prototypical Au-alkanedithiol-Au junctions, reveal that thermal transport in single molecule junctions is ballistic, nearly independent on the molecular length. The experimental technique and methods presented in this work set the benchmark for systematic studies of single molecule thermal transport and energy conversion, which is crucial to address numerous fundamental questions that have remained experimentally inaccessible.

In Chapter 5, we demonstrated the Peltier cooling effect in molecular junctions. Recent experimental progress in probing the thermopower (Seebeck effect) of molecular junctions has enabled studies of the relationship between thermoelectricity and molecular structure. However, observation of Peltier cooling in molecular junctions—a critical step for establishing molecular-based refrigeration—has remained inaccessible. By integrating conducting probe atomic force microscopy with custom-fabricated picowatt-resolution calorimetric microdevices, we created an experimental platform that enables the unified characterization of electrical, thermoelectric, and energy dissipation characteristics of molecular junctions. Using this platform we studied prototypical molecules (Au-Biphenyl-4,4'-dithiol-Au, Au-Terphenyl-4,4''-dithiol-Au, and Au-4,4'-Bipyridine-Au) and revealed the relationship between heating or cooling and charge transmission characteristics. Our experimental conclusions are supported by self-energy corrected density functional theory calculations.

In Chapter 6, we reported the experimental study of radiative heat transfer at the atomic scale, i.e. for gap-sizes of a few Å to 5 nm, performed under ultra-high vacuum conditions between a stiff Au-coated probe featuring embedded Cr-Au thermocouples and a heated planar Au substrate. Past measurements performed in ultra-high vacuum conditions showed large apparent near-field conductances that are larger than the predictions of state-of-the-art fluctuational electrodynamics calculations by more than three orders of magnitude. In order to understand the source of this discrepancy we systematically studied extreme near-field radiative heat transfer after subjecting Au surfaces to various surface cleaning procedures. We found that insufficiently cleaned samples lead to unexpectedly large thermal conductances and feature a small apparent tunnel barrier height (1 eV) suggesting the presence of surface contamination. When the probe and substrate were systematically cleaned following protocols involving plasma-

cleaning/locally crashing the tip into the substrate the apparent barrier heights were found to increase to values as large as 2.5 eV and the observed near-field conductances decreased to extremely small values—below the detection limit of our probe—as expected by our computational results. Our results show that surface contaminants, that confound the interpretation of near-field radiative heat transfer measurements, can be reproducibly eliminated paving the way for systematic future studies.

1.2 Outlook

As an outlook of this dissertation, the novel experimental techniques and approaches presented here pave the way for numerous avenues of future research to understand energy transport and conversion properties of a broad range of nanomaterials, low dimensional structures and devices. Below I will discuss a couple of examples that applying these techniques would make further impact on thermoelectric and heat transport studies.

A central challenge in the study of thermoelectrics is to look for materials with high thermoelectric figure of merit *ZT*, a dimensionless number defined to be equal to $S^2 G_e T / G_{th}$, where *S*, G_e and G_{th} represent the Seebeck coefficient, electrical and thermal conductances, respectively. Mostly used thermoelectric material, Bismuth telluride, possesses a ZT of approximately one, which corresponds to less than 20% of Carnot efficiency in energy generation applications, significantly lower than the thermal efficiency of traditional energy conversion technologies such as internal combustion engine. A *ZT* higher than 3 is necessary to enable the conversion of wasted thermal energy to electricity with similar efficiency as traditional in technologies, especially at around room temperature. In the pursuit of high-ZT thermoelectric materials, a fundamental question that has not been well addressed is that how high the thermoelectric energy conversion efficiency can be for nanoscale and molecular scale

systems. The promise is that in nanoscale and molecular materials thermoelectric energy conversion can be boosted by quantum effects that have no classical analogues. Recent theoretical studies have demonstrated extremely high *ZT* in specially designed molecular junctions due to quantum interference effect. The key issue here is that how we can design proper experimental technique to validate these theoretical proposals. Specifically, can we observe the predicted high thermoelectric energy conversion in special molecular systems? How can we rationally design the chemical structure of molecules to enhance selected transport properties of a molecule and simultaneously suppress others? These are the sets of fundamental questions that we need to address before proceeding to demonstrate system level thermoelectric energy conversion devices for various applications.

The capability of measuring picowatt-level heat current using scanning thermal probe microscopy will also enable a deep understanding of energy transport mechanisms in various atomic- and nanometer-scale systems. One puzzling question regarding heat transport at the atomic scale is about how thermal radiation and heat conduction coexist, when two surfaces (with different equilibrium temperatures) are extremely close to each other, but not in direct contact. Numerous studies in the field of near-field radiative heat transfer have shown that near-field thermal effects emerge and increase monotonically when the distance between two surfaces are less than the thermal wavelength (~ 10 microns at room temperature). On the other hand, it has long been suspected that long wavelength acoustic phonons will propagate through vacuum, analogues to photon and electron tunneling in vacuum, when two surfaces are close enough. The crossover regime of near-field thermal radiation to phonon heat conduction is of particular interest in this regard. The questions that we can ask include: How does "phonon tunneling" behave in vacuum gaps? Is there an upper limit of near-field heat transport and how large that

would be compared to the contribution to thermal transport due to phonon conduction? Where does the transition from thermal radiation to heat conduction happen? How does the appearance of transition depend on the material properties such as composition, temperature, crystalline structure, and others? Theoretically a number of competing models have been proposed to answer these questions. To resolve this issue, experimental challenges such as measuring minute heat flow and maintaining sub-nanometer vacuum gaps have to be first overcome. In light of our recent development of techniques and experiments performed on both heat conduction and radiative heat transfer at the atomic scale, we believe the first sets of experiments to answer these above questions are feasible and would provide significant insight into our understanding of energy transport from both phonons and photons at their fundamental limit.

Chapter 2: Heat Transport and Energy Conversion at the Atomic and Molecular Scale: From Theory to Experiment

Sections 1.1 through 1.7 are reproduced with permission from *Journal of Chemical Physics*. See Ref.[1]

Longji Cui, Ruijiao Miao, Chang Jiang, Edgar Meyhofer and Pramod Reddy

2.1 Abstract

With the advent of molecular electronics in which the dimensions of devices and circuits are pushed to the technical limit of miniaturization, namely the atomic scale, tremendous attention has been paid towards understanding the structure-function relationship of atomic and molecular junctions. Understanding how heat is transported, dissipated, and converted into electricity in these atomic-sized junctions is of great importance for designing thermally robust molecular circuits and high-performance energy conversion devices. Further, the study of thermal and thermoelectric phenomena in atomic-sized junctions provides novel insights into the limits of applicability of classical laws. Here, we present a review of the computational and experimental progress made in probing thermoelectric effects, thermal conduction, heat dissipation and local heating/cooling in atomic and molecule junctions. We also discuss some outstanding challenges and potential future directions.

2.2 Introduction

The idea[2] of building electrical components and interconnects using single molecules has greatly inspired researchers over the past several decades and led to the emergence of the field of "molecular electronics". Transport characteristics of junctions of molecules between electrodes (Fig. 2.1), called Atomic and Molecular Junctions (AMJs), have been extensively explored to investigate the feasibility of creating molecular devices with desirable transport characteristics. Both experimental and theoretical work has shown that AMJs can indeed be employed to achieve unique and interesting charge transport characteristics.[3, 4, 5, 6, 7, 8, 9, 10] Owing to technical and computational advancements over the last decade, energy (thermal) transport and conversion properties of AMJs have attracted considerable attention.[11, 12, 13, 14, 15, 16, 17] Fundamentally, probing thermal transport in AMJs is useful to understand the limits to the applicability of classical theories at the nanoscale. Moreover, such studies are also essential for future practical applications of AMJs in electronic devices and for developing high-efficiency energy conversion devices. For example, it has been computationally proposed that by carefully designing AMJs, it is possible to achieve very efficient thermoelectric energy conversion.[18, 19, 20, 21] Furthermore, single molecular chains are also expected to feature ultrahigh thermal conductivities, in strong contrast to the relatively poor thermal conductivity of polymer materials,[22, 23] indicating that a more detailed understanding of thermal transport in such molecules may enable the creation of polymer based materials with high thermal conductivity.

In this chapter, we review current understanding of thermal and thermoelectric properties of AMJs. Insights obtained from both theoretical and experimental investigations of both self-assembled monolayer (SAM) based and single molecule based AMJs will be described. This chapter is organized as follows: in Sec. 2.3, we briefly introduce the Landauer formalism that is

used to describe transport in AMJs; subsequently in Sec. 2.4, we review the theoretical and experimental advancements in studying thermoelectric effects in AMJs; in Sec. 2.5, recent work on heat conduction, heat dissipation and local heating/cooling of AMJs will be discussed. Finally, we conclude by highlighting some open questions in the field.

2.3 Landauer Theory of Quantum Transport

2.3.1 Electrical conductance

Landauer's seminal work[24] which relates electrical conductance to electron transmission is widely used for describing transport in AMJs.[25, 26, 27] Within the Landauer formalism (Fig. 2.1(b)), the electrical current (I) at finite bias (V), is given by[27]

$$I = \frac{2e}{h} \int_{-\infty}^{+\infty} (f_L - f_R)\tau(E)dE \tag{1}$$

where $f_{L/R}$ is the Fermi-Dirac distribution of the left/right electrodes and $\tau(E)$ is the energy (E) dependent transmission function, which describes the probability of electron transmission through the AMJ. Under the small-bias and low-temperature approximations, Eq. (1) can be simplified to yield $I/V = G_e = (2e^2/h)\tau_{E=E_F}$, where E_F is the Fermi energy (chemical potential). Interestingly, for one fully open channel ($\tau_{E=E_F} = 1$), the electrical conductance is given by $G_e = G_0 = 2e^2/h = 1/(12.9k\Omega)$, which is the quantum of electrical conductance.

2.3.2 Seebeck Coefficient

The thermoelectric properties of AMJs can also be described within the Landauer formalism (Fig. 2.1(c)). Specifically, when a temperature difference (ΔT) is applied across a AMJ, an open-circuit voltage (ΔV) develops across the junction (Fig. 2.1(c)). The Seebeck coefficient (S) is given by $S = -\Delta V/\Delta T$ and can be related to the transmission function by[28, 29]:

$$S = \frac{\pi^2 k_B^2 T}{3|e|} \frac{\partial \ln(\tau(E))}{\partial E}\bigg|_{E=E_F} \tag{2}$$

It is clear from the above expression, which is valid if the transmission function is smooth and slowly varying on over an energy range of ~k_BT around E_F, that the slope of the transmission function at E_F determines the sign and magnitude of the Seebeck coefficient.

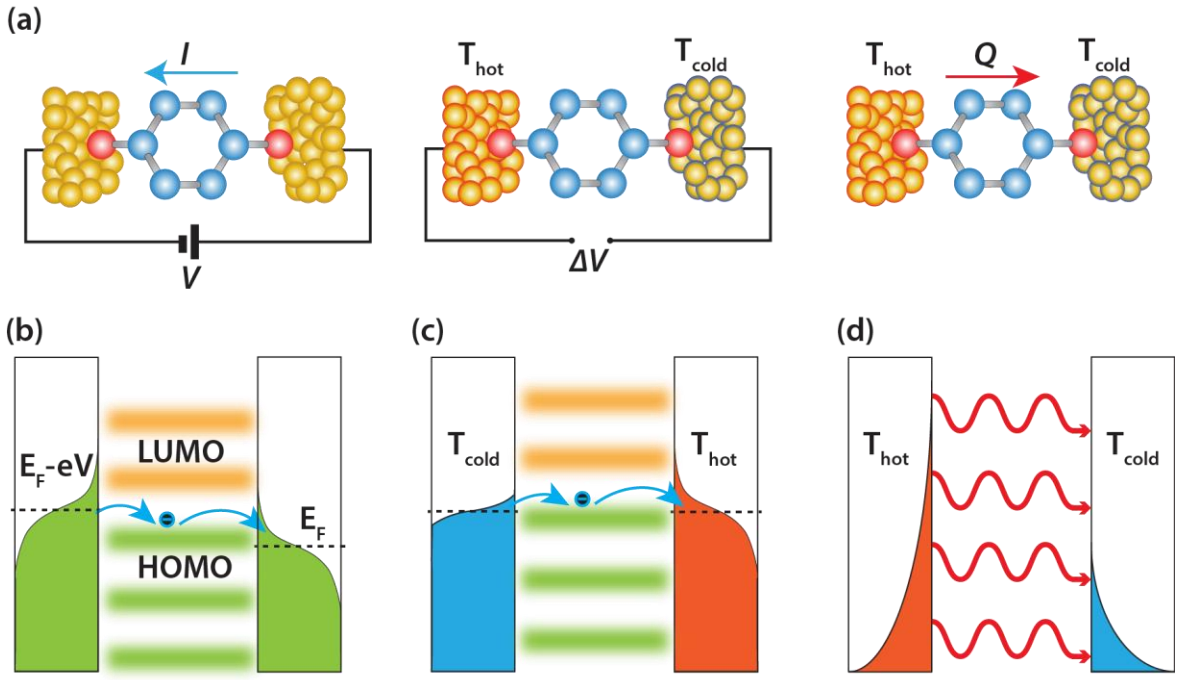

Figure 2.1: Schematics describing charge, thermoelectric and heat transport in atomic and molecular junctions (AMJs).
(a) An organic molecule in bridged between two electrodes to form a single AMJ. Left: electrical conductance measurement scheme. Middle: thermoelectric (Seebeck coefficient) measurement scheme. Right: thermal conductance measurement scheme. (b) Electric currents in a AMJ are driven by a difference in the Fermi-Dirac distributions in the electrodes arising from an applied bias (V). (c) Thermoelectric transport under a temperature difference. The sign of the Seebeck coefficient (S) is determined by the alignment of the HOMO and LUMO levels of the AMJ with respect to the Fermi level of the electrodes. HOMO: highest occupied molecular orbital; LUMO: lowest unoccupied molecular orbital. (d) Heat transport due to phonons when a temperature differential is applied to the electrodes, the Bose-Einstein distributions for phonons in the hot and cold electrodes are shown as red and blue shaded region, respectively.

2.3.3 Thermal Conductance

Thermal transport through AMJs (Fig. 2.1(d)) can also be described within the Landauer formalism. The electronic heat current ($J_{electrons}$) and the phononic heat current ($J_{phonons}$), when a temperature difference ΔT is applied, are given by[24, 30]

$$J_{electrons} = \frac{2}{h}\int_{-\infty}^{+\infty}(E - E_F)(f_L - f_R)\tau(E)dE \quad (3)$$

and

$$J_{phonons} = \int_{0}^{\infty}(h\upsilon)(g_L - g_R)\tau_{ph}(\upsilon)d\upsilon \quad (4)$$

where υ is the phonon frequency and $\tau_{ph}(\upsilon)$ is the transmission function for phonons and g_L and g_R denote the Bose-Einstein distributions for the left and the right thermal reservoirs respectively and depend on the temperature of the electrodes.

2.3.4 Energy (Heat) Dissipation

When a voltage bias V is applied across a AMJ, it results in both an electrical current (I) and heat dissipation in the junction. Within the Landauer approach it can be shown that when the heat dissipation in the molecular region is negligible, i.e. when transport is elastic, the heat dissipation in the left and right electrodes, Q_L and Q_R, respectively, are given by[31, 32]

$$Q_L = \frac{2}{h}\int_{-\infty}^{+\infty}(\mu_L - E)(f_L - f_R)\tau(E)dE \quad (5)$$

and

$$Q_R = \frac{2}{h}\int_{-\infty}^{+\infty}(E - \mu_R)(f_L - f_R)\tau(E)dE \quad (6)$$

where $\mu_{L/R}$ represent the chemical potentials of the left/right electrodes respectively.

In the next section, we describe thermoelectric phenomena in AMJs. We begin by describing the reasons why thermoelectric properties of AMJs are interesting. Subsequently, we describe theoretical and computational studies that highlight the potential of AMJs for thermoelectric energy conversion. Finally, we describe currently available experimental techniques and the progress to date in probing thermoelectric effects of AMJs.

2.4 Thermoelectrics in Molecular Junctions

Thermoelectric materials have long been employed as solid-state heat engines that convert heat into electricity. The energy conversion efficiency is represented by a dimensionless quantity called the figure of merit (ZT) which is defined as $ZT = S^2\sigma T/\kappa$, where S is the Seebeck coefficient (also called thermopower), σ is the electrical conductivity, κ is the thermal conductivity and T is the absolute temperature. Analogous to bulk materials, the efficiency of a AMJ in converting heat into electricity is quantified by

$$ZT = \frac{S^2 G_e T}{G_{th}} \tag{7}$$

where G_e and G_{th} represent the electrical and thermal conductances, respectively. The energy conversion efficiency (η) of a AMJ monotonically increases with ZT and is given by:

$$\eta = \eta_C \frac{\sqrt{1+ZT}-1}{\sqrt{1+ZT}+\frac{T_C}{T_H}} \tag{8}$$

where T_H and T_C are the temperature of the hot side and the cold side, respectively, and $\eta_C = 1 - T_C/T_H$ is the Carnot efficiency which represents the upper limit to energy conversion efficiency that any heat engine can achieve. It can be seen from Eq. (8) that achieving high

energy conversion efficiency requires a large *ZT* which in turn can be obtained if AMJs feature a large thermopower and electric conductance, and a small thermal conductance. Given the results in Eq. (1), Eq. (2) and Eq. (7) it is clear that large values of *ZT* can be achieved if AMJs simultaneously feature a large value of $\tau(E)$ and a large gradient of the transmission at the chemical potential (E_F).

2.4.1 Theoretical results

One of the first works to explore thermoelectric properties in AMJs was by Paulsson and Datta[29] where they analyzed the thermoelectric current and voltage of benzenedithiol (BDT) based AMJs. Their findings suggested that the thermoelectric current and voltage output of BDT AMJs were large enough to be measured and insensitive to the molecule-electrode coupling details. Further, their work suggested that the relative position of the HOMO (highest occupied molecular orbital) and LUMO (lowest unoccupied molecular orbital) with respect to the Fermi energy plays an important role in determining the sign of the Seebeck coefficient, indicating that thermoelectric measurements of AMJs can reveal important information about the electronic structures of AMJs.

Subsequently, several groups theoretically studied the thermoelectric properties of AMJs to explore the feasibility of achieving high *ZT*.[18, 19, 29, 33, 34, 35, 36, 37, 38, 39, 40, 41, 42, 43, 44, 45, 46] For example, Finch *et al.*[18] presented a computational study for CSW-479-bipyridine AMJs with gold electrodes (Fig. 2.2(a)). They showed that by tuning the orientation of a side group with respect to the molecular backbone, the thermopower could be dramatically enhanced, resulting in a large *ZT* value. They attributed this enhancement to Fano resonances[47], which arise from the presence of degenerate energy levels in the molecular backbone and the side groups.

Specifically, they found that the transmission function showed a peak, which was shifted towards the Fermi energy by controlling the angular orientation of the side group.

Bergfield *et al.*[19] investigated polyphenyl ether (PPE) molecules bridged between gold electrodes (Fig. 2.2(b)). Their work suggested that a sharp peak in the transmission function near the Fermi energy could arise from quantum interference effects[42, 48, 49], and thus could lead to a large Seebeck coefficient. Further, they showed that by increasing the number of phenyl rings in the molecule, very high values of *ZT* (> 4) were achievable.

Besides modifying the shape of transmission function by means of quantum interferences, recent work has also found that spin-crossover could be used to tune the charge transport[50, 51, 52] and thermoelectric properties[53] of molecule-ferromagnetic metal junctions. For example, Ghosh *et al.*[53] studied a spin-crossover molecule Fe(2-(1H-pyrazol-1-yl)-6-(1H-tetrazole-5-yl)pyridine)$_2$ ([Fe(L)$_2$]) which has a sharp transition from a low-spin (LS) state to a high-spin (HS) state upon elevating the temperature of the junction, and both spin and electron contributed to the thermoelectric current. In this work, *ZT* for the HS state (at 350 K) was found to be 4 times higher than the *ZT* for the LS state (at 250 K).

Vacek *et al.*[21] studied thermoelectric properties in helicene AMJs when the helical shaped junctions are mechanically stretched or compressed (Fig. 2.2(c)). Their calculations showed that when the molecular junction is compressed, a significant enhancement of electrical conductance and a sign-change in thermopower, originating from the change in the overlap of the wave functions of nearest atoms is expected along with a concomitant increase in *ZT*. Upon stretching, the *ZT* value was found to first decrease and subsequently increase. They suggested that the idea of mechanically controlling electric conductance and thermopower could also be applied to other

non-planar shaped molecules including cycloparaphenylenes, cyclacenes, ball-like molecules, carbon cages, tailored fullerenes, fullerene cages and short DNA molecules.

As described above several computational studies have suggested that it may be feasible to perform thermoelectric energy conversion at efficiencies close to the Carnot limit (i.e. very high values of *ZT*). However, it is well know that operation close to the Carnot limit implies operation and the reversible limit and therefore, the power output is negligible. In practice, as has been highlighted in recent works[45, 54, 55], it is essential to understand the relationship between efficiency and power output under irreversible conditions. The Curzon-Ahlborn (CA) limit, which describes the thermodynamically maximum efficiency of a heat engine operating under conditions where the power output is maximized, is therefore of great interest. The maximum efficiency of a heat engine operating at maximum output power is given by, $\eta_{CA} = \frac{\eta_C}{2} + \frac{\eta_C^2}{8} + O(\eta_C^3) + \cdots$where η_{CA} (η_C) is the Curzon-Ahlborn (Carnot) efficiency. To achieve this maximum output power, the transmission function of AMJs has to be rationally designed.

In this regard, Nakpathomkun *et al.*[20] studied a low-dimensional system with an approximately Lorentzian shape transmission function, which is given by

$$\tau(E) = \frac{\frac{\Gamma^2}{2}}{(E - E_0)^2 + \frac{\Gamma^2}{2}} \tag{9}$$

where E_0 is the center position of the Lorentzian and Γ is the full width at half of maximum of $\tau(E)$. They showed that by carefully choosing Γ and the relative position of E_0 and E_F, the output power can be optimized. However, they also showed that the Curzon-Ahlborn limit can

not be reached with a Lorentzian shaped $\tau(E)$ due to the low-energy tail, which permits a detrimental electric current in a direction opposite to the thermoelectric current.

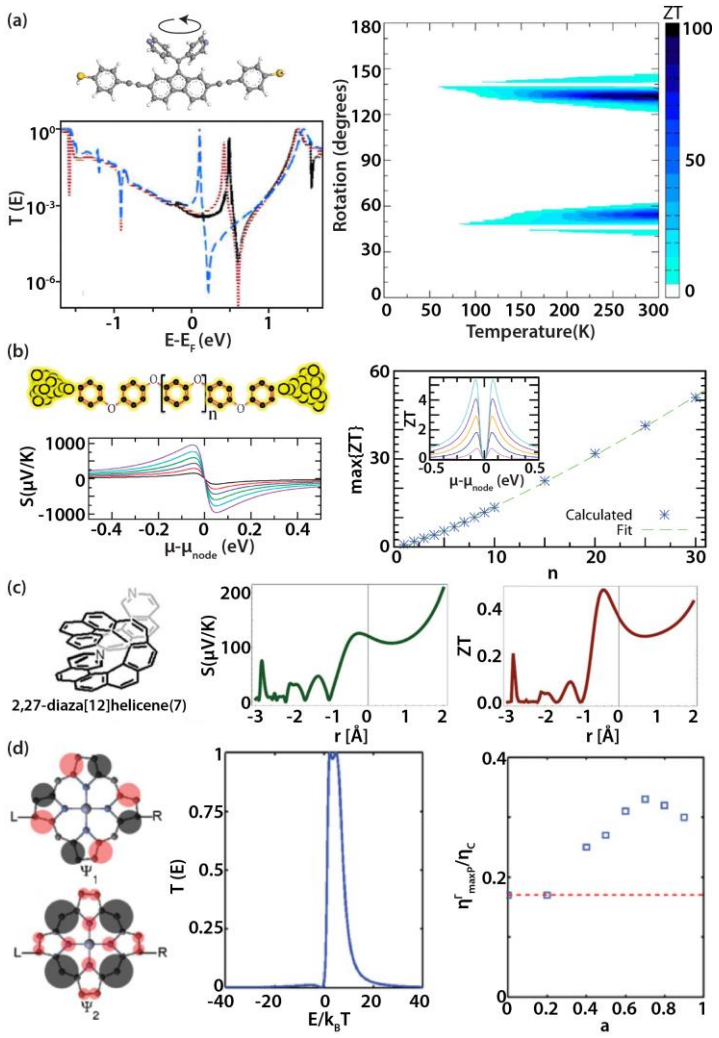

Figure 2.2: Theoretical proposals for enhancing thermoelectricity in molecular junctions.
(a) Results for CSW-479-bipyridine molecule.[18] Left top: schematic of the molecule with a side group which can rotate around the C-C bond connecting it to the molecule. Left bottom: transmission function when the side group is rotated. Right: calculated *ZT* with respect to rotation angle and temperature. Darker color indicates higher *ZT*. (b) Computed thermoelectric properties of polyphenyl ether (PPE) molecules.[19] Schematic of the molecule is shown on top left with length denoted as *n*. Left bottom: Seebeck coefficient vs chemical potential from $n = 1$ (black line) to $n = 7$ (purple line). Right: Maximum *ZT* plotted as a function of *n*. Inset: *ZT* vs. chemical potential, where the maximum *ZT* value increases with *n*. (c) Helicene MJs.[21] Left: Schematic of helicene molecule subject to mechanical stretching/compression. Middle: Seebeck coefficient with respect to stretching/compressing distance. $r < 0$ indicates compression and $r > 0$ stretching. Right: Plot of calculated *ZT*. (d) Analysis of high power output energy conversion.[45] Left: schematic of zinc porphine molecule with sketching of wave function of the two degenerate levels. Light/dark shade indicates positive/negative magnitude of wave function. Middle, plot of the transmission function. The low-energy tail is eliminated. Right: plot of efficiency at maximum output power (η^{Γ}_{maxP}) in units of Carnot efficiency (η_C) as a function of the difference between the coupling strength of two levels (a, defined in Eq. (10)).

To overcome this challenge, Karlstrom *et al.*[45] took advantage of the quantum interference in a two-level system (Fig. 2.2(d)) where the transmission function is expressed as

$$\tau(E) = \Gamma^2 \left| \frac{1}{(E - E_F) + E_1 + i\Gamma} - \frac{a^2}{(E - E_F) + E_2 + ia^2\Gamma} \right| \quad (10)$$

where the energy levels E_1 and E_2 are located on the same side of E_F, and the coupling strengths of the two energy levels to the electrodes differ by a factor of a^2. When $E^1 = a^2 E_1$, $\tau(E)$ is zero at E_F and is large for a finite range of energies above E_F . This implies that $\tau(E)$ has a large gradient at E_F and a finite width so that the system can operate with large power output. They further showed that the efficiency of such a system can be very close to the CA-limit. Finally, they suggested that the desired transmission function can be realized in Au-zinc porphine-Au AMJs.

Taken together, computational work on the thermoelectric efficiencies of AMJs suggests various strategies to achieve energy conversion at very high efficiencies (close to the Carnot limit) and large power outputs (close to the CA-limit). Key to achieving this goal is to develop strategies for achieving transmission functions that show rapid variations at the Fermi energy (e.g. delta/step shaped functions or an asymmetric Lorentzian-like transmission function[56]). Other approaches to tune the transmission function include redox control of the quantum interference within phase coherent molecular wires[57], variation of the transition metal-center in porphyrin-based conjugated molecules,[58] and creating π-π overlap between planar aromatic anchor groups and electro-burnt graphene electrodes[59]. In the following, we will discuss past experimental work on probing the thermoelectric properties of AMJs.

2.4.2 Experimental Progress

Several groups have experimentally quantified the thermoelectric properties of AMJs. Below, we first provide a brief discussion of experimental techniques that were developed to measure the thermoelectric properties of AMJs in two-terminal configurations, i.e., techniques that enable the measurement of a voltage output from junctions created by trapping molecules between a hot and a cold electrode. Subsequently, we review experimental work that elucidated the dependence of thermoelectric properties of AMJs on molecular length, end groups, molecular structures and conformation, electrode materials, and temperature. Finally we discuss three-terminal techniques that enable tuning the thermoelectric properties of AMJs.

2.4.2.1. Two-terminal thermoelectric measurements

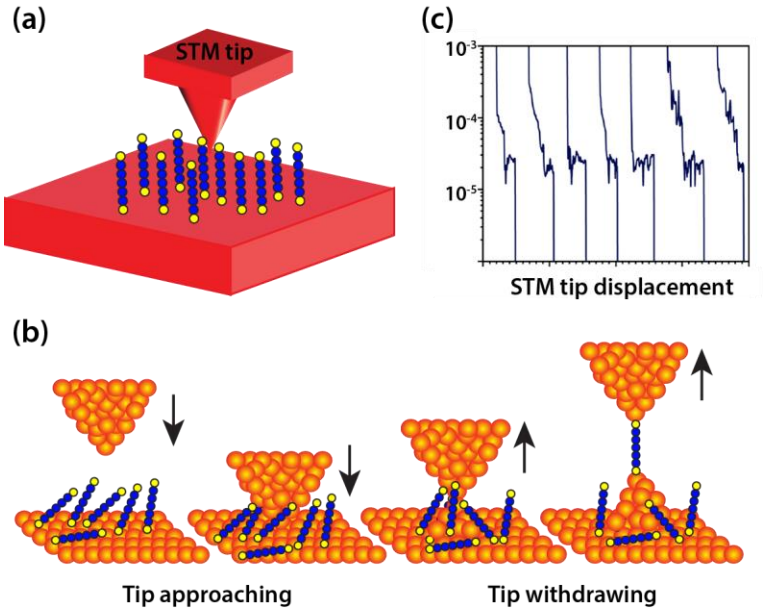

Figure 2.3: Schematic of the STM break junction (STMBJ) technique.
(a) STM tip is in proximity to a substrate bonded with SAM MJs. (b) The process of trapping a single MJ. STM tip is brought in contact with the substrate. MJs are formed when the STM tip retracts from the substrate until only one molecule bridges the tip and substrate. (c) Representative traces of electrical conductance of the junction during the withdrawal process.[60]

The initial experimental studies of thermoelectric properties of AMJs were performed by Reddy *et al.*[61]. In performing these studies the authors adapted a STM based technique called the STM break-junction (STMBJ) technique that was originally developed by Xu and Tao[62] for

probing electrical transport in AMJs (Fig. 2.3(a)). Since the electrical and thermoelectric properties of AMJs are pivotal to thermoelectric energy conversion, we first introduce the STMBJ technique and then describe how it was modified[61] for single-molecule thermoelectric measurements.

In the STMBJ technique a voltage bias is applied between a sharp tip of an STM (typically made of Au) and a Au substrate covered with a monolayer of molecules that are chemically bound to the substrate via endgroups such as thiols (-SH). The tip is displaced towards the substrate while the electrical conductance between the tip and the sample is being monitored. This process continues until an electrical contact is established and an electrical conductance of ~5 G_0 or greater is observed (signifying the formation of Au-Au atomic contacts). During this process, in addition to the formation of Au-Au contacts, some molecules stochastically bridge the electrodes (see Fig. 2.3(b)). Subsequently, the tip is withdrawn from the substrate, while monitoring the electrical conductance. This process results in a scenario where a few molecules bridge the tip and substrate. By further withdrawing the tip, the molecular bridges break successively until there is only one molecule bridging the tip and the substrate. During this withdrawal process the electrical conductance of the tip-molecule-substrate junctions is measured. Typical conductance traces obtained in such an experiment[60] are shown in Fig. 2.3(c). A substantial number of conductance traces can then be used to analyze and obtain statistically significant information about the electrical properties of AMJs.

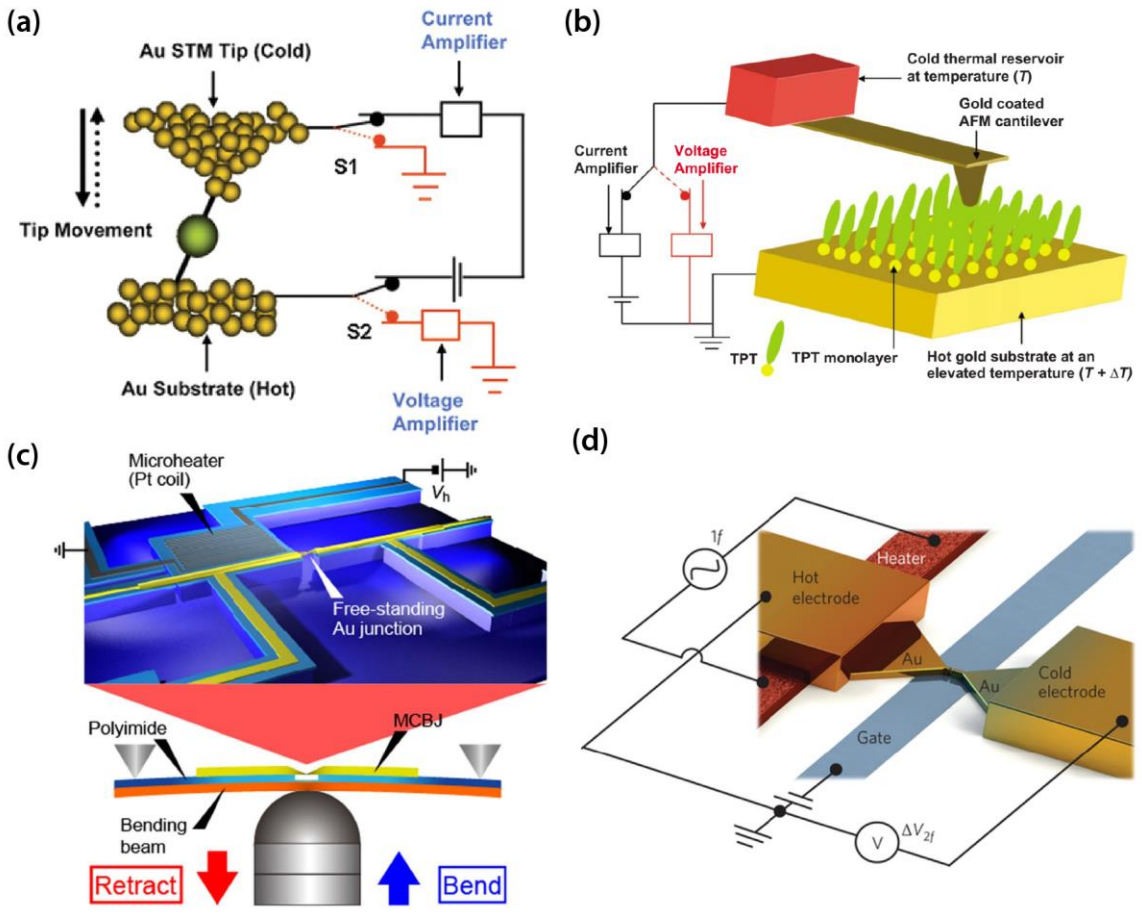

Figure 2.4: Schematics of experimental setups for thermoelectric measurements of AMJs.
(a) STMBJ based setup.[61] The STM tip is kept at ambient temperature while the substrate is heated up. Connections to the current and voltage amplifiers are made at different times to measure the thermoelectric voltage across the junctions. (b) CP-AFM based setup.[63] The AFM cantilever is in contact with a reservoir at temperature T while the Au substrate is heated to an elevated temperature $T + \Delta T$. (c) MCBJ setup.[64] A free-standing Au junction is created by bending the substrate. Temperature differentials between the electrodes are established via an integrated Pt coil micro-heater. A polyimide layer insulates the Au electrodes from the bending substrate. (d) EBJ setup.[65] A gate electrode is used to tune the electronic structure of the junction. One of the electrodes is heated by applying a sinusoidal electric current at frequency f through an integrated heater, resulting in a temperature difference and a thermoelectric voltage output at frequency $2f$.

In order to thermoelectric effects of AMJs, the STMBJ technique is modified so as to enable the application of a temperature difference across the AMJ. In Fig. 2.4(a), a single AMJ formed by using the STMBJ technique is depicted. The Au substrate is heated while the STM tip is kept at room temperature by placing it in contact with a large thermal reservoir. Because thermal conductance of the AMJ is much smaller (quantified later in this article) than the thermal

conductance of the gold STM tip, a tip-substrate temperature difference, ΔT, is readily established.[55, 57]

The procedure to measure the Seebeck coefficient involves trapping of multiple molecules between the electrodes by following the procedure described above. Subsequently, the voltage bias and the current amplifier that are used to monitor the current are disconnected and a voltage amplifier is connected to measure the thermoelectric voltage induced by ΔT (see Fig. 2.4(a)). The tip is slowly withdrawn until all the trapped molecules break off. During this process, the output voltage, ΔV, is continuously monitored. When the last molecule breaks off, the thermoelelctric voltage vanishes. This output voltage ΔV, due to ΔT, is a measure of the Seebeck coefficient and is obtained by $S = -\Delta V / \Delta T$.

Reddy *et al.*[61] employed the above-described STMBJ technique to probe the thermoelectric properties of AMJs created from benzenedithiol, dibenzenedithiol and tribenzenedithiol molecules and Au electrodes (Fig. 2.5(a)). These experiments revealed that the Seebeck coefficient of these aromatic AMJs is positive and increases monotonically (and approximately linearly) with molecular length.

The STMBJ technique as applied to thermoelectric studies was further improved by Widawsky *et al.*[66] who succeeded in simultaneously recording the electrical conductance and thermopower of single AMJs in STMBJ technique by measuring both the zero-bias thermocurrent and the electrical conductance under a small applied bias. Using this method the authors explored several amine-Au linked and pyridine-Au linked AMJs. From these measurements they observed a positive Seebeck coefficient for amine-Au linked AMJs and a negative Seebeck coefficient for pyridine-Au linked AMJs, confirming that transport in amine-Au junctions is HOMO dominated whereas that in pyridine-Au junctions is LUMO dominated.

In addition to the STMBJ technique, a different technique that is based on an atomic force microscope (AFM) was developed by Tan *et al.*[63] to probe thermoelectric effects in SAM based AMJs. Briefly, a Au-coated AFM probe made of Si, that is at ambient temperature, is placed in contact with a heated Au substrate that is covered with a monolayer of molecules, while the deflection of the cantilever is continuously monitored and maintained at a constant value using feedback control (Fig. 2.4(b)). The electrical conductance and the Seebeck coefficient of the tip-SAM-metal junctions are directly measured by monitoring the current output under a small bias and by measuring the voltage output under a temperature difference.

Mechanically controlled break junction (MCBJ) technique is another widely used experimental approach for probing the electrical and thermoelectric transport properties of AMJs. The first mechanical "break junction" experiment was conducted by Moreland and Ekin[67] for electron tunneling in superconductors. Later Muller and van Ruitenbeek[68] developed a MCBJ technique in which a suspended metallic wire with a notch at the center is attached to a thin substrate (Fig. 2.4(c)). Further, the flexible device is mounted in a three-point contact configuration. The center of the device is pushed by a piezoactuator whose motion can be controlled precisely by external bias. This process results in an elongation of the wire and eventually leads to the fracture of the wire at the notch, exposing clean metal surfaces. By controlling the motion of the actuator, the gap size between the electrodes can be systematically controlled allowing one to close and reopen the gap. Specifically, the displacement between the electrodes is a small fraction (also called reduction factor) of the displacement of the actuator due to the geometry of the MCBJ platform. This reduction factor enables very precise control of the separation of the electrodes with picometer stability. Given the excellent stability of the

MCBJ technique it has been employed extensively in studies of transport properties of AMJs and atomic junctions.[64, 69, 70, 71, 72, 73, 74, 75, 76]

Reed *et al.*[76] applied the MCBJ technique to perform charge transport measurements in organic molecule based AMJs. Briefly, they exposed the Au electrodes in an MCBJ setup to benzenedithiol (BDT) molecules. This enabled them to successfully trap BDT molecules between the Au electrodes. Given the stability of the MCBJ platform they were able to trap AMJs and perform electrical transport experiments in them.

Tsutsui *et al.*[64] adapted the MCBJ technique for probing thermoelectric properties of AMJs by integrating a Pt serpentine heater into one of the electrodes, which enabled them to apply temperature differentials across AMJs (Fig. 2.4(c)). Using this approach, the authors probed both the electrical conductance and the Seebeck coefficient of Au-BDT-Au junctions and reported that the transport properties were sensitive to the geometric configuration of BDT molecules. They showed that upon mechanical stretching, in some cases, the molecule tilts into an upright direction and the Au-S bonds are elongated, resulting in a weaker coupling to the contact and a gradual shift of the HOMO level, accompanied by a decrease in conductance and a change (slight increase or decrease) in the Seebeck coefficient. In other cases they found that the configuration of the contact was dramatically changed, so that E_F shifted towards HOMO level, leading to an increased conductance and Seebeck coefficient.

2.4.2.2. Length dependence of thermopower in molecular junctions

Researchers have explored the dependence of the thermoelectric properties of AMJs on molecular length. For Au-alkanedithiol (ADT)-Au junctions, the thermopower was found (Fig. 2.5(a)) to vary linearly with increasing N (N is the number of carbon atoms in the backbone) while the electrical conductance decreased exponentially.[77] Similarly, for aromatic AMJs, e.g.

Au-phenylenediamine-Au[77] and Au-phenylenedithiol-Au[61, 77, 78] junctions, thermopower was found to increase linearly with length (Fig. 2.5(a)). Similar results are found by Widawsky *et al.*[79] for trimethylstannylmethyl-terminated polyphenyls with 1−4 phenyl rings (P1−P4) (Fig. 2.5(b)). However, they also found that the thermopower of trimethylstannyl-terminated alkanes with N = 6, 8 and 10 (C6, C8, and C10) has little length dependence (Fig. 2.5(b)).

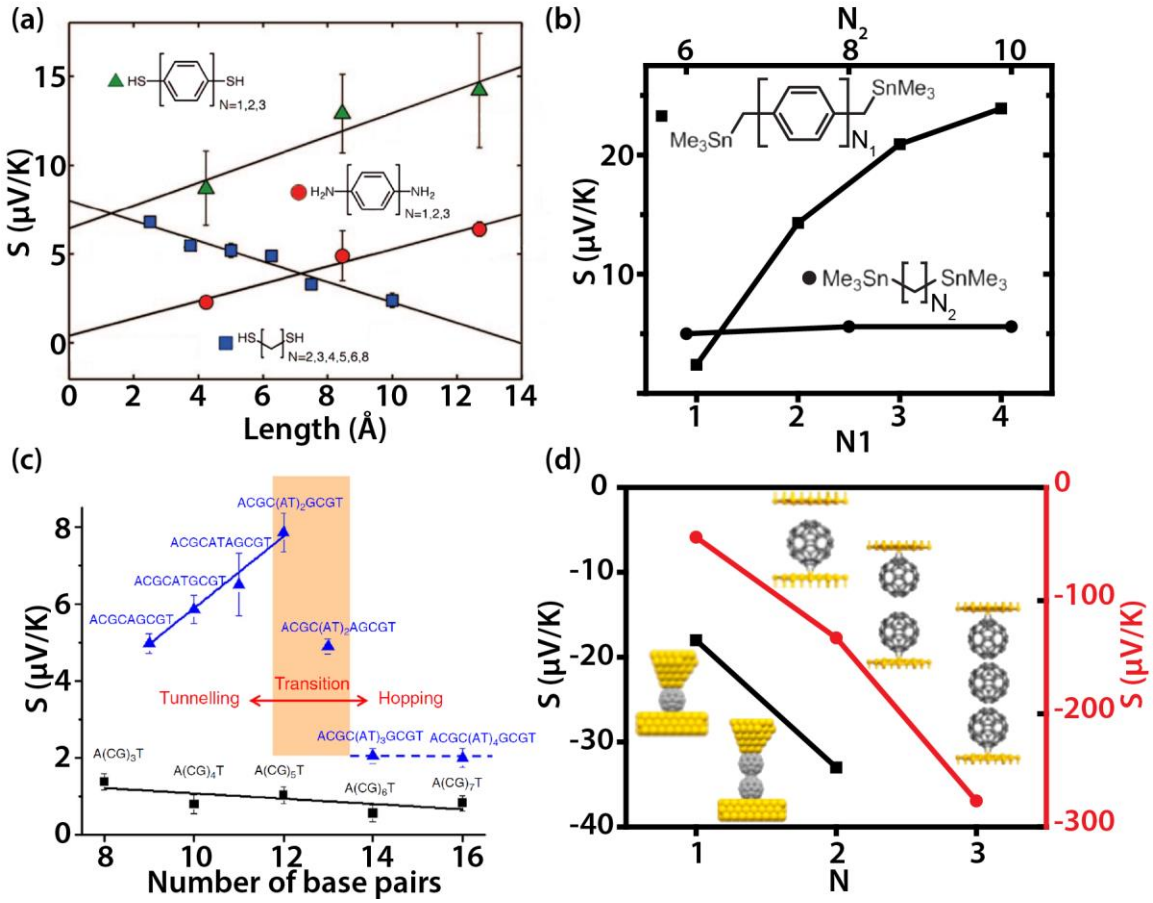

Figure 2.5: Length dependence of the Seebeck coefficient of AMJs.
(a) Seebeck coefficient of phenylenedithiol (green triangle), phenylenediamine (red circle) and ADT (blue square) molecular junctions with respect to molecular length.[77] (b) Thermopower of $SnMe_3$ terminated polyphenyl (square, N_1) and $SnMe_3$ terminated alkane (circle, N_2) vs molecule length.[79] (c) Transition from the tunneling regime to the hopping regime of (CG) DNA molecules inserted with (AT) tunneling blocks (blue triangle). (CG) sequence DNA molecules don't show transition behavior (black squares).[80] (d) Experimental (square, left axis) and computational (circle, right axis) results of C_{60} monomer, dimer and trimer (only computational data shown for trimers).[81]

Length dependence of thermopower was also studied in junctions made from DNA molecules of different sequences (Fig. 2.5(c)).[82, 80] For GC sequence double-stranded DNA molecules, Li *et al.*[79] reported a linear increase in resistance with molecular length whereas the Seebeck coefficient was small and weakly dependent on the length. This is due to hopping of holes along the molecules dominates the charge transport in GC sequences where G act as hopping sites. When AT pairs, which are expected to act as a tunneling barrier, were inserted in the middle of GC sequence, both the conductance and thermopower changed. It was found that when the number of inserted AT block base pairs *m* is smaller than 4, the resistance increased exponentially with the length of the block, and the Seebeck coefficient increased linearly and is large compared with the size of the GC molecule. When $m \geq 4$, the transport mechanism was reported to transition from tunneling to hopping, in which regime the resistance shows weak dependence on length, and the Seebeck coefficient drops to small values.

In addition to the above described measurements of length dependence Evangeli *et al.*[81] created a C_{60} dimer by contacting a tip that had one C_{60} molecule adhered to it with another C_{60} molecule which adhered to a Au substrate (Fig. 2.5(d)). They found that the thermopower of the C_{60} dimer is approximately doubled in comparison to single C_{60} junctions, resulting in a relatively high Seebeck coefficient of -33 μV/K. Computational results suggested that the thermopower and *ZT* increased with the number of C_{60} monomers in the molecular chain due to the intermolecular interaction, suggesting that it may be possible to improve thermoelectric properties by manipulating C_{60} junctions.

2.4.2.3. Effect of end groups on thermoelectric properties

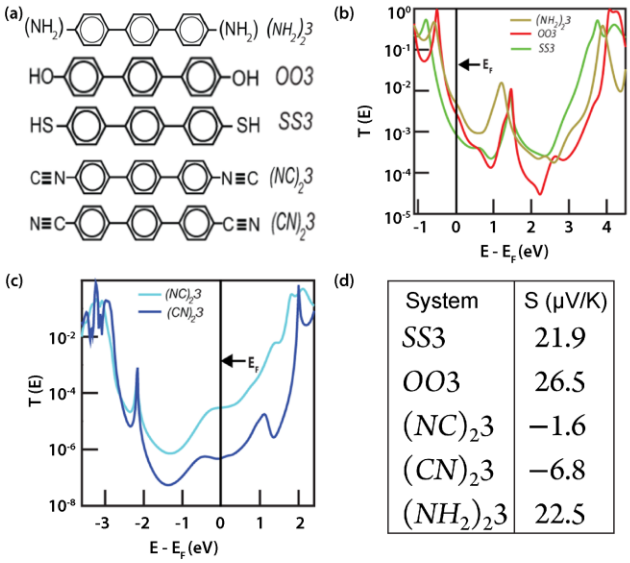

System	S (μV/K)
$SS3$	21.9
$OO3$	26.5
$(NC)_2 3$	−1.6
$(CN)_2 3$	−6.8
$(NH_2)_2 3$	22.5

Figure 2.6: Theoretical results for triphenyl AMJs with five different end groups.
(a) Schematic of triphenyl molecules with five different end groups[83]. (b) and (c) Transmission as a function of energy. For SS3, OO3, and $(NH_2)_2 3$ molecules, the HOMO peak is closer to the E_F. For $(NC)_2 3$ and $(CN)_2 3$ the LUMO peak is closer to the E_F, resulting in a LUMO-dominated transport. (d) Calculated Seebeck coefficient for five types for triphenyl molecular junctions.

The end groups bridging molecules to electrodes play an important role in charge transport and thermoelectric properties of AMJs.[83, 84, 85, 86] Experimental measurements of thiol-terminated aromatic AMJs showed a positive thermopower[34, 74, 75] while measurements of isocyanide-terminated junctions showed a negative thermopower[87]. In addition, experimental work on trimethyltin-terminated aromatic molecules[79] demonstrated slightly higher thermopower compared to thiol groups[87]. Balachandran *et al.*[83] provided a theoretical explanation for end-group effects on thermopower of AMJs. Specifically, they investigated five different end groups (isocyanide, nitrile, amine, thiol and hydroxyl) which couple triphenyl molecule to Au electrodes (Fig. 2.6) and studied the influence of end groups. They found that isocyanide, nitrile and amine end-groups led to charge transfer out of the molecule upon coupling with the electrodes, resulting in a downward shift of the energy levels, which positioned the HOMO peak closer to the Fermi energy. In contrast, thiol and hydroxyl end-groups resulted in charge transfer from the

electrodes into the molecule, which led to a slight downward shift in the energy levels thus placing the LUMO peak closer to the Fermi energy.

2.4.2.4. Effect of chemical structure, conformation and shape of molecules

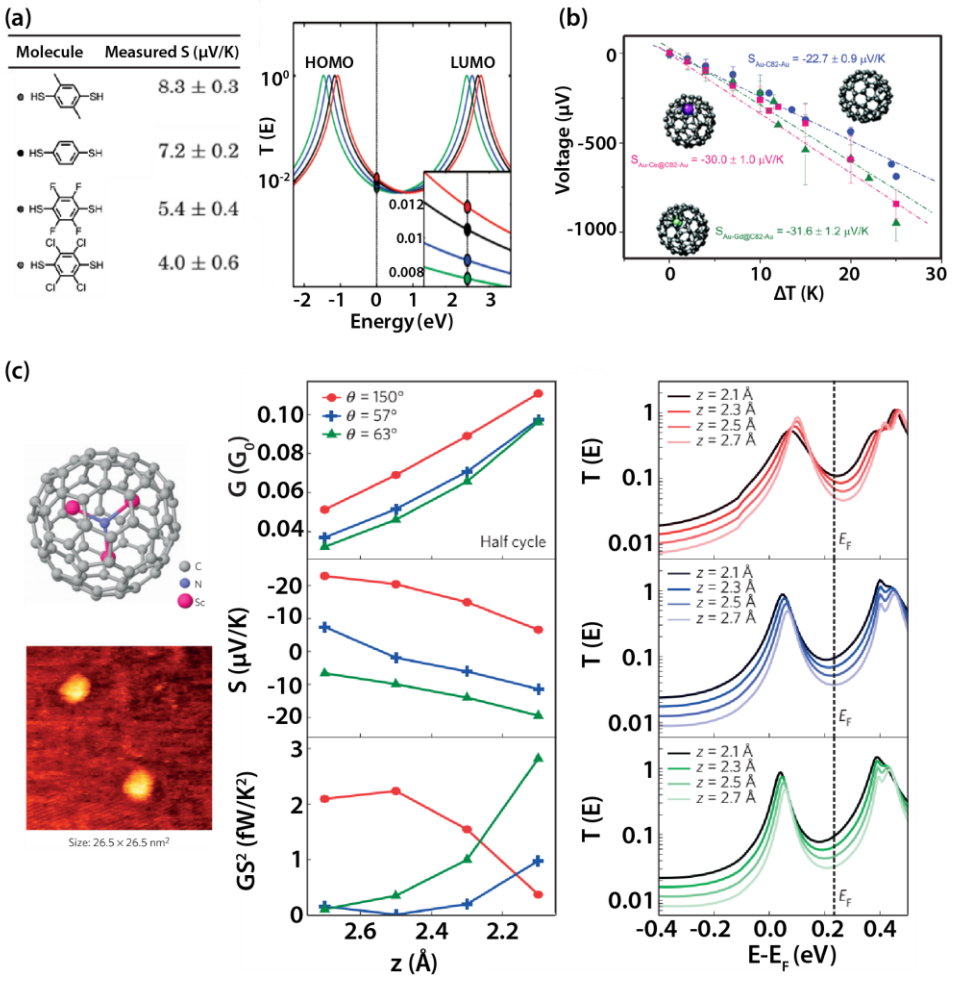

Figure 2.7: Effect of chemical structure, conformation and shape of molecules on thermoelectric properties of AMJs.
(a) Thermoelectric properties of BDT based MJs with substituents.[88] Left: Structure of BDT2Me, BDT, BDT4F, and BDT4Cl molecules (from top to bottom). Right: Lorentzian shaped transmission functions which illustrates how the transmission function is expected to changes due to electron-withdrawing groups (BDT4F, blue line and BDT4Cl, green line, BDT, black line), and electron-donating groups (BDT2Me, red line). (b) Seebeck coefficient of C_{82} derivative based junctions: C_{82} (blue circle), Gd@C_{82} (green triangle), Gd@C_{82} (red square).[89] (c) Effect of mechanical deformations of molecular junctions on their thermoelectric properties.[90] Left: Schematic of $Sc_3N@C_{80}$ molecule and two isolated $Sc_3N@C_{80}$ molecules under STM. Middle: Conductance, Seebeck coefficient and power factor (GS^2) as functions of pressing distance. Red circle, blue square and green triangle represents different molecule orientation corresponding to the substrate. Right: Theoretical transmission functions vs. energy. Red, green and blue colors represent different molecular orientations. Lighter colored line represents larger pressing distances.[90]

The effect of chemical structure on thermoelectricity of AMJs has been probed by adding electron-withdrawing/donating groups (fluorine, chlorine, and methyl) to BDT molecules (Fig. 2.7(a)).[88] It was suggested that the presence of electron-withdrawing groups (fluorine and chlorine) on a BDT molecule shifts the energy levels of AMJs downwards, leading to a decreased thermopower, while the presence of electron-donating group (methyl) groups shift the energy levels upwards, leading to an increased thermopower. Since BDT has HOMO dominated charge transport properties, shifting the energy levels up (down) gives rise to a larger (smaller) slope in the transmission function at the Fermi level.

The effect of molecular conformation on the electrical conductance has also been studies by several groups.[91, 92, 93] For example, it was shown that in aromatic molecules, when the planes associated with each of phenyl rings are twisted from being "flat" ($\theta = 0°$, θ indicates the twist angle between two benzene plates) to being "perpendicular" ($\theta = 90°$), the conductance decreases by a factor of 30.[91] The thermoelectric properties of AMJs created from fullerene based molecules was investigated by Lee *et al.*[89]. They experimentally investigated three fullerene derivatives (C_{82}, Gd@C_{82} and Ce@C_{82}) and found enhanced thermopower of Gd@C_{82} and Ce@C_{82} (Fig. 2.7(b)). Computational analysis of the same system suggested that this enhancement was due to the encapsulated metal atoms that induced changes in the geometric and electronic structure of the fullerene molecule.

Researchers have also explored the effect of mechanical deformations of AMJs on their thermoelectric properties.[64, 90] For example, by studying Au-Sc_3N@C_{80}-Au junctions, where an Sc_3N molecule is imbedded into a C_{80} cage (Fig. 2.7(c)), Rincon-Garcia *et al.*[90] found that the magnitude and the sign of thermopower both depend on the orientation of the molecule and force applied to the molecule. Further, computational analysis by the authors also suggested that the

introduced Sc_3N creates a sharp resonance near the Fermi energy, and the location of the peak in transmission function depends strongly on the molecular orientation and applied pressure, so the thermopower can exhibits both a positive and a negative sign, depending on the relative position of the transmission peak with respect to the Fermi level. They emphasized that the transport resonance plays an import role in thermoelectric performance and that $Sc_3N@C_{80}$ can act as a bi-thermoelectric material.

2.4.2.5. Effect of electrode materials

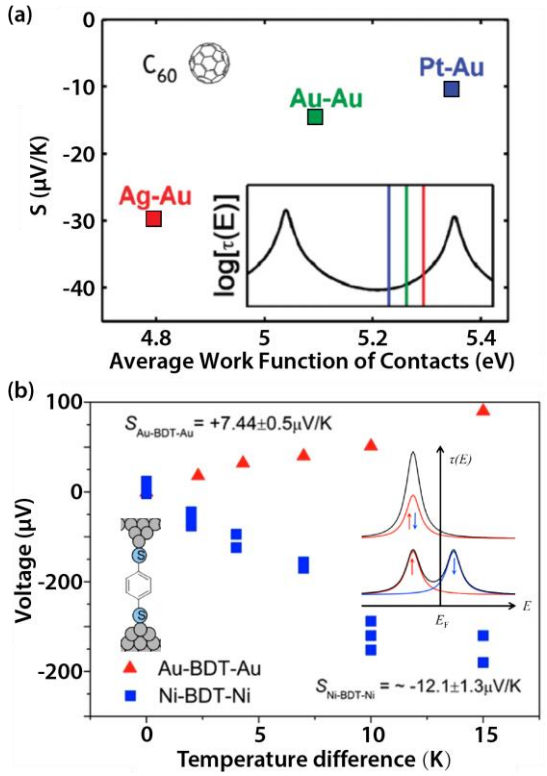

Figure 2.8: Effect of electrode materials on thermoelectric properties of AMJs.
(a) Thermopower of Au-C_{60}-Au/Pt/Ag junctions vs. the average work function of electrodes. Inset: Lorentzian approximation of the transmission function, where blue, green, and red vertical lines approximate the position of E_F for Au-Pt, Au-Au, and Au-Ag junctions.[94] (b) Plot of measured thermoelectric voltage of Au-BDT-Au (red triangle) and Ni-BDT-Ni (blue square) molecular junctions. Top inset: transmission function of Au-BDT-Au junction. Bottom inset: transmission function of Ni-BDT-Ni junction. Ni-BDT-Ni junction has a negative Seebeck coefficient (as opposed to the positive Seebeck coefficient of Au-BDT-Au junctions) due to spin-split hybridized states generated when BDT LUMO orbital coupled with Ni electrodes.[95]

Although gold is the prototypical electrode material in most AMJ experiments, other metals have also been studied to identify potentially interesting thermoelectric properties.[17, 40, 96, 97] The advantage of other electrode materials lies in the possibility of bringing the Fermi energy of electrodes closer to the orbital that dominates the charge transport properties of molecules.[98, 99] Past work on fullerene based molecules (C_{60}, PCBM ([6,6]-Phenyl-C_{61}-butyric acid methyl ester) and C_{70}) (Fig. 2.8(a), showing C_{60} only) showed that the Seebeck coefficient is suppressed when one of the Au electrodes is replaced by Pt. In contrast, it was found that the Seebeck coefficient is doubled when one of the Au electrodes was replaced with Ag.[94] Enhancements in the Seebeck coefficient were also reported in experiments involving Ni electrodes. Computations revealed that these enhancements arise from the spin-split hybridized states that are generated when the HOMO orbital of the BDT molecule couples with Ni electrodes (Fig. 2.8(b)).[95] In addition to these studies, computational work has pointed out that semiconducting electrodes[46] and carbon nanotubes[30] could suppress the "electron-like" contributions to the thermopower and cutoff the lower energy tails of HOMO transmission.[46] In these cases the output power of the systems was found to be greatly boosted.

2.4.2.6. Temperature dependence of thermopower in molecular junctions

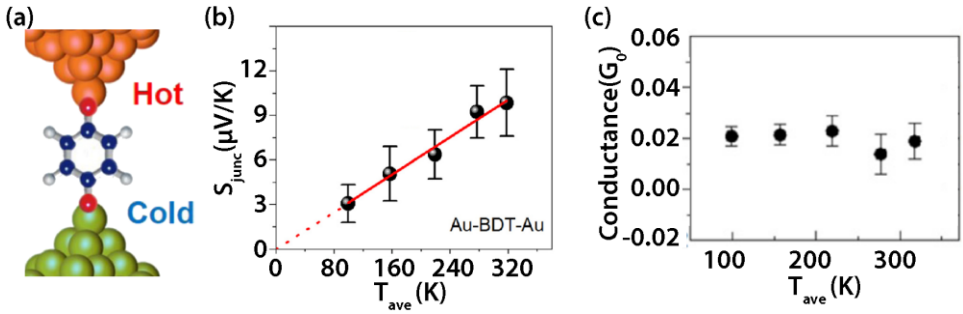

Figure 2.9: Temperature dependence of thermopower of molecular junctions.
(a) Schematic of a Au-BDT-Au junction. (b) Plot of measured Seebeck coefficient as function of temperature. Linear fit indicates that the Seebeck coefficient vanishes when the temperature tends to 0 K. (c) Plot of the electrical conductance as function of temperature. The electrical conductance remains invariant with temperature.[100]

According to Landauer formula, thermopower is expected to be linearly dependent on the average temperature of the molecular junction (see Eq. (2)). Kim *et al.*[100] varied the average temperature of Au-BDT-Au AMJs and experimentally verified this prediction (Fig. 2.9). Since the figure of merit ZT is proportional to the power factor (G_eS^2) and temperature T, and inversely proportional to the thermal conductance G_{th}, this work indicates that ZT can potentially increases as T^3 if the thermal conductance is independent of temperature, as is expected when the operating temperature is higher the Debye temperature of the electrodes.

2.4.2.7. Three-terminal thermoelectric measurements

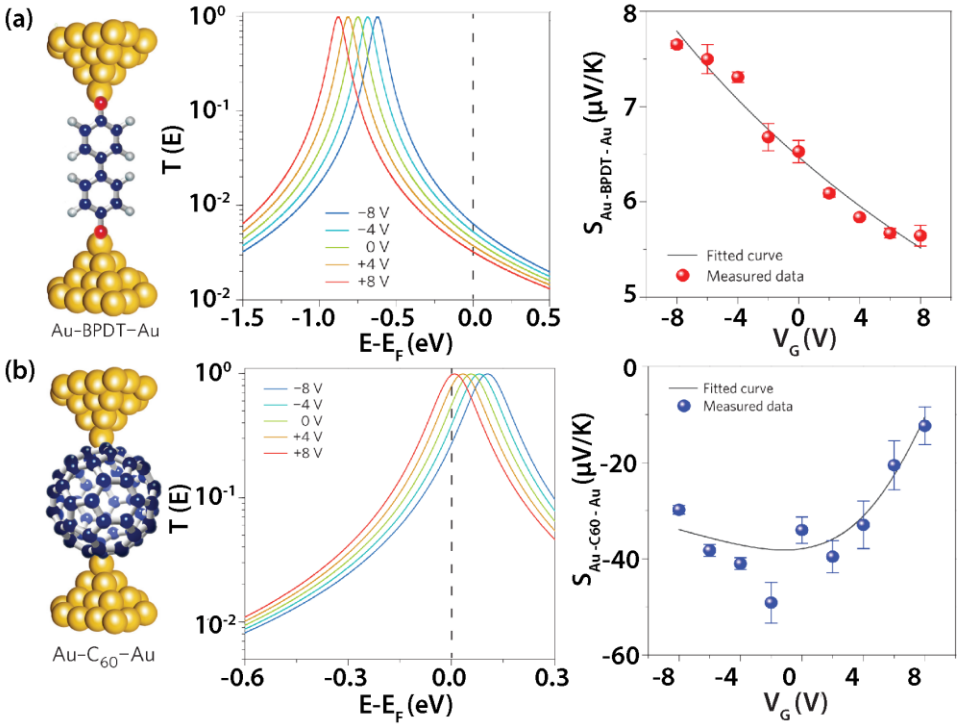

Figure 2.10: Electrostatic tuning of thermoelectric properties of AMJs, Au-DBDT-Au (a) and Au-C_{60}-Au (b) junctions using three-terminal EBJ technique.
Left: molecular junction structures. Middle: Lorentzian curves that approximate the transmission function when the gate voltage is varied from -8 V to +8 V. Right: Measured Seebeck coefficient as a function of gate voltage.[65]

Key to improving the thermopower of an AMJ is to shift the transmission function such that the slope and magnitude of the transmission function at the Fermi energy are maximized.

However, most measurements of thermoelectric properties of AMJs have relied on two-terminal measurements, which do not offer control on the electronic structure of the junction. Past research[101, 102, 103, 104, 105, 106, 107, 108, 109, 110, 111] has shown that it is possible to create three-terminal devices that can tune the electronic structure of junctions via a gate electrode. These devices are often created by a process called electromigration which creates three-terminal AMJs by inserting molecules in nanometer-sized gaps formed during electromigration.[105, 112] In creating these devices, a gold nanowire is first fabricated using electron-beam lithography on a doped Si layer which is coated with a thin dielectric layer. Subsequently, a large electric current is applied to the nanowire, causing the movement of metal atoms, which creates a nanometer or sub-nanometer sized gap in the nanowire. Molecules are deposited into the nanoscale gap by exposing the electrodes to molecules in a solution. The broken portions of the Au nanowire create two terminals (source and drain electrodes), while the Si back gate serves as a gate electrode. While several groups have used three terminal devices for tuning electrical transport, such devices could not be readily used for thermoelectric measurements due to the challenges in establishing temperature differences across the nano-gap between electrodes.

In order to overcome the limitations of two-terminal thermoelectric measurements, Kim *et al.*[65] created novel three-terminal devices based on EBJ and integrated an electric heater into one electrode (source or drain) that allowed them to apply temperature differences across AMJs while electrostatically gating their electronic structure. Using such devices (Fig. 2.4(d)), they probed the thermoelectric properties of Au-biphenyldithiol (BPDT)-Au and Au-C_{60}-Au junctions. These measurements revealed that the thermoelectric properties can be significantly improved when the dominant transport orbital is located closely to Fermi energy. In analyzing these experimental results the transmission function of the junctions was approximated by a

Lorentzian function. For both Au-BPDT-Au junction (Fig. 2.10(a)), and Au-C_{60}-Au junctions (Fig. 2.10(b)), the thermoelectric properties were found to be tunable when a gate voltage was applied. This work demonstrated the feasibility of improving thermoelectric properties by tuning the electronic structure of AMJs.

2.4 Heat Transport in Molecular Junctions

In this section we provide a review of the studies of thermal transport in AMJs and polymer chains. We begin by first describing the computational and theoretical work on thermal transport in AMJs. Subsequently, we will describe the status of current experimental work and compare the results from experiments with those from computational predictions.

2.4.1 Theoretical Results

Thermal transport in macroscopic systems is well described by Fourier's law, $J = -\kappa \nabla T$, where J is the heat current density, κ is the thermal conductivity and T is the absolute temperature. However, numerous computational studies have suggested that Fourier's law is inapplicable to modeling thermal transport in single molecule chains and junctions. Historically, this important characteristic was identified in the pioneering work of Fermi, Pasta and Ulam (the FPU problem)[113] where they studied the dynamics of a 1D lattice chain of N monoatomic particles. They found that a small nonlinearity in the harmonic 1D chain can give rise to a surprising divergence in thermal conductivity. Specifically, they found that for a chain of N atoms, the thermal conductivity varies as $\kappa \propto N^{\alpha}, \alpha > 0$.

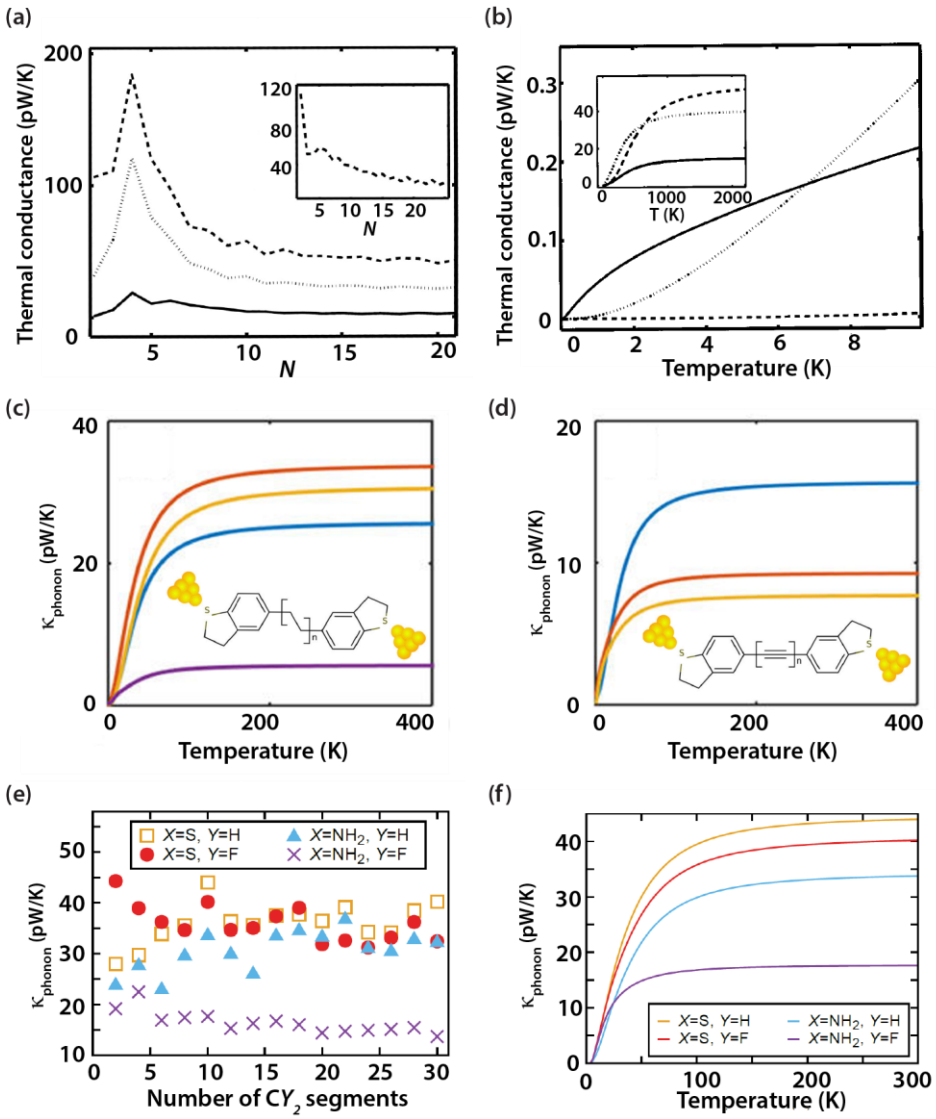

Figure 2.11: Calculated thermal conductance of single molecule junctions.
(a) Thermal conductance of alkane molecules vs. the chain length at different temperatures (solid line 50 K, dotted line 300 K, dashed line 1000 K) for the case of weak molecule-reservoir coupling.[114] Inset: calculations for the case of strong molecule-reservior coupling at 1000 K. (b) Temperature dependent thermal conductance of alkane molecules for different chain lengths (number of carbon-atom in the backbone *N*) (dashed line *N* = 2, dotted line *N* = 5, full line *N* = 14).[114] (c) Temperature dependent phononic thermal conductance of alkanes (chemical structure shown as inset, blue line n = 1, red line n = 2, yellow line n = 4, purple line n = 8).[115] (d) Temperature dependent phononic thermal conductance of oligoynes (blue line n = 1, red line n = 2, yellow line n = 4).[115] (e) Room temperature (300 K) phononic thermal conductance vs. number of CY_2 units (Y= H, F) in the molecule for different end anchoring groups X (X = S, NH_2).[116] (f) Temperature dependent phononic thermal conductance for molecules with 10 CY_2 units.[116]

More recently, several other groups have explored thermal transport in 1D-chains based on the FPU chain model.[117, 118] Specifically, simulations performed using non-equilibrium molecular dynamics and equilibrium Green-Kubo methods confirmed that a divergence in

thermal conductivity is to be expected for various configurations of the interatomic potential as well as for chains with a diatomic basis. Several of these studies reported that the value of the exponent (α) is ~0.4, suggesting that such divergences are a general feature of 1D chains.

Despite the early theoretical findings leading to important insights into thermal transport in 1D atomic chains, the originally considered systems were relatively simple and did not include the effects of electrodes and the coupling between the chains and the electrodes. In order to capture these additional effects more realistic 1D structures such as AMJs and atomic junctions have also been recently explored. For example, Segal *et al.*[114] studied thermal conduction through alkane chains bridging two thermal reservoirs. They derived a Landauer-like expression for heat flux from a generalized Langevin equation. By considering the phonon modes of a given molecule and the thermal reservoir, they calculated the thermal conductance and revealed interesting dependencies of the thermal conductance on the length and temperature of the junction (Fig. 2.11(a), 2.11(b)). Specifically, they found that in the presence of weak reservoir-molecule coupling, the molecule chain achieved a maximum thermal conductance when the number (N) of the back-bone carbon atoms equals 4. Further, they found that a size-independent conductance is established when $N > 10$, indicating a strong divergence in the thermal conductivity. However, they found that when the reservoir-molecule coupling was strengthened, a Fourier-like thermal conductivity was recovered.

Ab initio methods were also employed by Sadeghi *et al.*[115] to study the thermal conductance of alkanes (N = 2, 4, 8, and 16) and oligoynes (N = 2, 4, 8). They identified the contributions to the thermal conductance from electrons and phonons and found that the phononic contribution for alkanes is ~700 times larger than the electronic contribution. Similar calculations for oligoynes suggested that the phononic contribution is only 30 times larger than

the electronic contribution. Further, similar to the findings of Segal *et al.*[114], the thermal conductance of both alkanes and oligoynes in this work was found to first increase and then decrease with the molecule length (Fig. 2.11(c), 2.11(d)).

More recently, Klöckner *et al.*[116] combined DFT and NEGF approaches to calculate the thermal conductance of alkanes (N = 2 to 30) and PTFE molecule (where H atoms in alkanes are replaced by F atoms) with different end anchoring groups (thiol and amine) (Fig. 2.11(e), 2.11(f)). They reported that the phononic thermal conductances in all scenarios are relatively insensitive to the molecular length. Further, they explored the effect of the anchoring group by calculating the thermal conductance for both thiol- (-SH) and amine- (-NH_2) terminated AMJs. They found that the thiol-terminated AMJs had a higher conductance than the amine-terminated ones.

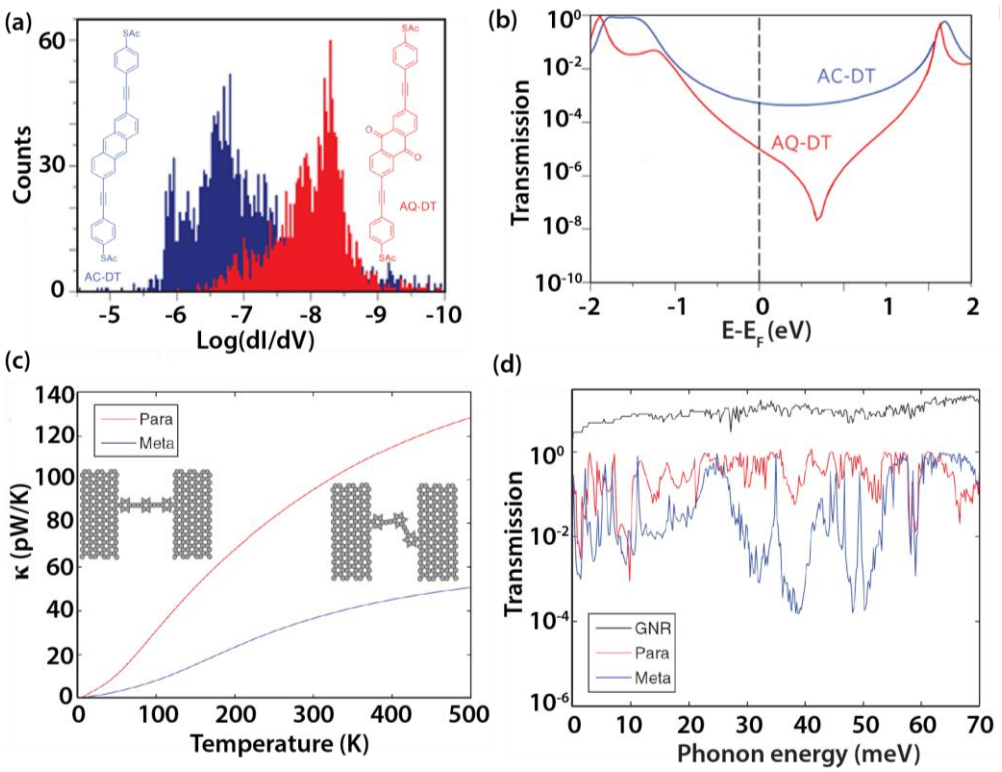

Figure 2.12: Influence of quantum interference on electrical and thermal (phonon) transport.
(a) Measured electrical conductance histogram of AC-DT and AQ-DT molecules (chemical structures shown as inset).[119] (b) Calculated transmission functions for AC-DT and AQ-DT.[119] Cross-conjugated AQ-DT molecule exhibits destructive electron interference effect. (c) Calculated phononic thermal conductance for para- and meta-connected molecules (chemical structures shown as insets).[120] (d) Calculated phonon transmission functions showing phononic quantum interference effect.[120]

Markussen[120] performed first-principle simulations of phonon transport through both linear-conjugated and cross-conjugated molecules. He showed that in cross-conjugated molecules, such as meta-connected benzene, the phonon transmission function exhibits destructive quantum interference. This observation is analogous to the destructive quantum interference effects for electron transport in similar molecules (Fig. 2.12(a), 2.12(b)).[119] Further, he found that the cross-conjugated AMJs reduce the thermal conductance by a factor of 2-5 compared to the linear-conjugated counterparts (Fig. 2.12(c), 2.12(d)).

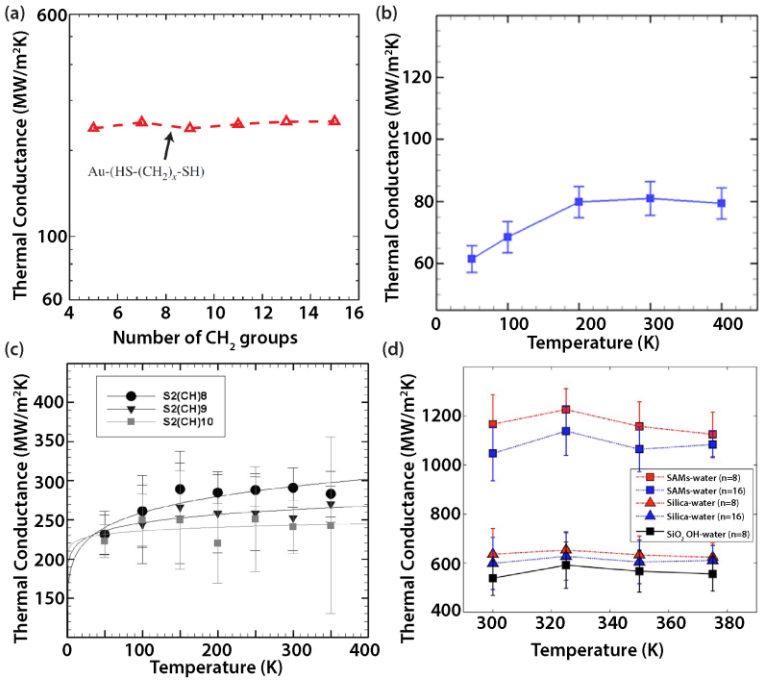

Figure 2.13: Calculated thermal conductance of self-assembled monolayer (SAM) AMJs.
(a) Thermal conductance across Au-ADT monolayer interface vs. the number of CH_2 groups in the backbone.[121] (b) Temperature dependent thermal conductance of GaAs-ADT (N = 8)-GaAs AMJs.[122] (c) Temperature dependence of the thermal conductance of Au-ADT (N = 8, 9, 10)-Au junctions.[123] (d) Temperature dependence of the thermal conductance of SiO_2-SAM-water junctions.[124] The SAM AMJs are formed by Alkysilanol ($-Si(OH)_2-(CH_2)_n$-OH, n = 8, 16).

In addition to studies in single AMJs, heat conduction through self-assembled monolayer (SAM) of molecules covalently bonded to the substrates has also been extensively investigated. Select computational results for different combinations of solid-SAM-solid/liquid junctions are summarized in Fig. 2.13. Specifically, Luo and Lloyd[122, 123] performed non-equilibrium and equilibrium molecular dynamics (NEMD) calculations in Au-SAM-Au junctions. The thermal conductance of such junctions was found to be independent of length and the applied external pressure. These results were also confirmed by Duda *et al.*[121] who calculated the interface thermal conductance across the Au-SAM junctions. They found that the thermal conductance is nearly constant upon varying the molecular length. Further, Goicochea et al.[124] studied thermal transport across silica-SAM-water junctions. They found that compared to the silica-water junctions the thermal conductance is enhanced by 1.8 – 3.2 fold when the silica surface is chemically functionalized by alkysilanol ($-Si(OH)_2-(CH_2)_n-OH$) to become hydrophilic. In addition, Hu *et al.*[125] studied thermal transport in Au-SAM-Si junctions using molecular dynamics simulations and found that the phonon transmission function shows distinct oscillatory behavior with strong frequency dependence, which indicates phonon interference effects. Further, they showed that this interference effect diminishes with increasing SAM thickness.

The observation of unusual phonon transport phenomena in AMJs have led to several proposals for control and manipulation of thermal properties.[126] As shown in Fig. 2.14, it has been proposed theoretically that AMJs can be used to create thermal rectifiers[127, 128, 129] (heat flow enhanced in one direction but suppressed in the other direction due to the asymmetrical molecule-reservoir coupling), field-effect phononic thermal transistors[130] (by reversibly switching between the acoustic torsion and optical phonon modes), mechanically tunable thermal modulators[131], heat pumps[132] (flowing heat flux in the absence of temperature difference due to

the phononic analogy of berry-phase effect) and quantum heat ratchets[133] (directed flow of current even when the net average temperature difference across the junction $\mathrm{D}T=0$).

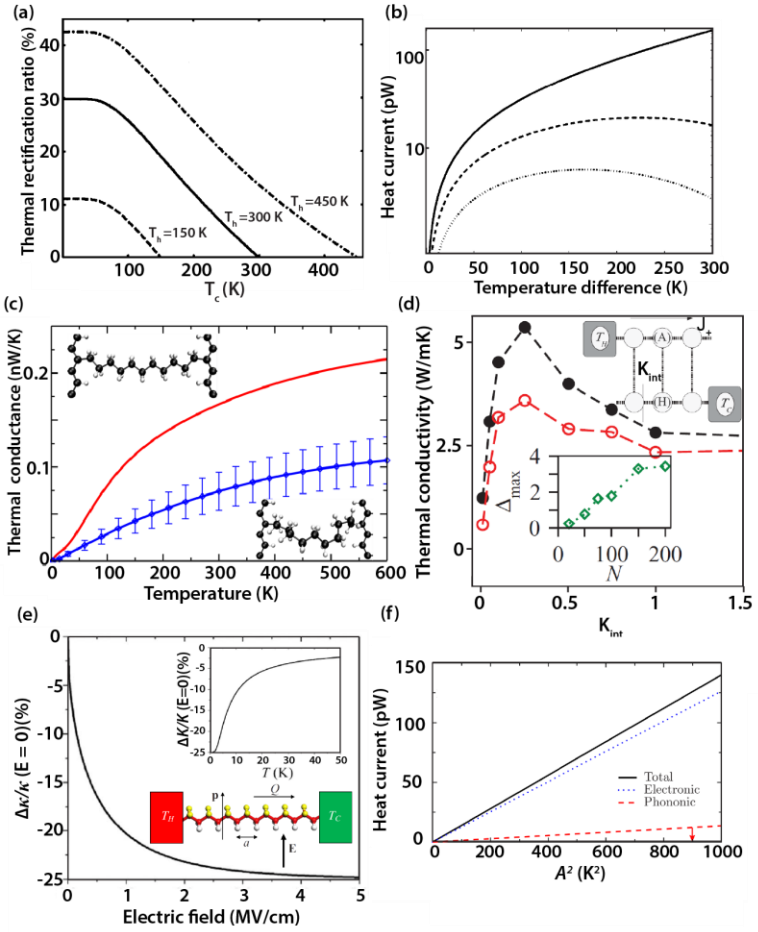

Figure 2.14: Proposed schemes for controlling/modulating thermal transport.
(a) Heat rectification ratio in a two-level phonon model as a function of T_c (cold reservoir temperature) when hot reservoir temperature T_h is fixed (dashed line 150 K, full line 300 K, dash-dotted line 450 K).[127] (b) Predicted negative differential thermal conductance (NDTC) in a two-level phonon model vs. temperature difference across the AMJ.[128] The molecule-reservoir coupling strength is set to be weak (solid line), medium (dashed line), and strong (dotted line). (c) Tunable thermal conductance in a AMJ by mechanical compression/stretching.[131] (d) Heat rectification realized in a two-chain molecule model. Rectification ratio is plotted as a function of the interaction strength between the two chains.[129] One chain (labeled as H in the inset) has only harmonic interactions and the other (A) contains local nonlinearities. Inset shows the molecular length dependent rectification ratio. (e) Modulated thermal conductance by applying electric field to tune the dipole moments of the monomers.[130] Inset shows the modulation ratio vs. temperatures. (f) Heat ratchet effect in AMJs. Predicted heat current (total and the separate electronic and phononic contributions) is plotted as a function of the square of the amplitude (A) of temperature oscillation.[133] The two reservoirs are at temperatures $T_L = T_0 + A\cos(\omega t)$, $T_R = T_0$. The driving frequency is ω = 3.92 GHz, and T_0 = 300 K.

In addition to the studies of thermal transport in short AMJs ($N < 30$), another interesting topic is thermal transport in long polymer molecular chains. Here, computational/theoretical work was mainly inspired by the experimental observation[134] of high thermal conductivity in highly drawn polyethylene (PE) fibers. In contrast to the explorations of thermal transport in 1D chains, long polymer molecules represent realistic 1D systems that can test the limit of Fourier's law. Many researchers[22, 23, 135, 136, 137] have simulated thermal conduction in single polymer chains of various lengths and found that the thermal conductivity is several orders of magnitude higher than that in bulk materials. Similar to the results from the simple 1D lattice model, thermal conductivity increases with molecular length, and even shows divergence in some cases. Particularly, Henry and Chen found the thermal conductivity of a single PE chain can reach 350 W/m·K when the molecular length is longer than 1 μm (Fig. 2.15(a)).[22] Further, Sasikumar and Keblinski[137] studied the role of chain conformation on phonon transport. They found that by introducing gauche conformations (kinks), the curved chain was shown to have much smaller thermal conductance than the straight chain because of the increase of phonon scattering centers (Fig. 15(b)). Further, Liu and Yang[23] found that the polymer chains with aromatic monomers had a thermal conductivity ~5 times larger than that of a PE chain (Fig, 2.15(c), 2.15(d)) and concluded that thermal transport in these long molecular chains was determined by the competition between ballistic and diffusive phonons.

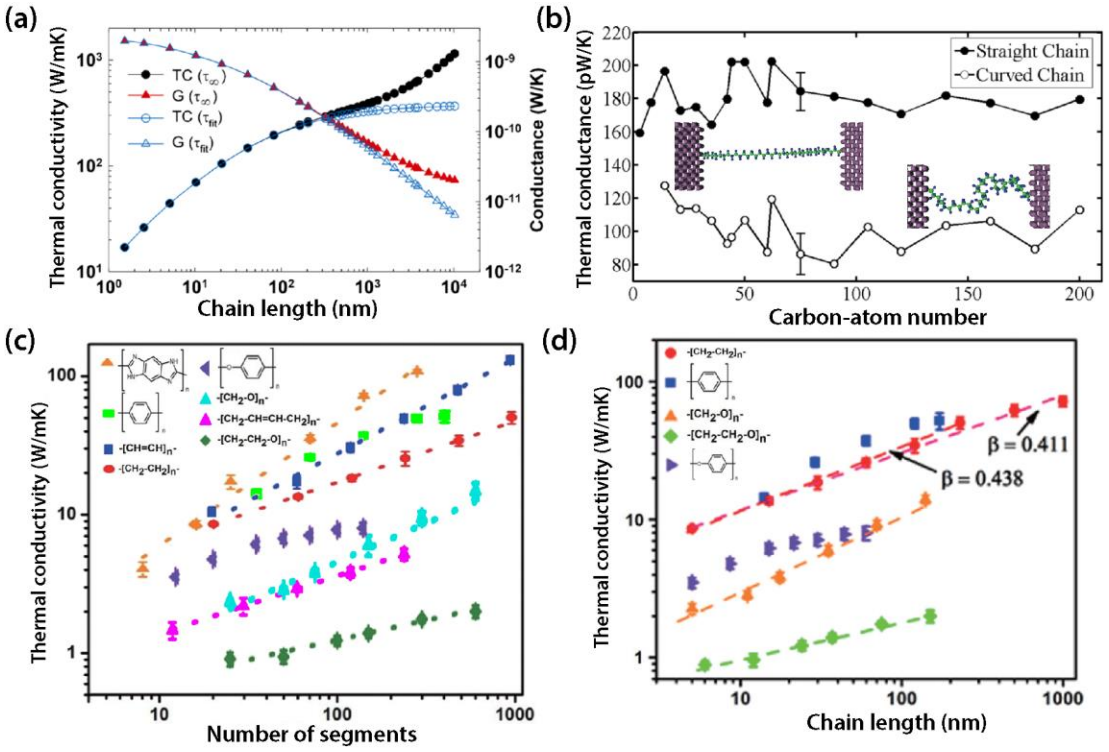

Figure 2.15: Calculated thermal conductance of single polymer molecular chains.
(a) Length dependence of thermal conductivity (circles) and corresponding conductance (triangles) for a single polyethelene (PE) chain.[22] (b) Length dependent thermal conductance of straight (solid circle) and kinked chains (open circles).[137] The ratio of end-to-end distance to coutour length is 0.55 for the kinked chains. (c) Thermal conductivity of single chains of various polymers vs. the number of segments.[23] (d) Length dependent thermal conductivity of various types of polymer chains.[23]

Another topic of interest in the study of thermal transport of molecular junctions or chains is the development of strategies to suppress phononic thermal conductance. This topic is of interest as thermoelectric energy conversion efficiency of molecular devices can be enhanced by successful reduction of phononic thermal conductance. Proposals in this direction include, for example, taking advantage of the degree of mismatch in the vibrational (phonon) density of states of the electrodes (which is effectively continuous) and the molecules (which are discrete)[115, 138] as well as designing π-stacked molecular structures with weak coupling between different parts of the molecules[139] .

2.4.2 Experimental Progress

While computational studies of thermal transport have been pursued for several years, corresponding experimental investigations have begun only recently. The strategy to quantify molecular thermal conductance is conceptually straightforward. An applied temperature difference (analogous to a voltage bias applied during electrical measurements) results in a relatively small heat current (analogous to electrical current) across the AMJs, which need to be measured to quantify thermal conductances. Given the challenges associated with measuring the small heat currents in that arise in AMJs (especially single molecule junctions), experimental studies have been somewhat limited.

The primary platform employed for probing thermal transport in AMJs are SAM based junctions as they provide a well characterized junction structure with a relatively large area over which experiments can be performed.[140] Some of the first transport studies were performed across solid-SAM-liquid junctions. For example, Ge *et al.*[141] studied the thermal conductance in solid-SAM-water junctions. In this experiment the SAM (OTS, C_{18}, PEG-silane, $C_{11}OH$) was bonded to a solid surface (Au or Al) to chemically modify the surface. The measurement of thermal conductance of the junction was performed using the time domain thermoreflectance[142] (TDTR) technique, which characterizes the thermal conductivity of a thin film by measuring the temperature-dependent change of surface reflectance under transient laser heating. They found that the thermal conductance between hydrophilic surfaces and water was several times larger than that between hydrophobic surfaces and water, indicating the important role of the SAM on modulating the interface thermal transport. These findings were also confirmed by Tian *et al.*[143] who studied the thermal transport across solid-liquid interface. They found that by adding a SAM (thiolated alkane molecules) between Au and ethanol the thermal conductance is enhanced 2-5 times, depending on the length of the AMJs.

In addition to the studies of Solid-SAM-liquid configuration, AMJs have also been studied in solid-SAM-solid configurations. Specifically, Wang *et al.*[138] measured the thermal conductance of Au-ADT-GaAs junctions (N = 8, 9 and 10). The molecular junction sample was prepared by a nanotransfer printing technique, where a gold thin film, patterned on a silicon stamp, was transferred onto a SAM chemically bonded to a GaAs substrate. Subsequently, the patterned Au film was employed as a thermometer to measure the thermal conductivity of the SAM junctions using the 3ω method[144]. In this work, the measured thermal conductance was found to be insensitive to the length of the AMJs (Fig. 2.16(a)).

In another work, Wang *et al.*[43] studied thermal transport through long-chain alkanethiols of various lengths that were bonded to a Au substrate (Fig. 2.16(b)). A nonlinear coherent vibrational spectroscopy technique, called time-resolved sum-frequency generation (SFG) technique, was employed to detect the ultrafast thermal induced orientational disorder when heat is transported to the terminal -CH_3 head groups. They found that phonon transport in the alkane chains is ballistic and the thermal conductance, which is estimated to be ~50 pW/K per molecule, is limited by the Au-SAM interface.

These original experiments of thermal transport in solid-SAM-solid junctions not only demonstrated how thermal transport could be systematically probed, but also identified several questions that needed further elucidation. For example: What is the influence of the SAM's molecular structure, the chemical composition of the electrodes and the interactions between the molecule and the electrode on their thermal transport properties? How can the geometry of AMJs be controlled to optimize (maximize or minimize) the thermal conductance? Several studies have been performed to answer these questions and are described below briefly.

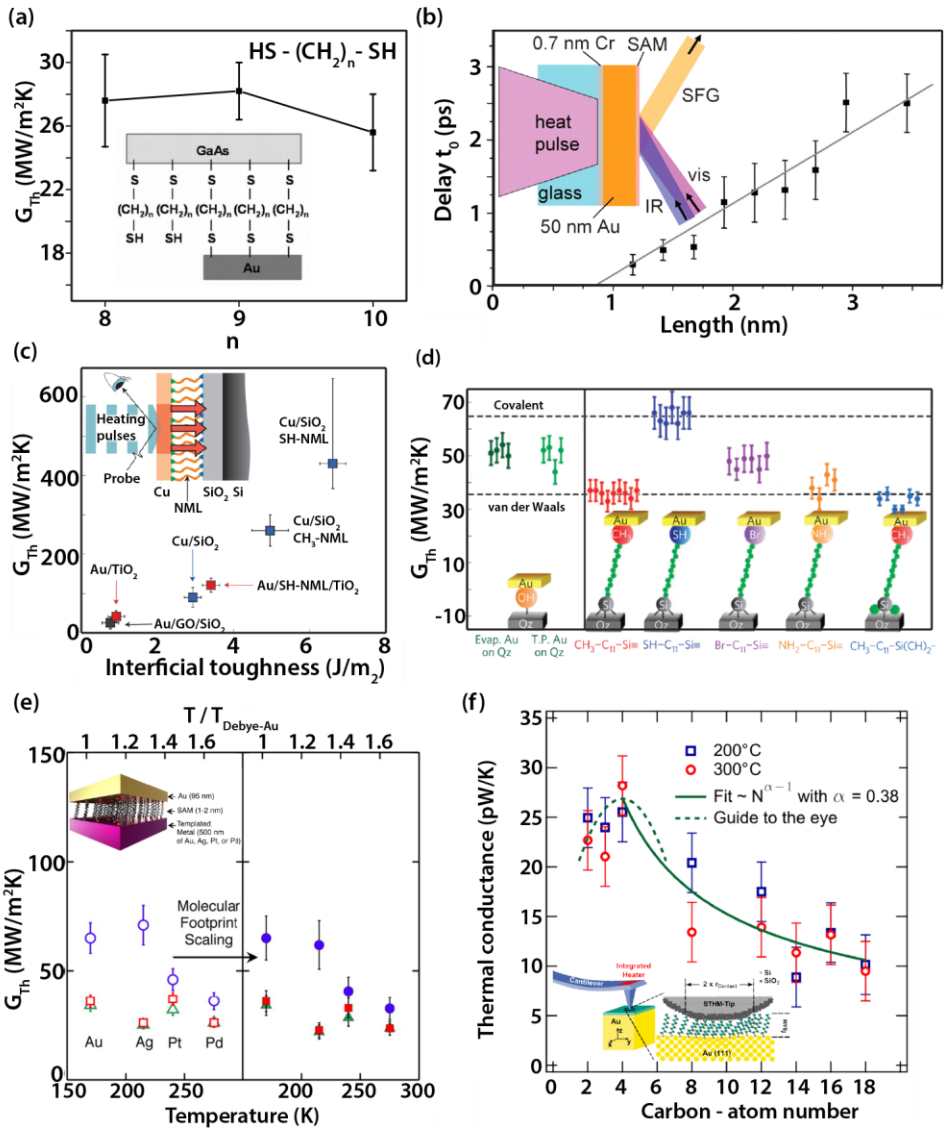

Figure 2.16: Measured thermal transport in SAM based AMJs.
(a) Thermal conductance of Au-alkanedithiol (n = 8, 9, 10)-GaAs junctions at room temperature.[138] Inset: schematic of the sample. (b) Thermal conductance measurement on Au-alkanethiol ($HS-(CH_2)_n-CH_3$, n=5 to 23) junctions.[43] The delay time between the heating laser pulse and the arrival of heat burst at the methyl head group is plotted as a function of the molecular length. Inset: schematic of the experimental set-up. (c) Thermal conductance in metal-SAM-dielectric junctions obtained using the TDTR technique (schematics shown as inset).[145] (d) Measured thermal conductance of SAM junctions for various end-groups.[146] (e) Quantification of impact of vibration mismatch on thermal conductance.[147] The vibrational mismatch is introduced by using different metallic electrodes (with different Debye temperatures, i.e., cut-off phonon mode frequencies). The raw data (left half panel) was re-scaled by the molecular footprint to isolate the effect of the electrode vibrational spectra on thermal conductance (right half panel). (f) Length dependent thermal conductance in Au-alkanethiol-SiO_2 junctions by scanning thermal microscopy (SThM) technique.[148]

O'Brien *et al.*[145] probed the thermal conductance of metal-SAM-dielectric interfaces and compared them to the thermal conductance of metal-dielectric interfaces. The samples were

prepared by assembling different organosilane molecules with identical molecular structure except for the end groups (one with -SH, another with -CH_3) on two different dielectric structures (SiO_2 or TiO_2). By employing the TDTR technique, they demonstrated that the thermal conductance across the interfaces can be significantly increased (more than a factor of 4) by introducing strong bonding organic monolayers to facilitate phonon transport through both metal-molecule and dielectric-molecule interfaces (Fig. 2.16(c)). Specifically, they found that the -SH end-group functionalization is more effective in boosting thermal transport than the -CH_3 end-group functionalization and demonstrated that interfacial thermal conductance can be tuned over an order of magnitude by altering the interfacial bonding strength

In addition to the study of O'Brien *et al.*, Losego *et al.*[146] systematically measured the thermal conductance of Au-SAM-quartz junctions. All the organic molecules studied had a silane group (-SiH_3) at one end, while the other end was varied to be methyl (–CH_3), thiol (–SH), amine (–NH_2), or bromine (–Br). Their measurements of thermal transport revealed that the binding strength had a strong impact on the conductance. Specifically, they found that covalent-like bonds at the interface such as thiol-gold bonds yielded a thermal conductance that was ~2 times higher than that given by van der Waals interactions, such as the cases with a –CH_3 moiety (Fig. 2.16(d)) interacting with Au. Further, they observed a linear dependence of interfacial thermal conductance on the covalent bond density, suggesting that intermolecular interactions do not significantly contribute to thermal transport.

More recently, Majumdar *et al.*[147] studied the impact of vibrational mismatch of electrodes on the thermal transport characteristics of SAM junctions. This measurement was conducted by employing a frequency-domain thermo-reflectance[149] (FDTR) technique. Different from the TDTR technique which records the time domain response of the surface reflectance due

to temperature change, the FDTR technique records the frequency domain response. They found that Au-ADT-Au junctions yield a thermal conductance that is ~2 times higher than Au-ADT-Pd junctions (Fig. 2.16(e)). The ratio of the Debye temperatures of the electrodes that sandwich the AMJs was used as a measure of the vibrational mismatch between the electrodes to explain the differences in the thermal conductance. These studies show that since thermal transport in AMJs is dominated by phonons, the vibrational modes inside the electrodes matter significantly even though the thermal carriers inside the electrodes are electrons.

In addition to the above conclusions Meier *et al.*[148] performed experiments where they probed thermal transport using scanning probes with integrated heater thermometers in a vacuum environment. Their measurements were performed on SAM layers assembled between a Au surface and a silica-coated tip of their scanning probe. Specifically, they created Au-ADT-SiO_2 junctions, where one end group (-SH) was chemically bonded to the Au substrate while the other (-CH_3) was weakly interacting with the tip and studied heat flow from a heated substrate into their tip as the length of the molecules was varied. They found that the thermal conductance of Au-ADT-SiO_2 junctions showed a maxima when the number of carbon atoms (N) was increased from 2 to 4. Upon further increasing N from 8 to 14, the thermal conductance was found to be invariant within measurement uncertainty (Fig. 2.16(f)). This observed length-dependent thermal conductance matched well with the predictions by Segal *et al.*[114]. We note that the advantage of the SThM over the former techniques is the capability to probe thermal transport in a highly localized region (<10 nm).

To summarize, current experimental work has successfully examined thermal transport properties of AMJs in monolayers. However, experimental elucidation of thermal transport in single molecule junctions and single polymer chains has remained inaccessible. Specifically, the

prediction of ultrahigh thermal conductivity in single polymer chains remains unverified. However, noteworthy efforts have succeeded in probing the thermal conductivity of nanofibers of polymer materials.[150, 151, 152] Such polymer nanofibers, which contain thousands or more single polymer chains, have provided an interesting preview of the thermal transport phenomena that arise in single-polymer chain based predictions. However, directly connecting the results from such nanofiber measurements to those of single polymer chains is complicated due to an incomplete knowledge of the crystallinity, orientation of the polymer fibers and the cross-linking between the chains.

2.5 Heat Dissipation, Local Heating and Cooling in Atomic and Molecular Junctions

Electric current flow and heat dissipation are often concomitant and involve complicated interactions among energy carriers. When a current I is driven by a constant bias V applied across a nanoscale junction, the total power dissipation is $Q = IV$. In AMJs created from short molecules, if the transport through the molecular region is elastic, the Landauer approach can be used to describe heat dissipation at the electrodes of the AMJs as described by Eqs. (5) and (6).

Inelastic processes, such as those arising from electron-phonon interactions in the molecular region pose significant challenges to modeling and result in a fraction of the power being dissipated in the molecular region. Given the small heat capacity of the molecules even a small amount of heat dissipation leads to a significant increase in the local kinetic energy of atoms in the molecular region. Such scenarios raise important questions regarding the validity of the notion of temperature in this strongly non-equilibrium state. It is well known that the classical definition of temperature is applicable to only systems in equilibrium and is given by $T = \frac{\partial U}{\partial S}$, where U is the internal energy of the system and S is its entropy. Therefore, the description of non-equilibrium scenarios that arise during dissipation requires the definition of an

operational temperature (also called the "effective temperature"). Below, we provide a description of the computational and experimental work that was performed to understand heat dissipation in AMJs.

2.5.2 Theoretical Results

Various computational works have investigated heat dissipation and local heating effects in AMJs and the microscopic mechanisms behind these phenomena. For example, heat dissipation in AMJs was studied by Zotti *et al.*[39] based on the Landauer picture (Fig. 2.17). They performed *ab initio* transport calculations and showed that heat dissipation in short molecular junctions, where transport is expected to be elastic, is intimately related to the electronic structure of AMJs. Specifically, they found that the heat dissipated in the two electrodes of a AMJ is in general asymmetric and the degree of asymmetry is determined by the sign and magnitude of the thermopower of the AMJs.

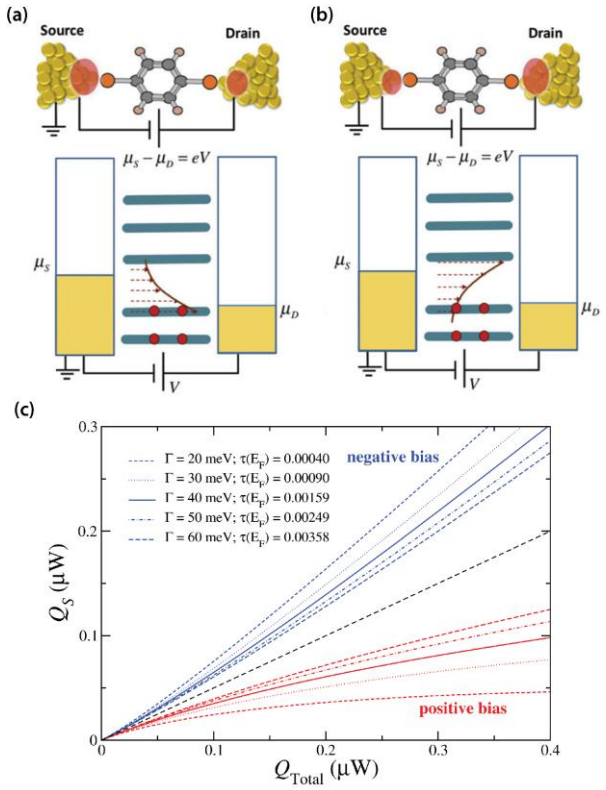

Figure 2.17: Heat dissipation in AMJs and the calculated heat dissipation based on the Landauer model.
(a) Schematic describing asymmetric heat dissipation in the electrodes of a AMJ. The potential drop across the left electrode-molecule interface is more than that across the right one. (b) Schematic of asymmetric heat dissipation in a AMJ where the voltage drop is larger at the interface with the right electrode. The potential drop across the right interface is more in this case. (c) Calcualted heat dissipation asymmetry for different molecule-electrode coupling strengthes. Q_{Total} is the total heat dissipation and Q_S is the heat dissipated in the source electrode[39].

Heat dissipation in systems featuring inelastic effects (non-Landauer picture, Fig. 2.18(a)) was studied by Segal and Nitzan[153] where they estimated the fraction of heat dissipated in the molecular region and its dependence on the molecular length and coupling strength of the molecule with the electrodes. By comparing the predictions from different models (Fig. 2.18(b)), they found that the classical heat conduction theory underestimates the temperature rise in the molecular region, suggesting the need to apply microscopic models to understand the phonon energy transport in AMJs.

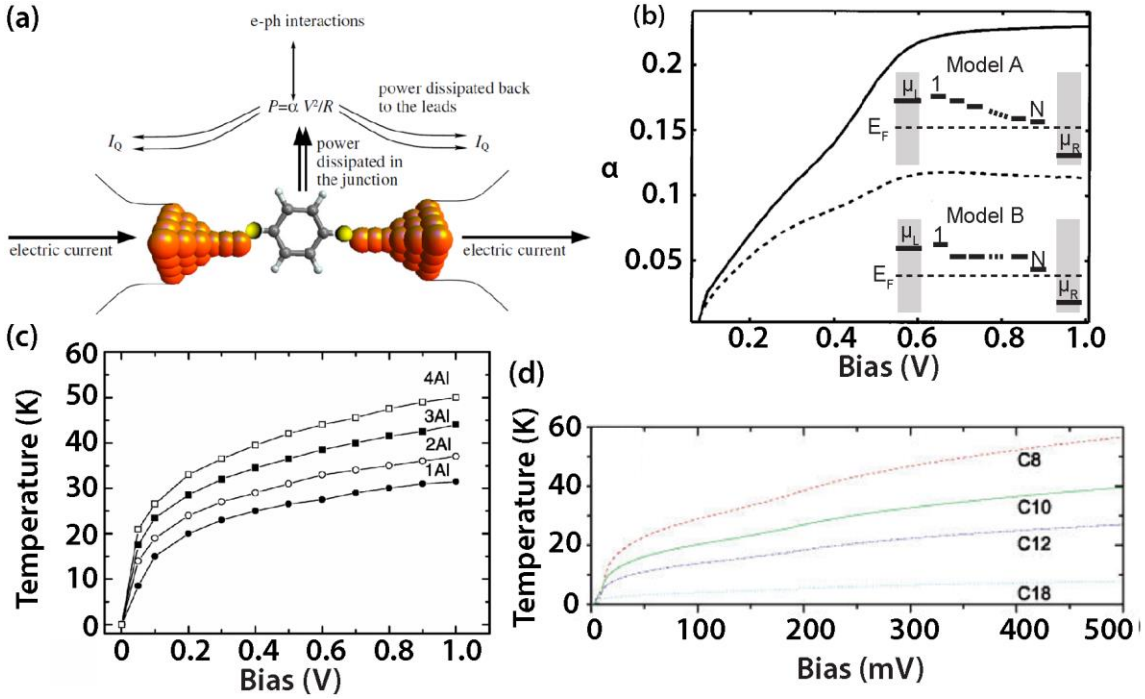

Figure 2.18: Computational results on heat dissipation and local temperature in molecular junctions
(a) Schematic of heat dissipation in molecular junction due to inelastic scattering.[17] The total heat dissipation is V^2/R, of which $\alpha V^2/R$ is dissipated in the molecular region while the rest in the electrodes. (b) Predicted heat dissipation in molecular region (α) based on different models of potential distribution within the junction.[153] (c) Local temperature increase calculated for atomic chains (with 1 to 4 Al atoms) under different biases.[154] (d) Local temperature increase as a function of bias voltage using alkanethiols of various length.[155]

Based on first principle approaches, Pecchia *et al.*[156] presented a theory of heat dissipation and local temperature of AMJs. They found that local temperature is strongly influenced by electron-phonon scattering. By applying this theory to metal-styrene-Si junctions, they found that the local temperature sharply increases after a critical bias, which indicates the strong excitation of the lowest vibrational mode in the styrene molecules. Along these lines, Galperin *et al.*[157] also studied heating in current-carrying AMJs and obtained a unified model to describe both heat dissipation and the electronic and vibrational contributions to heat conduction in AMJs.

In addition to the contribution of electron-phonon scatterings to local heating, the effect of electron-electron scatterings has also been studied by D'Agosta *et al.*[158] who derived a model to describe the local temperature based on an electron liquid based hydrodynamic approach. They found that in AMJs the electron-electron interactions, which could have comparable scattering rate as the electron-phonon interactions, may play an important role in determining the local temperature.

The effect of molecular length on local heating was also studied by Yang et al.[154] who calculated the local temperature increase in AMJs containing 1 to 4 Al atoms. Specifically, they found that at a given bias the local temperature increase is larger in longer chains (Fig. 2.18(c)). Further, Chen *et al.*[155] estimated the local heating of various ADT AMJs (Fig. 2.18(d)). They found that in the presence of good molecule-electrode coupling the local temperature increase was smaller when the molecular length increases. Further, local temperature increase was predicted to be insensitive to the molecular length when the molecule-electrode coupling was weak. These works suggest that inelastic interactions inside the molecule and heat dissipation in the electrodes play important roles in determining the local temperature.

In addition to studies of local heating effects, local cooling in AMJs has also attracted much attention.[159, 160, 161, 162, 163] For example, Galperin *et al.*[159] proposed two cooling mechanisms: one based on the depletion of hot electrons inside the high potential electrode; the other based on inelastic electron transport. The former achieved a cooling effect by shifting the non-equilibrium electron distribution, which defines the effective temperature. The latter leveraged the inelastic tunneling in which the electron extracts energy from vibrational modes while transmitting through the junction. More recently, Lykkebo *et al.*[163] studied local cooling effects in realistic AMJs. They presented cooling schemes based on inelastic electron tunneling and found that under voltage biases across the AMJs the local temperature can potentially reach values below the ambient temperature. This study pointed out the possibility of realizing local molecular cooling by rationally designing the AMJs.

2.5.2 Experimental Progress

Several experimental studies have been performed to quantify heat dissipation in AMJs and obtain insights into the inelastic processes in the molecular region and the electrodes. One of the first studies in this area was conducted by Huang *et al.*[164] who studied current induced local heating in AMJs by measuring the force required to break the molecule-electrode covalent bonds. By taking advantage of the fact that the chemical bond breakdown process is thermally activated, the authors were able to define an effective temperature of the junction as a function of the applied bias. Based on their analysis they suggested that, under ambient conditions, a ~30 K temperature increase is generated when a bias of 1 V is applied across Au-octanedithiol-Au junctions (Fig. 2.19(a)).

The instability of AMJs induced by applied voltage biases has been studied[166, 167] by quantifying the frequency of two-level fluctuations (TLF) in conductance of AMJs.[165, 166] It was

found that the frequency of the conductance fluctuations increase with increasing bias and the effective temperature of the AMJ is proportional to $\sqrt{V}$ (Fig. 2.19(b)). Along the same lines, Tsutsui *et al.*[167] reported an estimation of the local temperature by fitting the molecular junction lifetime to a model that takes into consideration both the applied bias and the effective temperature. From these studies it was found that Au-BDT-Au molecule junctions were heated up by ~200 K at room temperature under an applied bias of ~1V (Fig. 2.19(c)). Further, inelastic electron tunneling spectroscopy[168] (IETS) studies were used to study the onset of heat generation in AMJs due to the excitation of the lowest energy phonon mode.

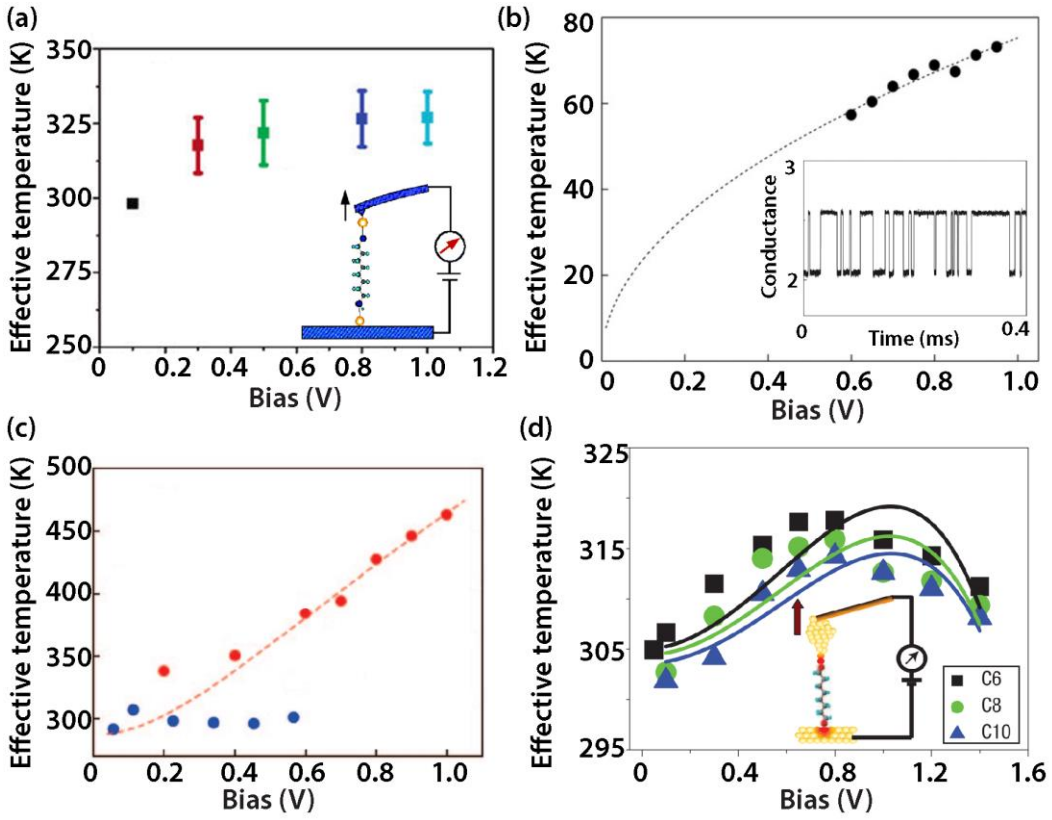

Figure 2.19: Measured effective local temperature of AMJs.
(a) Local temperature of octanedithol under different biases meausured by AFM break junction technique at room temperature.[164] The junction breaking force is directly measured and was used to calculate the local temperature. (b) Local temperature ($T_{electrode}$ = 4.2 K) of Au atomic junctions under different biases.[166] The frequency of two-level-fluctuations (TLFs) of conductance was used as an indicator of the local temperature. (c) Local tempearature ($T_{electrode}$ = 287 K) of BDT AMJ(red) and Au atomic junction (blue).[167] The junction lifetime was used to deduce the local temperature. (d) Bias dependent local temperature of ADT (N = 6, 8, 10).[169] $T_{electrode}$ = 300 K, and STM break junction technique was used to measure the junction streching length for estimating the local temperature.

Huang *et al.*[169] also studied the effective temperature of a series of ADT AMJs by using the STMBJ technique (Fig. 2.19(d)). In this work, the stretching lengths of a AMJ at breakdown were measured and fitted to a model that describes the dependence of stretching length on effective temperature. They found that the local temperature increases with the applied bias until ~0.8 V and then decreased in the presence of higher biases, suggesting that strong electron-electron scattering led to local ionic cooling. Further, they studied the dependence of effective temperature on the molecular length and found that at a given bias the effective temperature was higher for shorter AMJs, indicating that electron-phonon scattering is reduced when AMJs were longer.

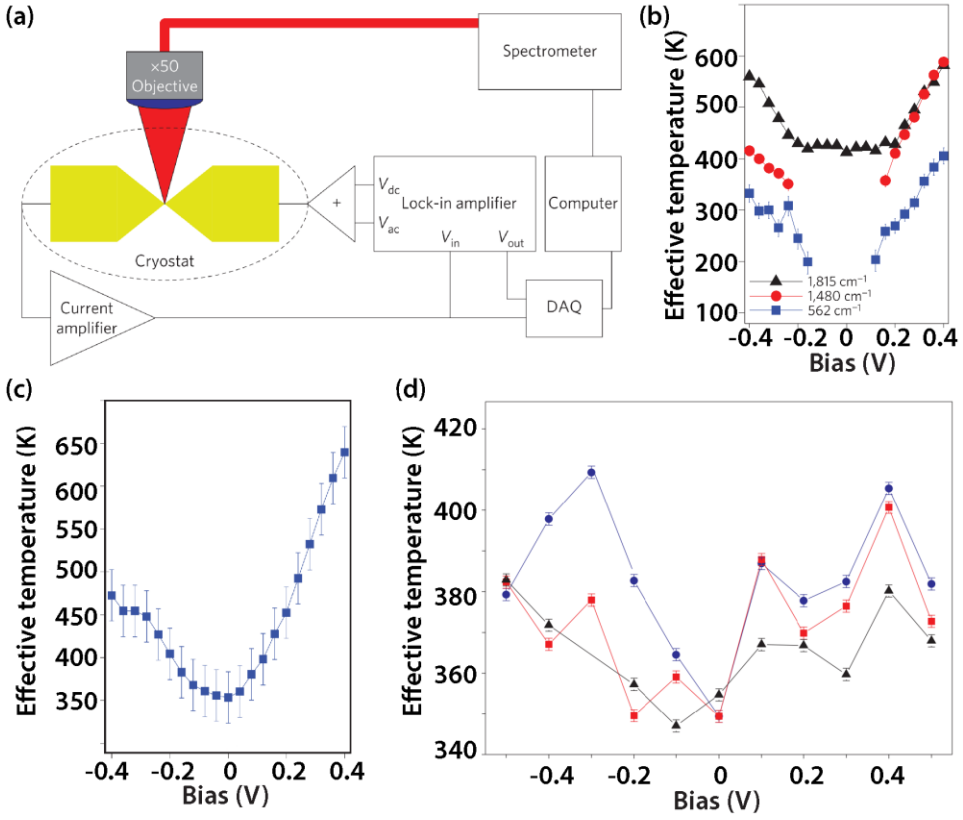

Figure 2.20: Local temperature measurements from surface-enhanced Raman spectroscopy.
(a) Schematic of the electrical and optical measurements.[170] (b) Bias-dependent phononic effective temperature in OPV3 molecule for different phonon modes.[170] (c) Bias-dependent electronic effective tempreature of OPV3 molecule.[170] (d) Phononic effective temperature in BPDT molecule for different phonon modes under different bias voltages.[171]

Besides the measurements of local temperatures using break-junction techniques, Ioffe *et al.*[171] and Ward *et al.*[170] also leveraged surface-enhanced Raman spectroscopy to study this problem (Fig. 2.20). In their works, the Stokes (S) and anti-Stokes (AS) components of the Raman scattering was measured and the AS/S ratio, which is temperature dependent, was used to estimate the local heating effects. Specifically, Ward *et al.*[170] characterized both the effective vibrational and electronic temperatures of OPV3 molecular junctions and observed a pronunced heating effect with ~200 - 300 K local temperature increase in the presence of applied bias ~0.4 V. In contrast, Ioffe *et al.*[171] reported a much smaller temperature increase (30 - 50 K) for the same bias in DBDT AMJs. These studies indicate that local Raman spectroscopy may serve as a valuable technique to probe local temperatures at the atomic scale.

In addition to these studies, Schulze *et al.*[172] used a STM to measure heating and heat dissipation processes in single C_{60} molecules. Specifically, they observed the thermally induced decomposition of molecular structures. In the tunneling regime, they found that dissipation of ~20 μW of power was sufficient to cause strong molecule heating and a breakdown of the fullerene cage. In contrast they found that when the molecule was in good contact with both the electrodes a larger amount of power was necessary for the breakdown of the fullerene cage. Given these observations they concluded that in the case of junctions with good contact with electrodes either the heat generation in the molecule was less effective or the heat dissipation through phonon-electrode coupling was stronger.

To directly quantify heat dissipation in AMJs, Lee *et al.*[173] employed scanning probes that featured a nanoscale thermocouple integrated into the tip of the probe (Fig. 2.21). By measuring the temperature rise in the tip under positive and negative applied biases they were able to identify the asymmetric heat dissipation characteristics in the electrodes of the short

molecular junctions created with benzenediisonitrile (BDNC) and benzenediamine (BDA) molecules. Similar measurements performed using gold atomic junctions showed no significant asymmetries. The authors combined their measurements of asymmetry with first principle calculations to show that heat dissipation asymmetries were related to the sign and the magnitude of the Seebeck coefficient[39]. Specifically, they concluded that, under an applied bias V, the difference between the heat dissipated in the left electrode (Q_L) and that in the right electrode (Q_R) is given by:

$$Q_L(V) - Q_R(V) \approx 2G_e TSV + O(V^3) \tag{11}$$

where S is the Seebeck coefficient of the junction, T is the absolute temperature and G_e is the electrical conductance of the junctions.

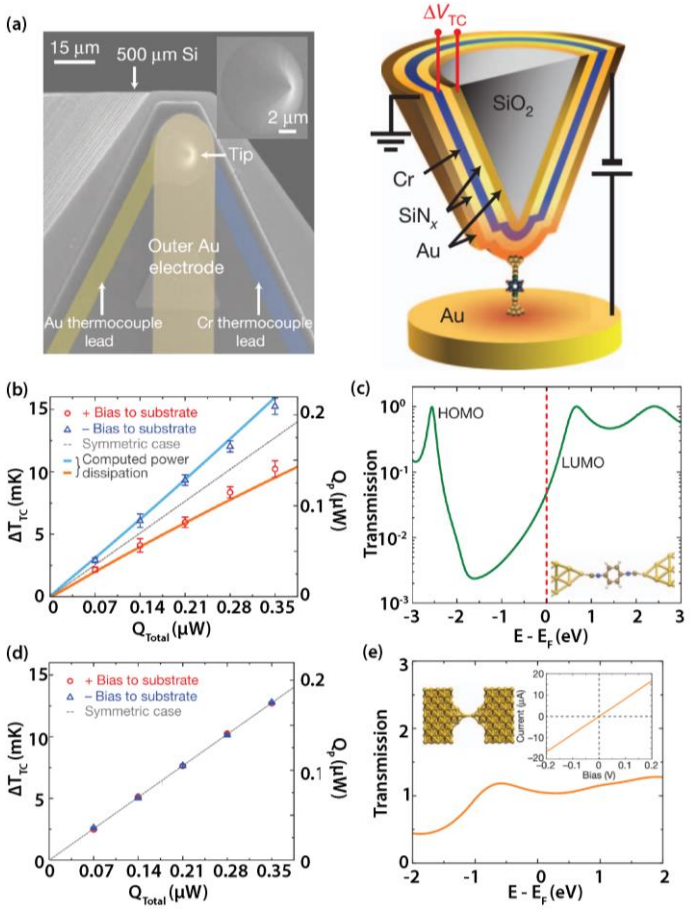

Figure 2.21: Direct measurement of the heat dissipation in single atomic and molecular junctions using scanning thermal probes with intergrated thermocouple.
(a) SEM image (left panel) and schematic (right panel) of the SThM probe featuring an embeded nanoscale thermocouple (Au-Cr) to record the temperature change of the tip due to dissipated heat. (b) Measured asymmetric heat dissipation in the electrodes of a Au-BDNC-Au junction. (c) Calculated transmission function of the Au-BDNC-Au junction. (d) Symmetric heat dissipation observed in the electrodes of Au atomic junctions. (e) Calculated transmission function for Au-Au atomic junctions[173].

We note that in the experiments discussed above, some were aimed at resolving the inelastic scattering mechanisms in the molecular regions of AMJs, while others focused on resolving heat dissipation in the electrodes and assumed that there is negligible dissipation in the molecular regions. These goals don't necessarily contradict each other: as discussed above, the power supplied to sustain the electron flow in AMJs must be dissipated in either the electrodes or the molecular region, or both. The heat dissipation in the molecular region of short AMJs is usually a very small portion of the total heat dissipation. But even such minute levels of dissipation cause large increases in the local temperature.

2.6 Conclusion Remarks

Experimental interrogation of thermoelectric energy conversion, heat transport and heat dissipation in AMJs poses several challenges overcoming which is critical to testing current predictions and stimulating future theoretical and computational work. We conclude this chapter by discussing some outstanding challenges.

A key challenge in thermoelectric energy conversion is to experimentally demonstrate large thermoelectric efficiencies (i.e., ZT values >1) in AMJs. While several computations have suggested the feasibility of achieving efficient and/or high power output thermoelectric energy conversion experiments have so far failed to achieve this goal. Further development of thermoelectric measurements schemes, especially three terminal techniques, may be required to successfully explore the limits of thermoelectric energy conversion in AMJs. Moreover, it is also

important to explore strategies for developing thermoelectric devices/materials where AMJs form the functional subunits.

Probing thermal transport in single AMJs and polymer chains is critical for achieving efficient thermoelectric energy conversion and for understanding the physics of heat transfer in these fundamentally different structures. While ensemble based experiments (such as in SAM and polymer nanofibers) have made impressive progress in understanding thermal transport properties they fail to reveal heterogeneities and can only reveal averaged properties. Single-molecule thermal transport measurement will enable direct comparisons among multiple theories in this field and help build guiding principles for designing AMJs for optimal thermal transport.

Another topic of interest is to probe heat dissipation and measuring local temperatures. Existing experimental approaches are not completely capable of resolving the validity of competing theoretical models. To overcome this challenge, high resolution heat dissipation measurements at the single-molecule level are required. Such measurements will enable establishing a precise limit for the fraction of heat dissipation in the molecular region and will play a critical role in verifying the proposed models for heating/cooling of molecules directly.

Chapter 3: Quantized Thermal Transport in Single Atom Junctions

Reproduced with permission from *Science*. See Ref.[174]

Longji Cui, Wonho Jeong, Sunghoon Hur, Manuel Matt, Jan C. Klöckner, Fabian Pauly, Peter Nielaba, Juan Carlos Cuevas, Edgar Meyhofer, Pramod Reddy

3.1 Abstract

Thermal transport in individual atomic junctions and chains is of great fundamental interest due to unique quantum effects expected to arise in them. Here, by employing novel, custom-fabricated, picowatt-resolution calorimetric scanning probes, we measure the thermal conductance of gold and platinum metallic wires down to single-atom junctions. Our work reveals that the thermal conductance of gold single atom junctions is quantized at room temperature and shows that the Wiedemann-Franz law, which relates the thermal and electrical conductivities in metallic materials at the macroscopic length scale, is satisfied even in single-atom contacts. Furthermore, we quantitatively explain our experimental results within the Landauer picture for quantum thermal transport by applying state-of-the-art first principle calculations. The experimental techniques reported here will enable thermal transport studies in atomic and molecular chains, which is key to investigating numerous fundamental issues that have remained experimentally inaccessible.

3.2 Introduction

The study of thermal transport at the nanoscale is of critical importance for the development of novel nanoelectronic devices and holds promise to unravel quantum phenomena that have no classical analogues [175, 176, 177]. In the context of nanoscale devices, metallic atomic-size contacts [72] and single-molecule junctions [178] represent the ultimate limit of miniaturization and have emerged as paradigmatic systems revealing novel quantum effects related to charge and energy transport. For instance, transport properties of atomic-scale systems such as electrical conductance [179], shot noise [180, 181], thermopower [61, 70, 96] and Joule heating [173] are completely dominated by quantum effects, even at room temperature. Therefore, they drastically differ from those of macroscale devices. Unfortunately, the experimental study of thermal transport in these systems constitutes a formidable challenge and has remained elusive to date in spite of its fundamental interest [17].

Probing thermal transport in junctions of atomic dimensions is crucial for understanding the ultimate quantum limits of energy transport. These limits have been explored in a variety of microdevices [182, 183, 184, 185, 186] where it has been shown that, irrespective of the nature of the carriers (phonons, photons or electrons), heat is ultimately transported via discrete channels. The maximum contribution per channel to the thermal conductance is equal to the universal thermal conductance quantum $G_{0,Th} = \pi^2 k_B^2 T/3h$, where k_B is the Boltzmann constant, T is the absolute temperature and h is the Planck's constant. However, observations of quantum thermal transport in micro-scale devices were only possible at sub-Kelvin temperatures and other attempts at higher temperature regimes have yielded inconclusive results[187].

The energy level spacing in metallic contacts of atomic-size is of the order of electron volts, i.e., much larger than thermal energy, therefore these junctions offer a unique opportunity to explore whether thermal transport can still be quantized at room temperature. However,

probing thermal transport in atomic junctions is challenging due to technical obstacles in reproducibly creating stable atomic junctions, while measuring the miniscule heat currents flowing through the atomic chains.

3.3 Experimental Results and Analysis

We present an experimental platform that allows us to measure the thermal conductance of metallic wires down to the single-atom limit. With this technique we were able to observe quantized thermal transport at room temperature. Specifically, we developed an approach that employs custom-fabricated calorimetric scanning thermal microscopy (C-SThM; Fig. 3.1) probes, which feature a very large thermal resistance ($R_P \sim 1.3 \times 10^6$ K/W) and high resolution Pt thermometers with temperature resolution (ΔT_{min}) of ~0.6 mK in a 10 Hz bandwidth[188, 189]. These characteristics enable thermal conductance measurements with ~25 pW/K resolution, when a temperature bias of ~20 K is applied across atomic junctions. We achieved the large thermal resistance by incorporating long, "T" shaped beams with a small cross-sectional area, which also enable a very high stiffness (>10^4 N/m in the normal direction). Both these features are critical for accomplishing atomic junction thermal measurements. The C-SThM probes also feature a sharp metallic tip that we coated with Au or Pt, but can also be coated with other metals.

Our strategy for quantitatively measuring the thermal conductance of atomic junctions is depicted in Fig. 3.1A. We heated the Au substrate to a temperature T_S = 315 K, while the probe is connected to a thermal reservoir at T_P = 295 K. We then displaced the probe towards the heated substrate by piezoelectric actuation until we reached an electrical conductance of $4G_0$, with

$G_0 = \frac{2e^2}{h} \approx (12.9k\Omega)^{-1}$being the electrical conductance quantum. This electrical conductance signals the formation of a Au-Au contact involving several atoms as established by past work [72].

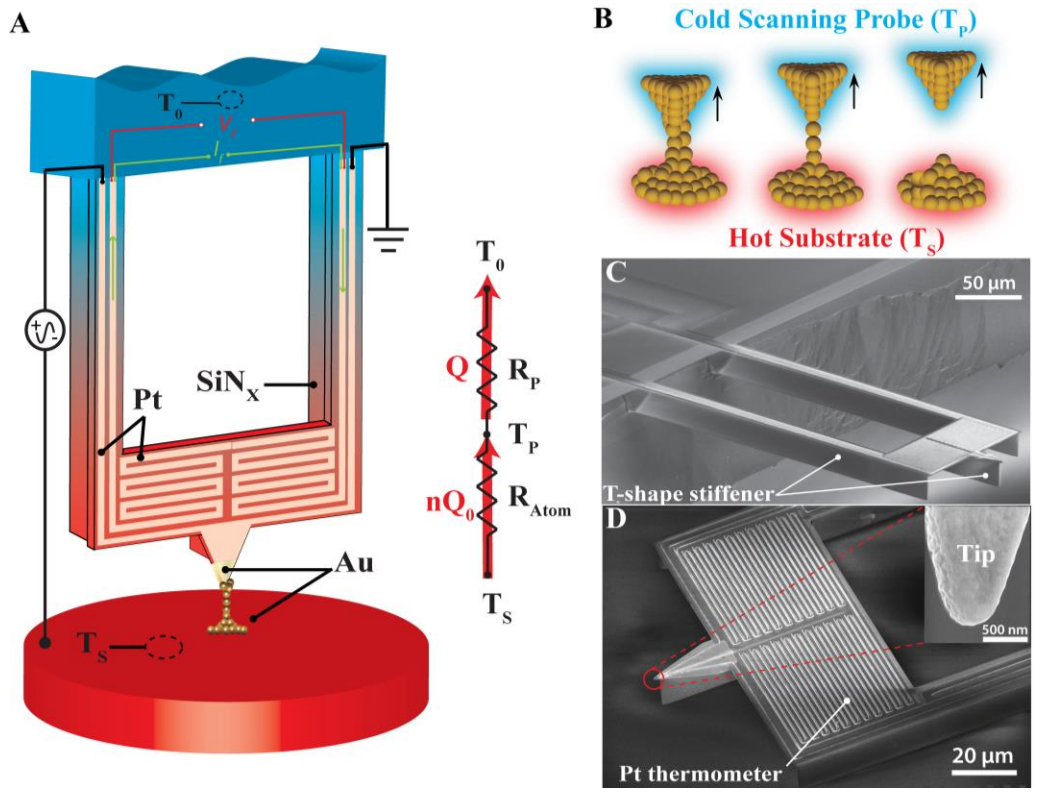

Figure 3.1: Experimental set-up and SEM images of the scanning thermal probes.
(A) Schematic of a calorimetric scanning thermal microscopy (C-SThM) probe, which is used to make atomic junctions with a heated metallic substrate. The tip and substrate coatings can be chosen to be either Au or Pt. The electrical conductance of the tip-substrate junction is monitored by applying a small sinusoidal voltage bias and measuring the resultant current. The resistance of the Pt resistance thermometer is monitored by applying a sinusoidal current and recording the voltage output. Thermal resistance network describes the resistances of the atomic chain and the scanning probe, as well as the heat current flow (red arrow). (B) Schematics of the atomic chains forming, narrowing, and breaking during the withdrawal of the probe from the heated substrate. (C) SEM image (side view) of a scanning probe with two long and stiff "T" shaped SiN beams. (D) SEM image (top view) of the scanning probe, featuring a Au coated tip (inset) and a serpentine Pt thermometer.

We measured the probe-substrate electrical conductance by applying a small sinusoidal voltage bias of amplitude 1 mV at a frequency of 10 kHz and recording the amplitude of the resultant electric current via a lock-in amplifier . Once we reached the threshold conductance, we withdrew the probe slowly from the substrate at a rate of 0.05 nm/s. During this process, the probe-substrate contact region is expected to become more constricted until it forms a single-

atom wide junction, which is broken upon further withdrawal (Fig. 3.1B) [62]. We concurrently performed thermal conductance measurements by continuously measuring the change in probe temperature (ΔT_P) in response to heat flow (Q) through the atomic junction. We measure the probe temperature by monitoring the change in the resistance of the embedded Pt resistance thermometer via a sinusoidal electrical current of fixed amplitude (10 μA) and frequency (1 kHz) supplied to the probe while measuring the voltage drop across the resistor.

From the resistance network (Fig. 3.1A), we directly related the thermal conductance (G_{Th}) of the atomic junctions to ΔT_P by $G_{Th} = \Delta T_P / [R_P(T_S - T_P - \Delta T_P)]$, where R_P was 1.3×10^6 K/W. Representative thermal (red) and electrical conductance (blue) traces show that the electrical conductance decreases in discrete steps (Fig. 3.2A). Many of the curves exhibit preferential conductance values that occur at integer multiples of G_0 as expected from past work [72]. The corresponding thermal conductance curves closely correlate to the electrical conductance curves. Further, several of the thermal conductance curves show steps with preferential conductances a $2\pi^2 k_B^2 T/3h$, a value that is twice the quantum of thermal conductance ($G_{0,Th}$). The factor of two here is a consequence of the spin degeneracy in electron transport and is not present in the usual definition of $G_{0,Th}$ because it was introduced in the context of phonon transport, where spin degeneracy is absent.

Past studies [190, 191, 192] on electrical conductance quantization established that the presence of plateaus in the conductance traces is insufficient evidence of quantization. Definitive conductance quantization requires an unbiased statistical analysis from a large data set. We obtained ~2000 consecutive electrical and thermal conductance traces with the procedure outlined above, which yielded electrical and thermal conductance histograms with clear peaks at $1G_0$ and $2G_{0,Th}$, respectively (Fig. 3.2C, Fig. 3.2D). The thermal conductance histogram exhibits

more broadening in comparison to its electrical counterpart because the time constant for our thermal measurements (~25 ms) is larger than that for our electrical measurements (~10 μs).

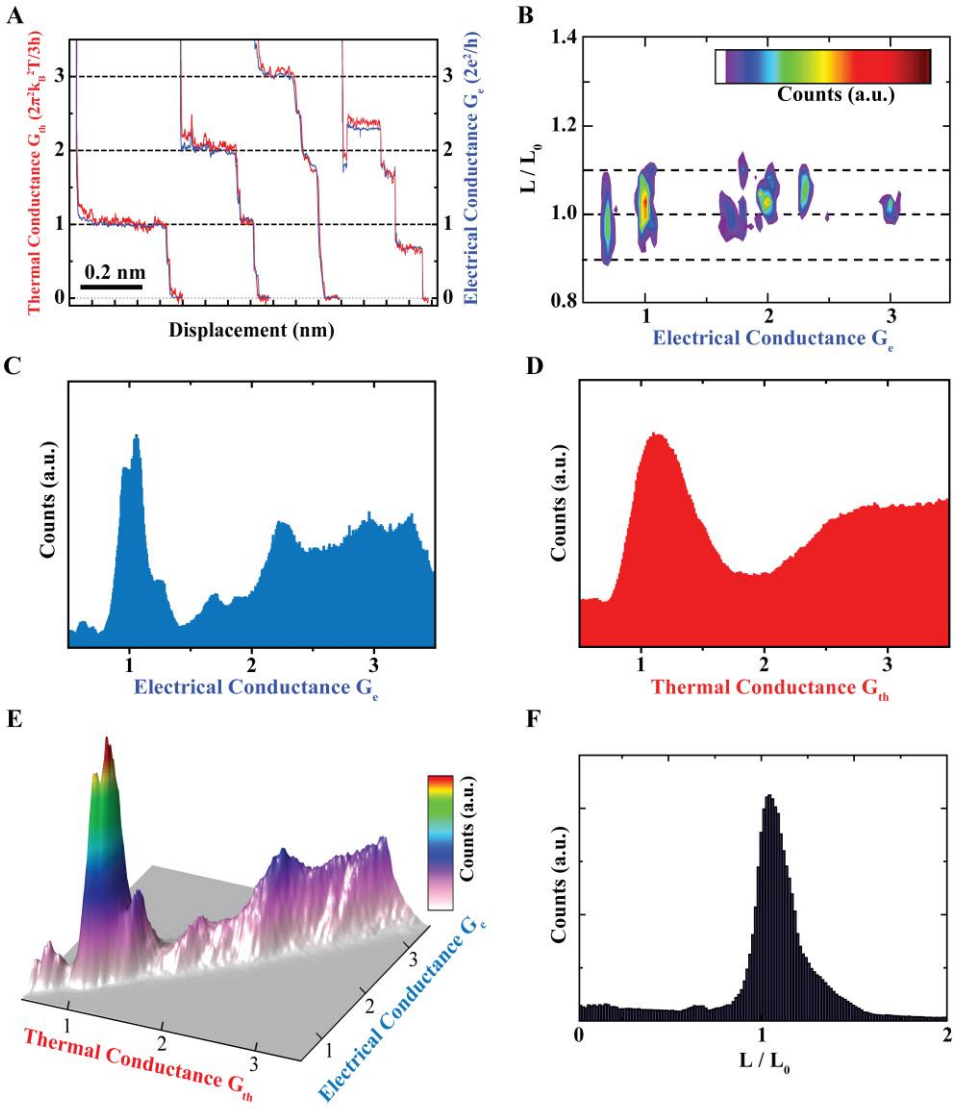

Figure 3.2: Thermal conductance quantization in Au atomic junctions.
(A) Representative traces of thermal and electrical conductances measured while reducing the transverse constriction of Au atomic junctions by displacing the Au tip of C-SThM probe away from the Au substrate. The thermal (red line) and electrical conductance (blue line) traces are plotted in units of twice the thermal conductance quantum and electrical conductance quantum, respectively. (B) Histogram of the ratio of the thermal conductance to electrical conductance is in good agreement with the Lorenz number (L/L0). Color bar: number of counts increase from white to red. (C, D) Electrical and thermal conductance histograms obtained from 2000 concurrently measured electrical and thermal conductance traces (without any data selection) similar to those shown in (A). (E) A joint plot of the electrical and thermal conductance traces shows the tight correlation between the occurrence of electrical and thermal conductance quantization. (F) Analysis of the data in (C) and (D) shows that the Wiedemann-Franz law accurately predicts the thermal conductance of Au atomic junctions (the peak is at 1.06).

The close correlation between the thermal and electrical conductances (Fig. 3.2A) provides important information regarding the validity of the Wiedemann-Franz law, which relates the electronic contribution of the thermal conductance, $G_{Th,e}$, to the electrical conductance G_e via: $G_{Th,e} = L_0 T G_e$ where $L_0 = (\frac{\pi^2}{3})(k_B/e)$ is the Lorenz number [193]. Since this basic law was originally derived with semi-classical arguments and is approximately obeyed in macroscopic wires of standard metals [193], it is unclear whether it should remain valid in metallic atomic junctions where the transport mechanisms are different[31]. To test the validity of the Wiedemann-Franz law in atomic junctions we used the data in Fig. 3.2A to obtain the Lorenz ratio $L/L_0 = G_{Th}/L_0 G_e T$, as a function of G_e. Here, T is the average temperature of the tip and the sample and equals 305 K. This process was repeated for each set of curves shown in Fig. 3.2A and the data from all the four curves was collected into a two dimensional histogram shown in Fig. 3.2B. It is clear from the data that the value of L/L_0 is very close to 1.

We plotted a 3D histogram created from 2000 concurrently measured electrical and thermal conductance traces without any data selection (Fig. 3.2E). The histogram features a large peak corresponding to (G_0, $2G_{0,Th}$), showing that the electrical and thermal conductance quantization occurs concurrently and that the quantized state is a statistically favored atomic configuration. This close correlation is also reflected in the 2D histogram (Fig. 3.2F) where we computed $L/L_0 = G_{Th}/L_0 G_e T = 1.06$ as mean value from the 2000 traces. The small increase above 1.00 is primarily due to contributions from phonons to the thermal conductivity, which we estimate to add ~5 - 10% (see below). The increase in L/L_0 can also have small contributions (~10 – 20 pW/K) from near-field radiative heat transfer and even smaller contributions from the overestimation of the thermal conductance during periods of rapid transition in the electrical conductance when the thermal response lags the electrical response.

To identify the origin of our quantization observations we employed custom-developed methods to compute the thermal and electrical conductance of Au atomic-size contacts within the framework of the Landauer-Büttiker formalism for coherent transport. We exactly simulated the experiments via a combination of molecular dynamics (MD) [194, 195], density functional theory (DFT) [41, 196], and non-equilibrium Green's function techniques to describe the contributions of both electrons and phonons to the thermal conductance. Our MD simulations show that when the electrical conductance is G_0, the geometry of the atomic junction typically corresponds to atomic "dimer" bridge geometries similar to that shown in the inset of Fig. 3.3A. Our DFT-based calculations (Fig. 3.3A) for the electrical and thermal transport for a dimer geometry show that the thermal conductance at room temperature is dominated by the electronic contribution, with phonons giving only ~4% of the total signal, which is similar to the case of bulk Au wires [197]. We also found that the electronic contribution at room temperature in this example is $G_{Th,e} \approx 0.59\, nW/K$, which is close to twice the thermal conductance quantum. The reason for this quantized thermal conductance is apparent from Fig. 3.3B where we show that electronic transmission is dominated by a single (spin-degenerate) conduction channel and has a value very close to 1. This fact, taken together with the smooth energy dependence of the electronic transmission around the Fermi energy, leads to excellent agreement with the Wiedemann-Franz law: $G_{Th,e} \approx L_0 T G_e \approx 2G_{0,Th}$. Therefore, we conclude that for one-atom Au junctions the observed thermal conductance quantization is intricately linked to the electronic structure of this monovalent metal.

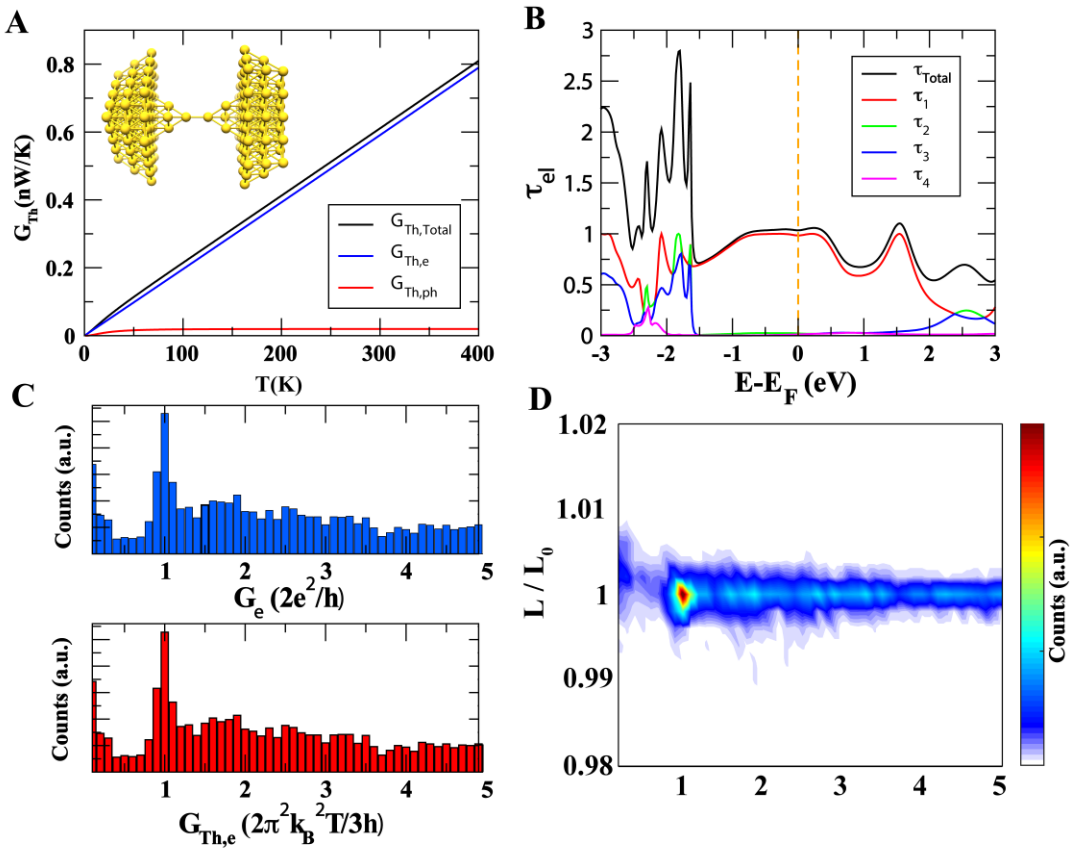

Figure 3.3: Computations of thermal conductance in Au atomic junctions.
(A) Computed thermal conductance as a function of temperature for the Au atomic junction geometry shown in the inset. The total thermal conductance (black), and the electronic contribution $G_{Th,e}$ (blue), and the phononic contribution $G_{Th,ph}$ (red) to thermal conductance are shown. Notice that $G_{Th,ph}$ is almost negligible at room temperature. (B) The total electronic transmission and the individual electronic transmission coefficients as a function of the energy (measured with respect to the Fermi energy EF) for the contact geometry in the inset of (A). The electronic transmission is dominated a single (spin-degenerate) conduction channel. (C) Electrical and electronic thermal conductance histograms obtained from 100 MD simulations of the formation of Au atomic contacts at room temperature (insets show representative electrical and thermal conductance traces obtained from these simulations). (D) Lorenz ratio (L/L0) as a function of the electrical conductance Ge of the Au contacts as obtained from the histograms in (C). Notice that the ratio is very close to one. Deviations are below 1%, which shows that the Wiedemann-Franz law is fulfilled with good accuracy, irrespective of the contact size.

Having established the origin of thermal conductance quantization and the small contribution of phonons, we focused on the analysis of $G_{Th,e}$ to systematically study the validity of the Wiedemann-Franz law for Au contacts of arbitrary size. For this purpose, we performed 100 simulations of the formation of Au junctions at 300 K while computing the electrical and thermal conductance for the transient geometries. We present histograms constructed from the

electrical and thermal conductance traces (Fig. 3.3C). The electrical conductance histogram is dominated by a peak close to $1G_0$, which is due to preferential formation of one-atom thick contacts and short atomic chains . The corresponding histogram for the thermal conductance (normalized by $2G_{0,Th}$) shows a very close correlation with the electrical one. Therefore, the Wiedemann-Franz law, $G_{Th,e} = L_0TG_e$ holds almost exactly, irrespective of the electrical conductance value (i.e. contact size) (Fig. 3.3D). Although some fine details of the experimental histograms are not reproduced, these computational results are in excellent agreement with our experiments (Fig. 3.2) and provide compelling evidence that the quantized thermal transport we observed corresponds to Au single-atom junctions and are not affected by surface contaminants, which are known to plague nano-gap thermal transport measurements[198].

The observed thermal conductance quantization in Au junctions is a direct consequence of the electronic structure of these junctions, which in turn is also responsible for the validity of the Wiedemann-Franz law. However, the opposite is not true: the validity of the Wiedemann-Franz law is a consequence of the smooth energy dependence of the electronic transmission [42, 199] but this does not imply that thermal transport is quantized in all cases. For example, our simulations of the Pt atomic junctions suggest that while the electrical and thermal conductance traces show discrete steps and are in agreement with the Wiedemann-Franz law (Fig. 3.4A), one should not expect electrical or thermal conductance quantization . Even a single-atom contact of Pt sustains multiple conduction channels with intermediate transmissions between 0 and 1 that contribute to the transport properties (Fig. 3.4B), which is clearly at variance with the Au case. These additional channels, as compared to Au, originate from the contribution of *d* orbitals in Pt . Further, our simulations show that the electrical and thermal conductance histograms for Pt are rather featureless and there are no strongly preferred conductance values at room temperature.

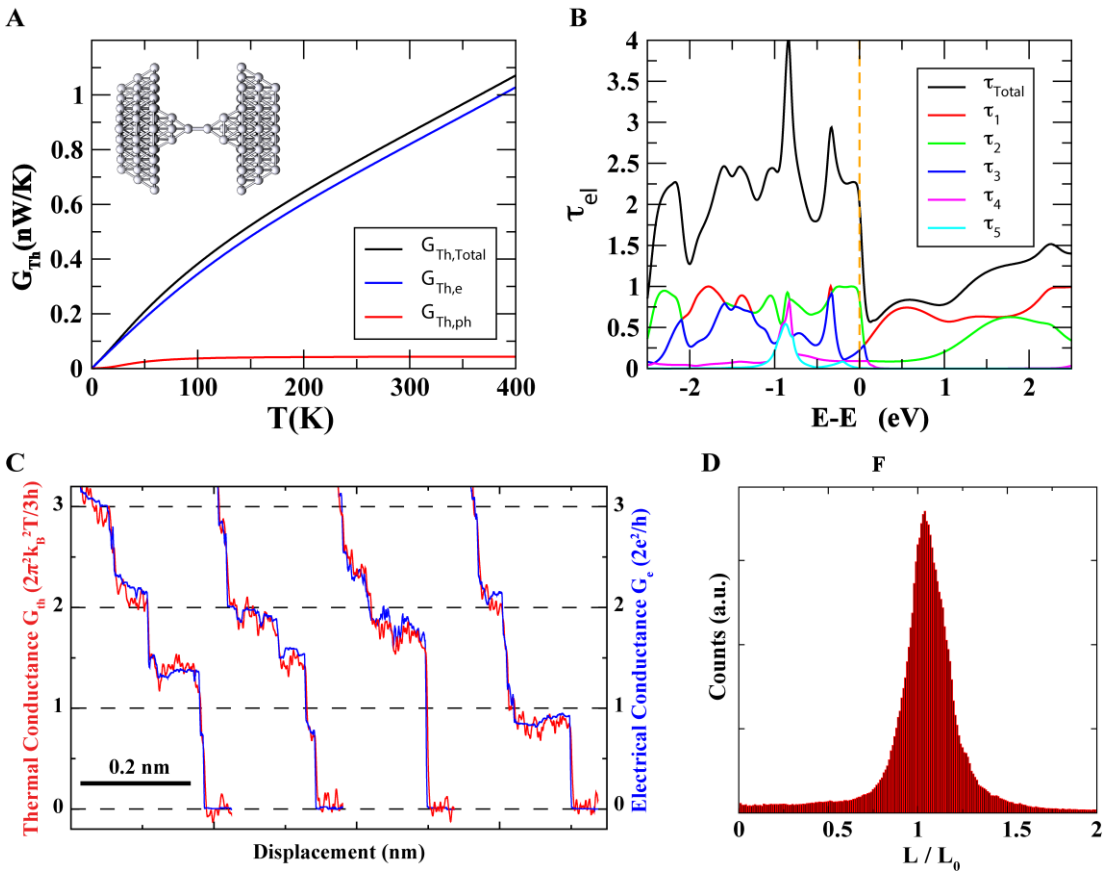

Figure 3.4: Calculated and measured transport properties of Pt atomic junctions.
(A) Representative traces of the electrical conductance (blue) and the electronic thermal conductance (red) for Pt junctions calculated by combined molecular dynamics (MD) and transport simulations. (B) The total electronic transmission and the individual electronic transmission coefficients as a function of the energy (measured with respect to the Fermi energy EF) for the contact geometry shown in the inset. The electronic transmission has significant contributions from three channels at the Fermi level. Further, the transmission varies more rapidly with energy than for Au atomic junctions. (C) Representative measured traces of electrical (blue) and thermal (red) conductances for Pt atomic junctions show discrete steps (conductance histograms do not display electrical or thermal conductance quantization). (D) Histogram similar to that shown in Fig. 3.2F but for Pt data shows that the Wiedemann-Franz law is applicable (the peak is at 1.04).

In order to unambiguously test these predictions we performed measurements using a Pt-coated scanning probe and a Pt substrate using the same methodology we used for gold atom junctions. The measured electrical and thermal conductance traces (Fig. 3.4C) show plateaus. A histogram-based analysis on 100 Pt traces (Fig. 3.4D) revealed that the Lorenz ratio is very close to 1 and therefore obeys the Wiedemann-Franz law. However, histograms of electrical and thermal conductance traces did not reveal conductance quantization, in agreement with our

computational predictions. This clearly demonstrates that thermal conductance quantization is not a universal feature of all metallic systems at room temperature.

3.4 Conclusions

Our work provides insights into thermal transport in atomic-size Au and Pt contacts and reveals conductance quantization at room temperature in Au atom junctions. We also establish the applicability of the Wiedemann-Franz law for analyzing thermal transport in metallic atomic-size contacts. The scanning calorimetric probes presented in this work will enable thermal transport studies in molecular junctions, one-dimensional chains of atoms and individual polymer chains, all of which have been studied theoretically and computationally for over half a century [17, 126] but have not been probed experimentally due to the lack of experimental tools.

3.5 Methods and Supporting Information

3.5.1 Nanofabrication process for C-SThM probes

The steps involved in the nanofabrication of the C-SThM probes are shown in Fig. 3.5. Briefly, the fabrication process proceeds as follows. The fabrication began with a silicon (Si) wafer. T-shaped beams were realized by making a trench on the Si wafer followed by wet oxidation and deposition of 600 nm of LPCVD SiNx. Subsequently, the backside of the Si wafer was patterned to facilitate KOH-based etching to release the devices in the last step of fabrication. Then a platinum (Pt) serpentine line was defined which forms a very sensitive temperature sensor. Further, 50 nm of PECVD SiNx was deposited on the serpentine line to electrically insulate it. Subsequently, the probe was released by a KOH etch. After successfully releasing the probes, each of the probes was individually flipped and aligned on a shadow mask to deposit 500 nm of the desired metal (Au or Pt) on the tip and the side walls.

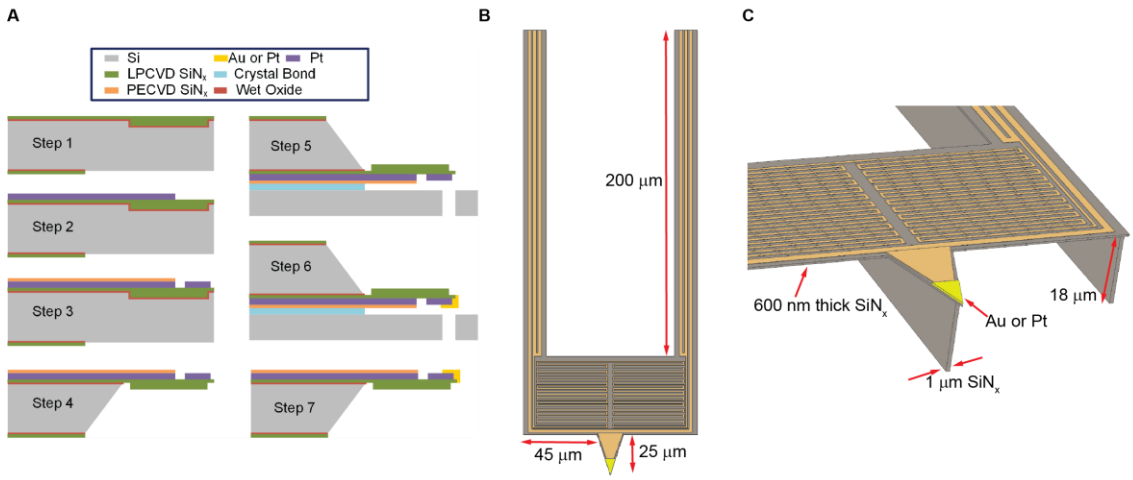

Figure 3.5: Nanofabrication steps for thermal probes
(A) (Step 1) Definition of T-shaped beams and backside patterning. (Step 2) Fabrication of the Pt serpentine resistance thermometer (30 nm thick). (Step 3) Deposition of the SiNx insulation layer, Pt tip (100 nm thick) definition and front side patterning. (Step 4) Release of the probe. (Step 5) Aligning the probe's tip with respect to a shadow mask. (Step 6) Sputtering of Au or Pt (500 nm thick) on the tip and side walls. (Step 7) Detaching the probe from the shadow mask. (B, C) Drawings show the geometry of the fabricated probe and relevant dimensions.

3.5.2 Characterization of the thermal conductance and time constant of the C-SThM probes

The thermal conductance of the probe was characterized in the following procedure. Briefly, a known amount of heat was supplied into the suspended region of the probe via the integrated Pt serpentine line and the corresponding temperature rise was measured. The relationship between the power input (Q_{in}) and the measured temperature rise (ΔT_P) is shown in Fig. 3.6A. This information can be used to readily estimate the thermal resistance of the C-SThM probe (R_P) via $R_P = \Delta T_P/Q_{in}$, which was estimated to be 1.34 MK/W.

In order to evaluate the thermal time constant of the C-SThM probe we input sinusoidal heat currents of constant amplitude and varying frequency into the suspended region of the probe. This was accomplished by supplying a sinusoidal current of amplitude (I_f = 5 μA) and at frequency *f* through the Pt heater-thermometer. This current produced sinusoidal Joule heating (Q_{2f}) in the device at frequency *2f*, with corresponding temperature fluctuations at an amplitude

ΔT_{2f}. A voltage component across the Pt heater-thermometer at 3*f*, V_{3f}, is related to these temperature fluctuations by the relationship $V_{3f} = \Delta T_{2f} \alpha I_f R/2$, where R is the nominal resistance of the Pt thermometer. Figure 3.6B presents the measured amplitude of these temperature oscillations (normalized by the amplitude at the lowest frequency). Note that the -3dB point ($f_{\text{-3dB}}$) is at ~7 Hz. Therefore, the thermal time constant (τ) of the C-SThM probe, which to an excellent approximation is a first order system, is given by $\tau = (2\pi f_{-3dB})^{-1}$ ~ 25 ms.

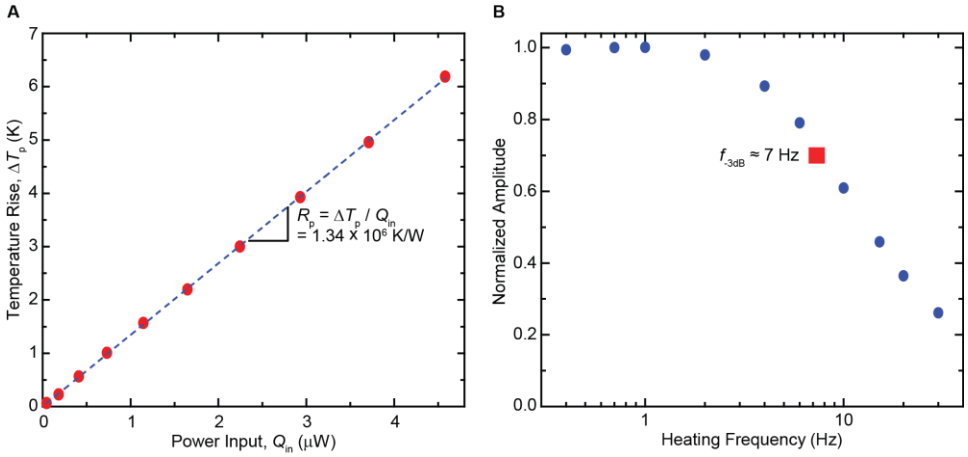

Figure 3.6: Measured thermal resistance and frequency response of the C-SThM probe.
(A) Temperature rise of the Pt resistance thermometer as a function of the heat input. (B) Normalized temperature rise of the probe as a function of frequency of heat input. The -3dB point is marked by a red square.

3.5.3 Evaluation of the stiffness of the C-SThM probes

In order to estimate the stiffness of the C-SThM probes, we performed finite element analysis (FEA) simulations using COMSOL™ (Solid Mechanics Module), which accurately predicts device stiffnesses[200]. In performing these calculations, we applied "fixed" boundary conditions to the distal ends of the beams of the C-SThM probe as shown in Fig. 3.7A. To estimate the stiffness of the probe, a 100 nN force was applied either in the normal or transverse directions at the end of the probe tip (see Figs. 3.7B, C, D). The resultant displacement field, as

computed by the FEA, enabled us to estimate the stiffness of the probe. From the computed deflections, the stiffness of the probe was estimated to be ~12,500 N/m in the normal direction and ~250 N/m and 9.1 N/m for the two transverse directions, respectively (see Figs. 3.7B, C, D). The lower stiffness in (D) arises partly due to the fact that the beam (stiffener) underneath the tip region does not fully extend to the end of the suspended region. From our experiments, we found that these stiffness values were sufficiently large to ensure stable atomic junction formation. We note that substantially lower stiffnesses can severely compromise the junction stability due to thermal fluctuation induced deflections of the probes and due to elastic instabilities. In these simulations the values of Young's modulus and Poisson's ratio of SiN_x were taken to be 290 GPa and 0.20, respectively [201].

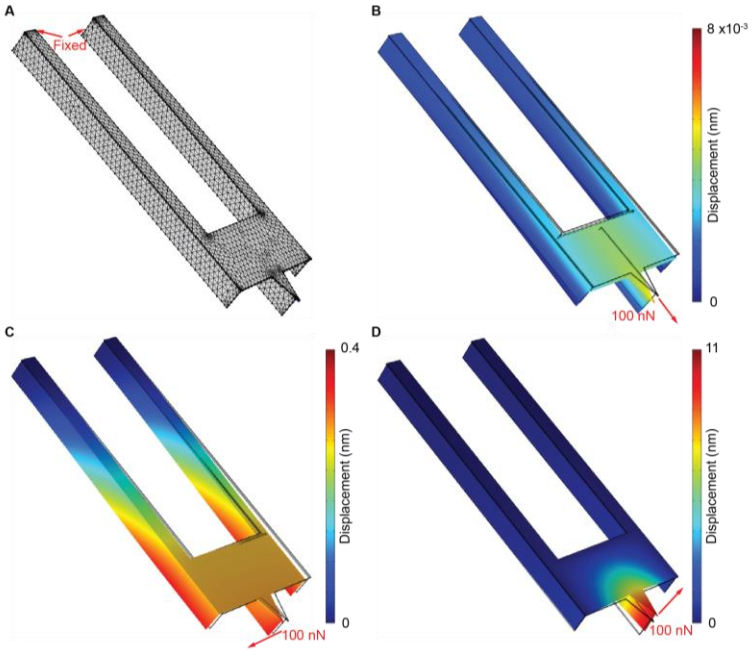

Figure 3.7: Finite element analysis of the stiffness of a C-SThM probe.
(A) The mesh used in our FEM scheme for the computation of the stiffness. A 100 nN force was applied in normal and transverse directions of the beams and the deflection for each of the cases was computed. (B–D) From the calculations the stiffness of the probe was estimated be 12500 N/m (B), 250 N/m (C) and 9.1 N/m (D), respectively.

3.5.4 Analysis of the temperature distribution and thermal expansion of the probe

We employed a COMSOL-based FEA to analyze the temperature distribution within the C-SThM probe when a heat flux is applied at the tip. The results of our calculations show that the temperature drop occurs primarily along the beams (Fig. 3.8A). This ensures that the temperature reported by the Pt resistance thermometer can be used to accurately estimate the heat flow into the probe.

A second question of importance is whether the sinusoidal electric current supplied to the Pt resistance thermometer causes deflections of the C-SThM probe due to bimaterial effects. To answer this question we first employed the FEA to compute the deflection of the C-SThM probe when a DC electric current is supplied into the Pt thermometer resulting in a 1 K temperature rise of the suspended region. Our results (Fig. 3.8B) show that the tip deflection is 1.06 nm/K. In order to estimate the perturbations due to our sinusoidal electric currents (10 μA, f = 1 kHz) supplied into the Pt line, we estimate the temperature oscillations of the probe at 2 kHz (note that Joule heating occurs at twice the excitation frequency, $2f$) by noting that our probe behaves as a first order system. Specifically, to estimate ΔT_{2f} we use the expression $\Delta T_{2f} \approx \Delta T_{DC} \times f_{-3dB}/(2f)$, where ΔT_{DC} (= 3.25 K) is the temperature increase of the suspended device when a DC current of 10 μA is supplied to the probe, $f_{\text{-3dB}}$ is the cut-off frequency of our scanning probe (~7 Hz). From this analysis we estimate the temperature rise at 2 kHz to be ~11 mK. Thus the amplitude of fluctuations of the probe due to bimaterial effects is ~12 pm. Since this amplitude is much smaller than the lengths over which the atomic junctions are stretched they do not have any adverse effects on our measurements.

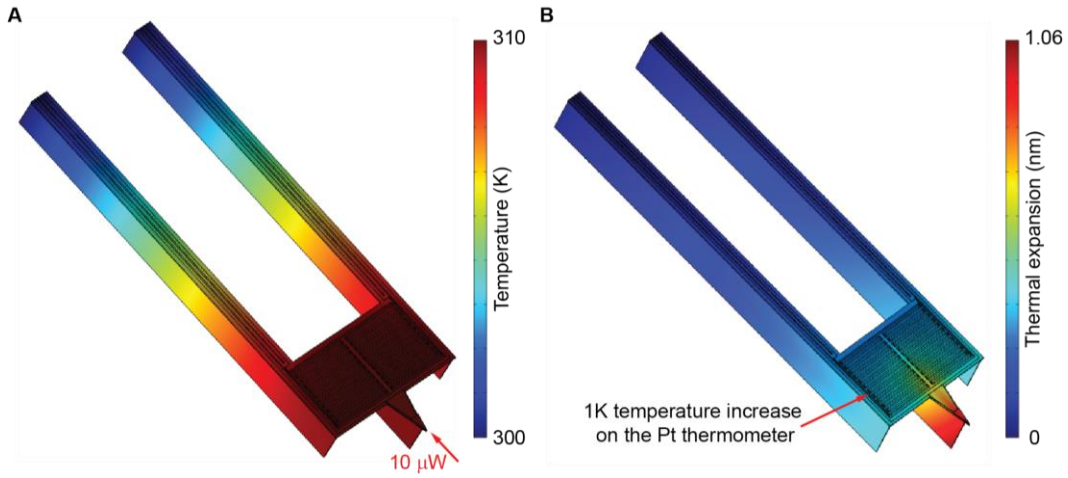

Figure 3.8: Finite element analysis of the temperature distribution and thermal expansion of the probes. (A) Computed results for the temperature increase of the probe when a power input of 10 μW was applied to the Au tip end. It can be seen that the majority of the temperature drops along the beams. (B) Deflection of the C-SThM probe, due to bimaterial effects, when the suspended region of the C-SThM probe was heated by 1 K (DC heating).

3.5.5 Electrical circuitry

As shown in Fig. 3.1A of the manuscript the electrical conductance of atomic junctions is measured by supplying a small sinusoidal electric voltage of 1 mV at 10 kHz across the scanning probe and the substrate, and monitoring the amplitude of the resultant current by using a current amplifier and a lock-in amplifier (SR 810). The small amplitude of the applied bias gives rise to very small amounts of Joule heating in single atom junctions (~25 pW), which is negligible in comparison to the 10 nW heat flow that occurs in Au single atomic junctions in response to a 20 K temperature differential (as is applied in our measurements).

The thermal conductance is measured by recording the temperature change of the scanning probe. This is accomplished by monitoring the changes in the electrical resistance of the Pt serpentine line (Pt thermometer). To achieve this goal the Pt sensor forms part of a Wheatstone bridge whose output signal was amplified by an instrumentation amplifier with a gain of 100. The amplified signal was measured using a lock-in amplifier (SR 830).

3.5.6 Noise characterization of the Pt resistance thermometer

The temperature resolution of the integrated Pt resistance thermometer was evaluated following the protocols developed by us in the past[188]. Briefly, our temperature measurement employs a modulated electrical current at 1 kHz to measure unmodulated temperature changes in a bandwidth of 10 Hz. Given this scheme, the noise in the measurement has contributions from electronics (amplifiers), Johnson noise, shot noise and ambient temperature drift. We quantified these components following the detailed protocols established in[188] and estimated the noise equivalent temperature (NET) of our current thermometry scheme to be <1 mK (~0.6 mK) RMS in a 10 Hz bandwidth.

3.5.7 Sample preparation and surface cleaning protocols

Employing proper surface cleaning protocols is essential for successfully minimizing any surface contaminations that compromise the desired thermal measurements. Towards this goal, we developed protocols for sample preparation and for cleaning the surfaces of the scanning probe and the substrate sample.

Planar Au and Pt samples were prepared by employing a template stripping approach. Briefly, a 150 nm thick layer of Au or Pt was deposited using E-beam evaporation on a pristine Si wafer. Subsequently, a low-viscosity epoxy (Epotek 377) was applied uniformly on the metal-coated Si wafer to glue a clean 7 mm × 7 mm Pyrex piece to the top surface of the wafer. The wafer was cured at ~150 °C for two hours. Right before the experiment the Pyrex substrate was peeled off to successfully expose a pristine metallic sample, which is protected from oxidation by the Si substrate. The peeling off process was conducted in a pure N_2 filled glove box, minimizing the exposure of the clean surface to the ambient environment.

Since the above-described approach cannot be applied to the metal tip of the C-SThM probe we employed the following protocol to eliminate any contamination that may have accumulated on the surfaces due to exposure to the ambient. The probes were first sonicated in acetone, IPA and then DI water for ~10 minutes in each step. Subsequently, the probe was dried in N_2 and subjected to multiple oxygen plasma cleaning cycles (300 W, 5 mins). For Pt-coated scanning probes, additional hydrogen plasma cleaning cycles (50 W, 20 mins) were applied after oxygen plasma treatment. All cleaned probes and samples were placed in a N_2 gas environment to avoid direct contact with the ambient. Successful experiments were accomplished when the apparent tunneling barrier heights [198, 202] measured in the experiments were large (>2 eV).

3.5.8 Details of histogram construction and histograms obtained from the measured electrical and thermal conductance traces for Pt atomic junctions

The 2D histogram in Fig. 3.2B was constructed by collecting the electrical conductance (G_e) and the corresponding Lorenz number (L / L_0) of the four measured electrical and thermal conductance traces shown in Fig. 3.2A and counting the number of data falling into the joint bins of $[(G_e)_i, (L / L_0)_j]$, where $i, j = 1, 2, \ldots, N$. In constructing our histograms N was chosen to be sufficiently large (>100, as large as 1000 in some cases) to give results that were invariant with further increasing the value of N. The same procedure was applied to obtain the joint plot of electrical and thermal conductances in Fig. 3.2E, where we used ~2000 traces of concurrently measured G_e and G_{Th}, without any data selection. These measured traces were also used to obtain 1D histograms of electrical conductance (Fig. 3.2C) and thermal conductance (Fig. 3.2D) and the corresponding Lorenz number (Fig. 3.2F). Histograms in Figs. 3.3C and 3.3D were constructed using the same approach (with a $N = 50$) as outlined for the data analysis in Fig. 3.2 but by using

100 computed electrical and thermal conductance traces. We note that these results are independent of probes and could be successfully repeated with multiple probes and samples.

The histograms obtained from the measured electrical and thermal conductance traces for Pt junction are shown in Fig. 3.9. As explained in the manuscript, the histograms for Pt atomic junction, in contrast to histograms for Au atomic junctions, do not show any clear peaks at integral multiples of G_0, $G_{0,Th}$, suggesting that there is no observable thermal conductance quantization for Pt junctions at room temperature.

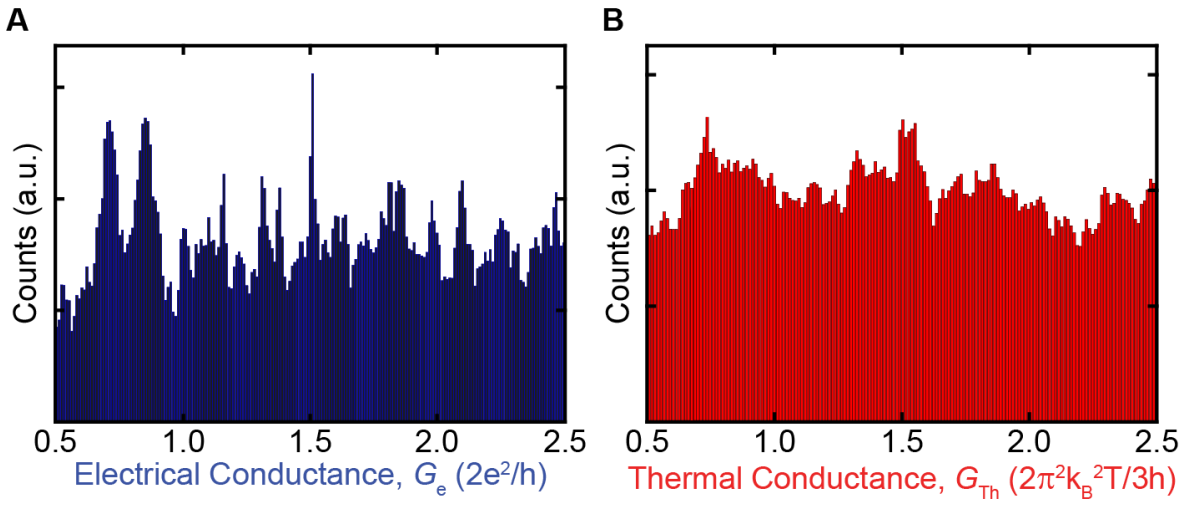

Figure 3.9: Histograms for Pt atomic junctions.
(A, B) Electrical and thermal conductance histograms for Pt atomic junctions (obtained from experimental data). The histograms are relatively featureless and do not display any distinct conductance quantization.

Chapter 4: Heat Transport in Single Molecule Junctions

4.1 Abstract

Single molecule junctions and chains are paradigmatic platforms for probing the novel charge and energy transport phenomena that are at the fundamental molecular limit. Recent works have successfully probed a variety of transport properties at the single molecule level such as electrical conduction[3, 62], light emission[203], thermoelectricity[61, 204], quantum interference[205, 206], and Joule heating[173]. Although central to our understanding of energy transport and conversion at the nanoscale, heat conduction in single molecule junctions has so far eluded direct detection due to experimental challenges. Moreover, theoretical modeling[114, 115, 116, 121] of heat transport in molecular junctions based on various frameworks has yield inconclusive predictions. Here, by employing custom developed calorimetric scanning thermal microscopy probes with picowatt resolution[174], we quantitatively measure the thermal conductance of single molecule junctions and identify the dependence of thermal transport on molecular length. Specifically, our experimental studies, performed in prototypical alkanedithiol (Au-SH-$(CH_2)_n$-SH-Au, n =2, 4, 6, 8, 10) junctions, reveal that thermal transport in single molecule junctions is ballistic, nearly independent on the molecular length. Furthermore, our *ab initio* simulations explain the experimental observations within Landauer theory of quantum thermal transport and demonstrate the dominant role of vibrational energy (phonon) transport in single molecule junctions. The experimental technique and methods presented in this work set the benchmark for systematic

studies of single molecule thermal transport and energy conversion, which is crucial to address numerous fundamental questions that have remained experimentally inaccessible.

4.2 Introduction

Study of heat transport in molecules is of great fundamental interest and critical importance for the development of a variety of technologies including molecular electronics[5], thermally conductive polymers[207], and energy-conversion devices[1]. Over the past decade, a series of experimental advances have enabled heat transport measurements in devices and materials consisting of ensembles of molecules such as self-assembled monolayer of molecular junctions[43] and polymer nanofibers[151], and probed critical aspects of heat conduction relevant to the intrinsic properties of the constituent molecules. However, these experimental investigations, owing to the ensemble nature and complex interactions of the studied molecules, are inadequate for addressing many fundamental issues of molecular-scale heat transport and reported contradictory observations as of how phonons transport heat at the single molecule limit and how heat transport depends on the size of the molecular materials. Furthermore, recent computational efforts[114, 115], mainly focusing on modeling heat transport in alkane-based single molecule junctions, have suggested a non-monotonic behavior of heat conduction as the molecular chain length increases. Yet other theoretical attempts[121] have demonstrated a moderate to nearly absent length dependence in the same molecular junctions. In addition, the predicted value of molecular thermal conductance differs quantitatively by over two orders of magnitude. These discrepancies in both experimental and theoretical studies call for a benchmark examination of heat transport at the single molecule level.

4.3 Experimental Results and Analysis

Experimentally probing heat transport in single molecule junctions is challenging due to the technical difficulties in reproducibly creating and accessing molecular scale junctions while simultaneously measuring the picowatt (pW) level heat currents involved in the thermal transport processes. Here we report on the measurement of thermal conductance of single molecule junctions by overcoming these experimental challenges. Key to performing thermal transport studies in single molecule junctions in this work was to leverage custom developed scanning probes with excellent mechanical stability and ultrahigh thermal sensitivity, called calorimetric scanning thermal microscopy (C-SThM)[174]. Specifically, the nanofabricated C-SThM probe (Fig. 4.1) features a suspended micro-island supported by two thin, long T-shaped silicon nitride (SiN_x) beams with both very high stiffness (>10^4 N/m in the normal direction) and thermal resistance ($R_P \approx 1.3\times 10^6$ K/W). A platinum (Pt) serpentine shaped resistor is embedded into the micro-island and works as a highly sensitive resistance thermometer with a temperature resolution of ~0.1 mK with ~0.2 Hz bandwidth. These characteristics enabled the detection of heat current flowing in or out of the scanning probe with ~100-pW resolution, critical to resolve the minute thermal energy flowing through a single molecule junction.

The experimental setup and strategy for quantifying thermal conductance of single molecule junctions is depicted in Fig. 1a. The C-SThM probe is heated up to $T_P = 315\ K$ by supplying a fixed d.c. electric current (30 μA) into the Pt serpentine resistor, while the Au sample substrate is connected to a thermal reservoir maintained at room temperature $T_S = 295\ K$. The planar surface of the Au substrate is coated with a self-assembled monolayer of molecules to facilitate the formation of single molecule junctions between the Au coated tip of the scanning probe and the substrate. In this work, we choose the simple and prototypical thiol-terminated

alkane molecules to perform the experiments of heat transport in single molecule junctions.

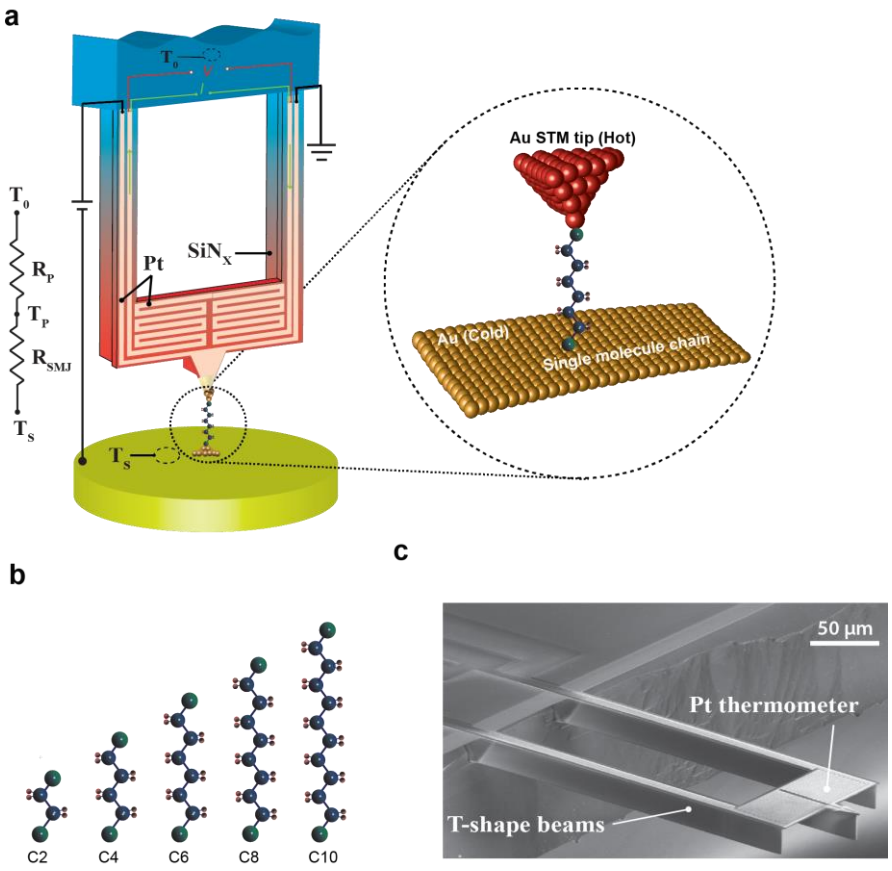

Figure 4.1: Experimental setup and strategy for quantifying heat transport in single molecule junctions.
a, Schematic of the calorimetric scanning thermal microscopy (C-SThM) experimental setup. A single molecule junction is trapped between the Au coated tip of the C-SThM probe and a Au substrate. The electrical conductance of the molecular junction is measured by applying a small d.c. voltage bias and recording the resultant electric current. A temperature difference is maintained across the molecular junction by supplying a d.c. electric current into the embedded Pt resistor to heat up the scanning probe by, while leaving the Au substrate connected to a thermal reservoir at room temperature. The electrical resistance of the Pt resistance-thermometer is monitored by measuring the voltage output in the presence of the input d.c. current. Thermal conductance of single molecule junctions is quantified by recording the temperature change of the Pt thermometer during the breakdown process of the molecular junctions. A thermal resistance network describes the thermal resistances of the molecular junction $G_{Th}=1/R_{SMJ}$ and the scanning probe (R_P). T_P and T_S indicate the temperatures of the probe and thermal reservoir (substrate), respectively. b, Chemical structures of the studied molecules (alkanedithiol) in this experiment. C_n (n = 2, 4, 6, 8, 10) denotes the number of Carbon atoms in the molecules. c, Scanning electron microscope image of the custom-fabricated C-SThM probes, featuring two long T-shaped SiN_x beams and a suspended micro-island patterned with serpentine Pt thermometer.

We first created a series of molecular junctions by driving the scanning probe at a constant speed via piezoelectric actuation towards the Au substrate until making contact,

signaled by a sufficiently large electrical conductance recorded by applying a voltage bias between the Au tip and the substrate. Subsequently, the probe is withdrawn slowly from the substrate at a speed of 0.05 nm/s. During this process, the initially created multiple molecular junctions within the space between the scanning probe and the substrate will break away consecutively until a single molecule junction is formed and broken upon further mechanical or thermal activation. We monitor the formation of the single molecule junctions while simultaneously performing thermal and electrical transport measurements. If a single molecule of alkanedithiol is trapped and then broken-down, we should expect to observe a rapid drop in both electric (measured current) and thermal (measured temperature) signals. According to the resistance network, the thermal conductance of molecular junctions (G_{Th}) can be obtained by $G_{Th} = \Delta T_P/[R_P(T_P - T_S)]$, where ΔT_P is the temperature change of the scanning probe which can be quantified by measuring the resistance change of the Pt thermometer in the presence of the supplied d.c. electric current into the resistor.

We begin our experimental studies by first trapping molecules of 1,6-hexanedithiol (HDT) between the Au coated tip of the C-SThM probe and the Au substrate, and measuring the electrical conductance of single molecule junctions. Representative electrical conductance traces obtained when the tip is repeatedly displaced away from the substrate is shown in Fig. 4.2a, with the histogram constructed from ~500 measured conductance traces. The histogram features a pronounced peak at $\sim 6 \times 10^{-4} G_0$ (electrical conductance quantum, $G_0 = 2e^2/h \approx 77.5\,\mu S$), indicating the most probable low-bias conductance of single Au-HDT-Au junctions and in good agreement with previous work[208]. We then proceed to probe thermal conductance of single molecule junctions by forming stable Au-HDT-Au junctions with an electrical conductance that is close to (within 20%) the most probable low-bias value and recording the change of thermal

conductance of the junction when it breaks spontaneously. Typical traces of the measured electrical and thermal conductance are shown in Fig. 4.2b. As expected, when the molecular junction breaks down, electrical conductance undergoes dramatic drop within a few milliseconds (the time constant of the electrical measurements). However, the anticipated change in thermal conductance is not observable due to the considerable noise in the thermal signal (~100pW peak-to-peak).

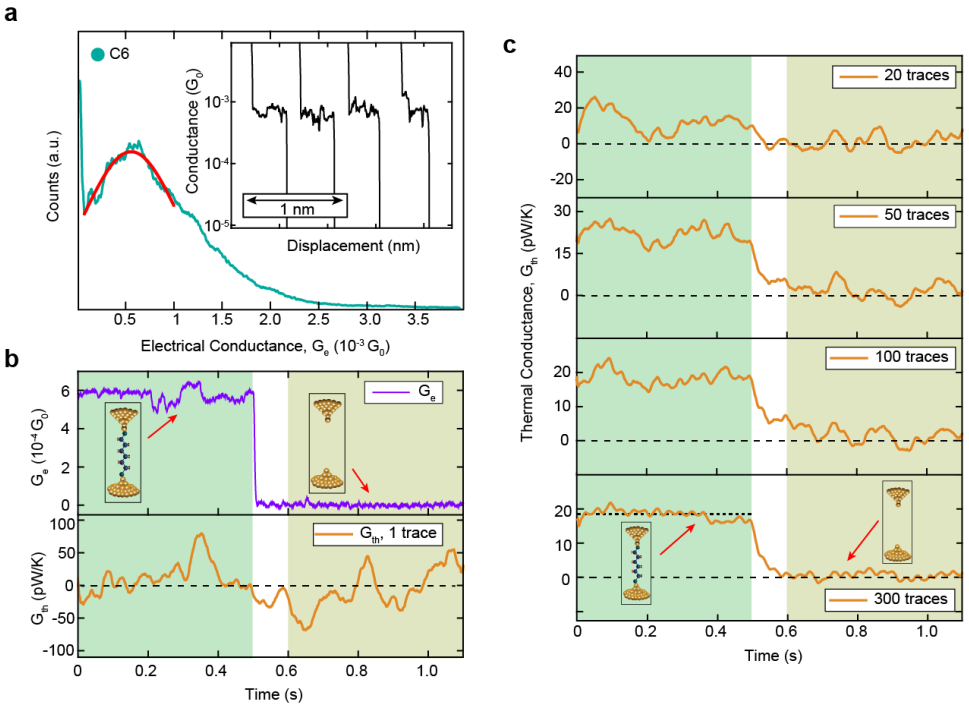

Figure 4.2: Measurement of electrical and thermal conductance of single Au-Hexanedithiol (HDT)-Au junctions.
a, Representative traces of electrical conductance (inset) of HDT junctions along with a histogram obtained from ~500 traces (main panel). A Gaussian fit to the histogram peak is represented by the solid red line. a.u., arbitrary units. b, Experimental protocol for measuring thermal conductance of a single HDT junction. The electrical conductance trace (Upper panel) shows the breakdown of the molecular junction, indicated by the sudden drop of the measured conductance value. The thermal conductance of the single junction (Lower panel) is not resolvable in the simultaneously obtained thermal conductance traces due to the large noise buried in the signal. c, Improved thermal resolution is obtained by aligning and averaging multiple thermal conductance traces using electrical signal as references. Clear drop of thermal conductance signal is seen after averaging ~100 traces.

To resolve the small thermal signal, we applied an averaging scheme that improves the signal-to-noise ratio of the thermal measurements. Briefly, we obtained many (from ~50 to 300)

electrical conductance traces and marked the time point when the junction breaks (at $t = 0.5\ s$ in Fig. 4. 2b). Using the electrical signal as a reference, which marks the breakdown of the molecular junction, the simultaneously measured thermal signal are aligned and averaged, and thermal conductance of the junction (G_{Th}) is determined. The results of G_{Th} after averaging of 20, 50, 300 traces are shown in Fig. 4. 2c. It is clear that the averaging scheme reduces the noise level and a corresponding drop of thermal signal as the molecular junction breaks is now resolved. In particularly, for a single Au-HDT-Au junction, the thermal conductance is found to be ~18 pW/K. Note that in contrast to the rapid transition of electrical signal, the rolling-off of thermal conductance is much slower, limited by the thermal time constant of the scanning probe (~25 ms).

The capability of resolving thermal conductance at the single molecule scale offers a unique opportunity for us to address important fundamental questions with regard to recent debates in both theoretical and experimental studies about how thermal transport in single molecule junctions depends on the molecular length. To answer this question unambiguously, we performed thermal transport measurements with a series of alkanedithiol molecules with different CH_2 units (from 2 to 10), following the procedure we have developed and described above. Figure 3a shows the measured electrical conductance histograms for all the studied molecules and the Gaussian-fitted peak values are summarized in Fig. 4.3c. It can be seen that electrical conductance (G_e) of single alkanedithiol junctions exhibits exponential decay as the molecular length increases, indicating the tunneling-mechanism dominated electron transport in molecular junctions. The tunneling decay constant (β) can be estimated to be 0.92 ± 0.05, agrees well with past work[62]. In strong contrast to the measured length-dependent electrical conductance, thermal conductance of single alkanedithiol junctions (as shown in Fig. 3b and 3c)

demonstrated a nearly length-independent behavior, suggesting the thermal transport in single molecule junctions is ballistic. We have also performed a control experiment at another temperature difference ($\Delta T = 40K$) and verified the robustness of our observation. By fitting the measured thermal conductance at different molecular length, we found that for various single alkanedithiol junctions, the value of the thermal conductance is within a narrow range, centered around 20 pW/K.

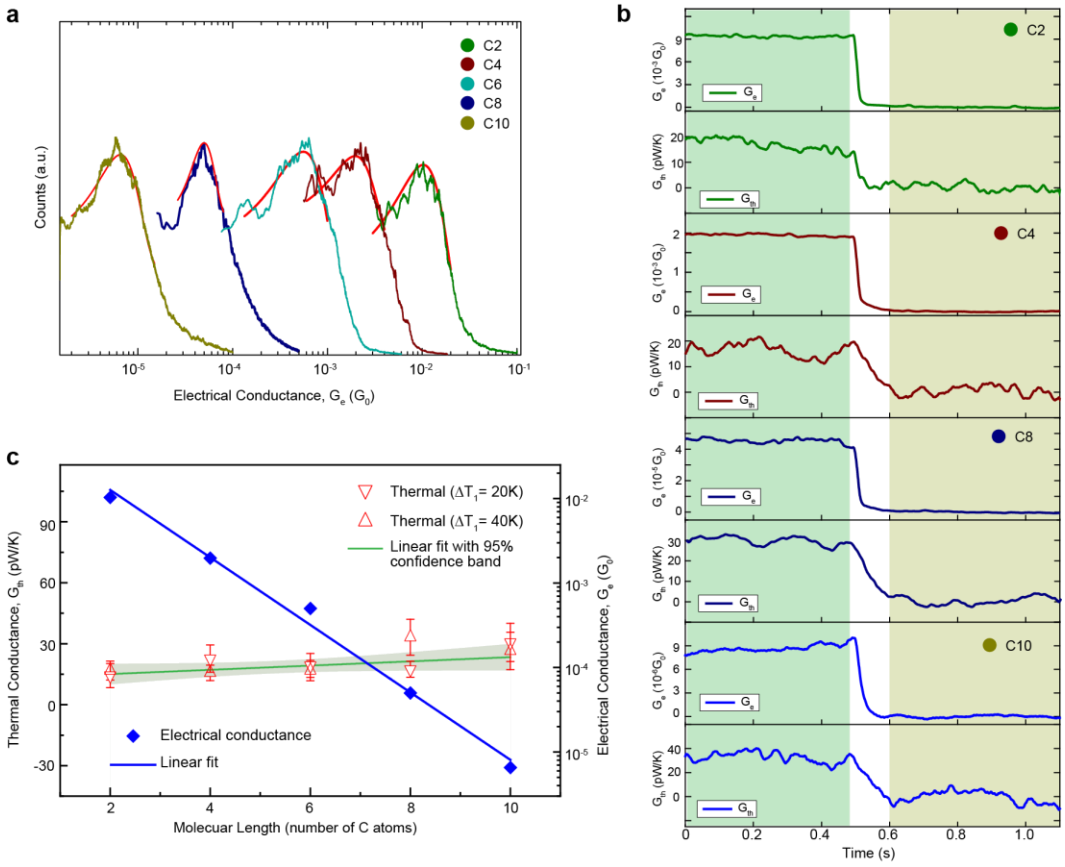

Figure 4.3: Length dependent electrical and thermal transport in single Au-Alkanedithiol-Au junctions.
a, Measured electrical conductance histograms for different alkanedithiol junctions (C2 to C10). Red lines represent the Gaussian fit of the histogram peaks. b, Measured electrical and thermal conductances of single alkanedithiol junctions by averaging ~100 traces, applying the experimental protocol described in Fig. 2b. c, Measured electrical (blue square) and thermal conductance (red triangle) as a function of the molecular length, indicated by the number of Carbon atoms in the alkanedithiol junction. The solid blue line indicates the fitted curve of electrical conductance (on log scale). The measured thermal conductance is fitted by a linear curve (green line), with the light green shaded region representing the 95% confidence band. Thermal conductance data from two difference temperature differences (ΔT = 20 K and 40 K) are shown. Error bars represent one standard deviation of the data.

4.4 Conclusion

In conclusion, we have experimentally measured the thermal transport in single molecule junctions and quantified the dependence of thermal conductance at the single molecule level on the molecular length. Our experimental results have demonstrated the ballistic transport of vibrational energy (phonons) in single molecule junctions, in contrast to the tunnelling mechanism based electron transport in the same junctions. Furthermore, based on this benchmark study, the presented platform should stimulate further systematic exploration of thermal transport and energy conversion in various atomic and molecular scale materials and systems.

Chapter 5: Peltier Cooling in Molecular Junctions

Reproduced with permission from *Nature Nanotechnology*. See Ref.[206]

Longji Cui, Ruijiao Miao, Kun Wang, Dakotah Thompson, Linda A. Zotti, Juan Carlos Cuevas, Edgar Meyhofer and Pramod Reddy

5.1 Abstract

The study of thermoelectricity in molecular junctions (MJs) is of fundamental interest for the development of a variety of technologies including cooling (refrigeration) and heat-to-electricity conversion[17, 18, 19, 45]. Recent experimental progress in probing the thermopower (Seebeck effect) of MJs[61, 65, 66, 80, 90] has enabled studies of the relationship between thermoelectricity and molecular structure[1, 5]. However, observation of Peltier cooling in MJs—a critical step for establishing molecular-based refrigeration—has remained inaccessible. Here, we report the experimental observations of Peltier cooling in MJs. By integrating conducting probe atomic force microscopy[63, 87] with custom-fabricated picowatt-resolution calorimetric microdevices, we created an experimental platform that enables the unified characterization of electrical, thermoelectric, and energy dissipation characteristics of MJs. Using this platform we studied prototypical molecules (Au-Biphenyl-4,4'-dithiol-Au, Au-Terphenyl-4,4''-dithiol-Au, and Au-4,4'-Bipyridine-Au) and revealed the relationship between heating or cooling and charge transmission characteristics. Our experimental conclusions are supported by self-energy

corrected density functional theory calculations. We expect these advances to stimulate studies of both thermal and thermoelectric transport in MJs where the possibility of extraordinarily efficient energy conversion has been theoretically predicted[18, 19, 45, 115].

5.2 Introduction

When an electrical current flows across an isothermal junction of two materials net refrigeration is accomplished when Peltier cooling is larger in magnitude than Joule heating[209, 210]. Experimentally probing Peltier cooling and Joule heating in current-carrying MJs is crucial for understanding electron transport, electron-phonon interactions, and energy dissipation mechanisms at the atomic and molecular scales. Previous experimental studies[169, 170, 171] have explored local ionic and electronic heating in MJs and probed the non-equilibrium temperature increase due to electron-phonon and electron-electron interactions in the junctions. More recently, experimental advancements have enabled the measurement of Joule heating in the electrodes of MJs[39, 173]. In spite of interesting theoretical predictions and practical significance[17, 45, 159] experimental observations of molecular-scale refrigeration have not been possible due to technical challenges in detecting picowatt level cooling.

5.3 Experimental Results and Analysis

We developed an experimental platform that is capable of creating and stably maintaining MJs while allowing simultaneous measurements of the electrical conductance, Seebeck coefficient, as well as the heating or cooling power deposited in the electrodes of the MJs. Specifically, we developed custom-fabricated calorimetric microdevices (Fig. 5.1a and 5.1b), which integrate highly sensitive Pt thermometers with a temperature resolution (ΔT_{min}) of <0.1 mK. The microdevice is suspended via four long, doubly clamped silicon nitride (SiN_x) beams to achieve both high thermal resistance (R_S ~ 3.3MK/W) and stiffness (~3.8 N/m). These

characteristics enable detection of heating or cooling power with ~30 pW resolution. Moreover, the planar surface of the microdevice is coated with an electrically isolated Au layer, on top of which a self-assembled monolayer (SAM) is created to facilitate the formation of MJs.

Our strategy for quantifying the Peltier-effect based cooling of MJs, at room temperature (298 K), is depicted in Fig. 5.1a. A contact-mode atomic force microscope, equipped with a sharp Au-coated cantilevered probe (tip radius ~100 nm and stiffness ~0.1 N/m), is employed to make a "soft" contact with the monolayer of molecules on the Au-coated microdevice and the contact force is maintained at ~1 nN by employing feedback control. As established in past work[63, 87, 211, 212], this nanoscopic contact between an AFM tip and a SAM contains approximately 100 metal-molecule-metal junctions. To perform the actual experiment, we applied a voltage bias (V_P) and recorded the resultant electric current (I) flowing through the molecules from which we obtained the electrical conductance (and the I-V characteristics) of the MJs. Current flow across the MJs results in heat dissipation and cooling due to Joule heating and Peltier effects, which in turn give rise to a temperature change of the calorimetric microdevice, that can be quantified by measuring the resistance of the Pt thermometer integrated into the device. To monitor the temperature change, we supplied a fixed electric current (I_{in} = 20 μA) to the Pt thermometer while continuously monitoring the voltage drop (V_{Cal}) across the resistor. The total cooling or heating power (Q_{Cal}) in the calorimeter can be directly determined from ΔT by $Q_{Cal} = \Delta T / R_S$, where R_S is the thermal resistance of the microdevice.

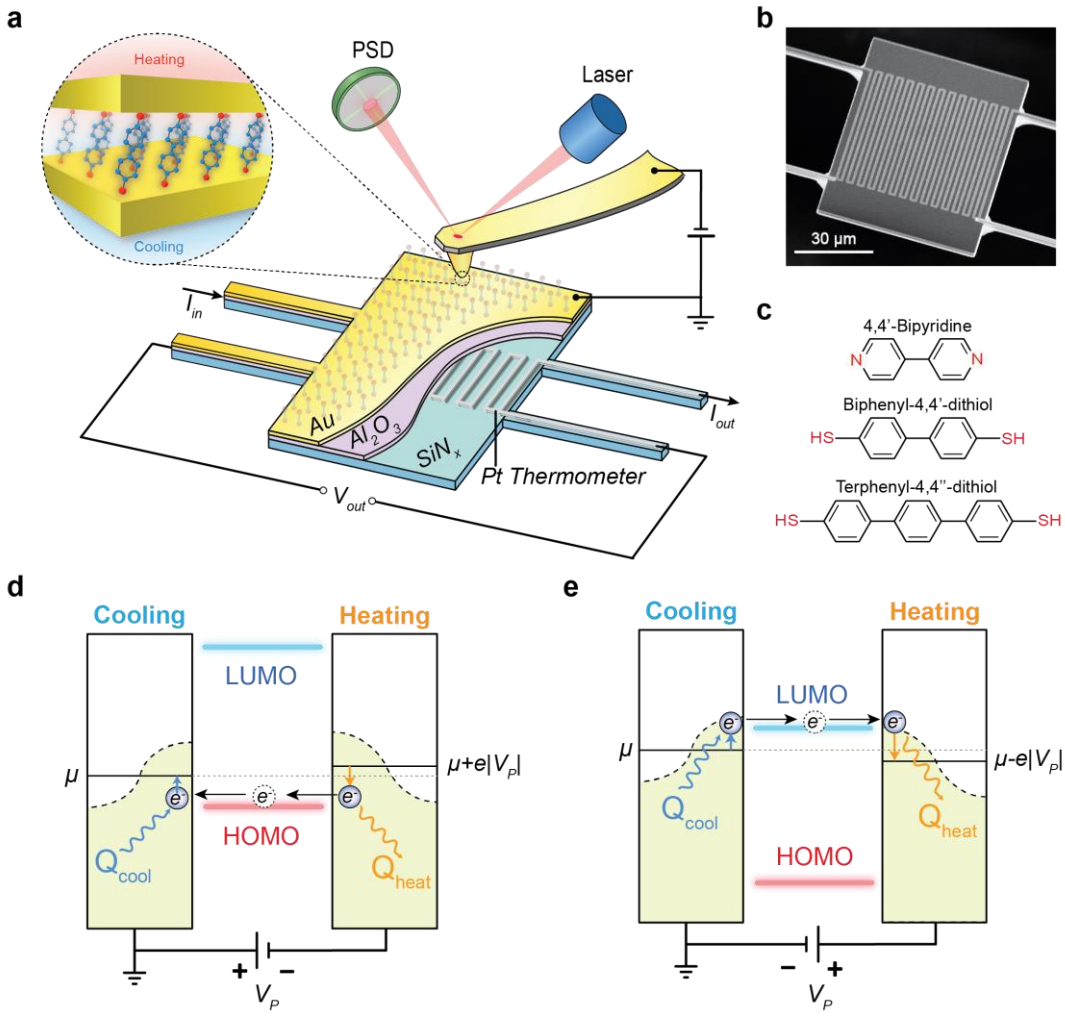

Figure 5.1: Probing cooling in molecular junctions.
a, Schematic of the experimental platform where a Au-coated AFM tip is in gentle contact with a self-assembled monolayer of molecular junctions formed on a Au-coated calorimetric microdevice. The electrical conductance of the molecular junctions is measured by supplying a small voltage bias (V_P) and recording the resultant current. The temperature change of the microdevice is induced by the heating or cooling effect in the current-carrying molecular junctions. The resistance of the Pt thermometer is continuously monitored by applying an electric current (I_{in}) into the resistor and measuring the voltage output (V_{cal}). **b**, SEM image of the custom-fabricated microdevice. **c**, Chemical structures of the molecules studied in this experiment. **d**, Schematic description of the origin of the Peltier effect in a molecular junction where transport is dominated by the Highest Occupied Molecular Orbital (HOMO). The transmission function is depicted as a Lorentzian around the HOMO and LUMO (Lowest Unoccupied Molecular Orbital) levels. μ_{Cal}, Q_{heat} and Q_{cool} denote chemical potential, heating and cooling power, respectively. **e**, same as **d**, but for LUMO-dominated case.

One may ask whether it is reasonable to expect cooling in the electrodes of MJs and under which conditions. Within Landauer theory, one can show that when a voltage bias V_P is

applied to the probe relative to the grounded calorimeter electrode, the power input into the calorimeter (Q_{Cal}) is[24,]:

$$Q_{Cal}(V_P) = \frac{2}{h}\int_{-\infty}^{+\infty}(\mu_{Cal} - E)(f_{Cal} - f_P)\tau(E, V_P)dE = GTSV_P + \frac{1}{2}GV_P^2 + O(V_P^3) \quad (1)$$

where μ_{Cal} is the chemical potential of the calorimeter electrode, f_P and f_{Cal} are the Fermi-Dirac distributions of the probe and calorimeter electrodes, respectively, $\tau(E,V_P)$ is the energy- (E) and voltage bias- (V_P) dependent transmission of the junction, T is absolute temperature, G, S are the low-bias electrical conductance and the Seebeck coefficient of the MJs, respectively and $O(V_P^3)$ represents the higher order terms. Note that G and S are related to $\tau(E,V_P)$. Thus, for small biases, when $|V_P| < 2|ST|$ and the first order term ($GTSV_P$) dominates, cooling is expected when SV_P, the product of the Seebeck coefficient and the applied bias, is negative. The physical picture behind the expected cooling mechanism is shown in the schematics in Fig. 5.1d and 5.1e and is discussed below.

We first investigated cooling in Au-Biphenyl-4,4'-dithiol (BPDT)-Au junctions. Towards this goal, we applied a periodic, three-level voltage sequence, $+V_P$ from (t = 0 to 1.66 s), $-V_P$ (1.66 s to 3.33 s) and 0 Volts (3.33 s to 5 s), across Au-BPDT-Au junctions, and simultaneously measured both the current flow through the junctions and Q_{Cal} (note that the calorimeter electrode is always grounded in these experiments). The time period of each of the voltage pulses (1.66 s) is chosen to be significantly larger than the thermal time constant (~40 ms) of the microdevice so that there is sufficient time for steady state conditions to be established in the calorimeter. Representative traces of the recorded electrical current (I) and heating or cooling power (Q_{Cal}), corresponding to one period of the three-level voltage sequence ($+V_P$, $-V_P$, and 0, where V_P was

chosen to be 3 mV) are shown in Fig. 5.2a. It can be clearly seen that when the voltage is changed from $+V_P$, to $-V_P$, the current direction switches sign as expected. However, the expected heating or cooling of the calorimeter (represented by a temperature change of the calorimeter) remains unresolvable due to the considerable noise in the signal. To resolve the desired signal, we employed an averaging scheme that significantly improves the thermal resolution and hence the calorimetric resolution. Briefly, in this approach the thermal signals from many (500 to 2000) equivalent phases of three-level voltage sequence ($+V_P$, $-V_P$, and 0) are aligned and averaged, and Q_{Cal} is determined. Figure 5.2a depicts the results obtained after averaging 10, 100, 1500 period traces, clearly demonstrating that such averaging significantly reduces noise to a level where heating and cooling can be resolved. Specifically, for Au-BPDT-Au junctions we find a net cooling power ~300 pW when a negative bias of -3 mV is applied. The corresponding heating power when reversing the bias polarity is ~600 pW.

Figure 5.2b presents the time-averaged thermal signal for varying V_P from 1 mV and 9 mV for the same Au-BPDT-Au MJs. It can be seen that under positive biases Q_{Cal} is always positive. In contrast, net cooling ($Q_{Cal} < 0$) is observed in a narrow range of negative biases, $V_P \in [-8\,mV, 0\,mV]$. We plot the measured Q_{Cal} as a function of the voltage bias applied to the probe (V_P) in Fig. 5.2c. The measured power dissipation is roughly parabolic as expected from Eq. 1. In order to obtain a quantitative comparison with the predictions of Eq. 1 we independently measured the electrical conductance and the Seebeck coefficient of MJs. These measurements are accomplished with the same experimental platform by directly recording the *I-V* characteristics and *S.* From these measurements (Fig. 5.2d) we determined that the low-bias conductance is ~37 μS (note that this relatively large conductance is due to the fact that we trapped multiple molecules in the MJ) and the Seebeck coefficient is $+13.0 \pm 0.6$ μV/K

(indicating that transport is dominated by the highest occupied molecular orbital (HOMO)), in good agreement with past work[87] for Au-BPDT-Au MJs. By inputting these independently measured transport parameters into Eq. 1 (neglecting higher order $O(V_P^3)$ terms) we obtained the solid line show in Fig. 5.2c. The resulting agreement between the calculated thermoelectric cooling of Au-BPDT-Au junctions and the experimental values confirmed the applicability of the Landauer approach for modelling cooling.

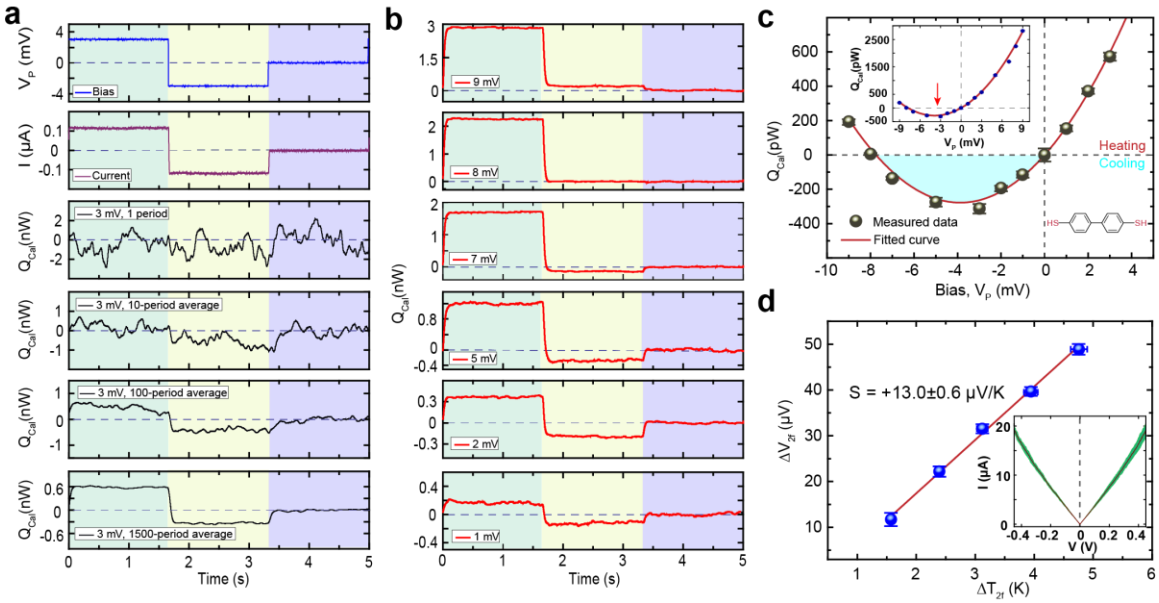

Figure 5.2: Observation of Peltier cooling in Au-BPDT-Au junctions.
a, Experimental protocol to quantify the heating and cooling power in molecular junctions. A periodic three-level voltage (blue line) is supplied into the junctions, while electrical current (purple line) and thermal signal (black lines) are simultaneously recorded. Improved thermal resolution is obtained by averaging the thermal signal over a large number of periods to reduce noise level. b, Time-averaged heating and cooling signal traces (red lines) under different voltage bias. c, Measured voltage-dependent thermal power for BPDT junctions. The solid red line indicates the fitted curve using Eq. 1 and the measured Seebeck coefficient and electrical conductance. Inset shows the measured data and the fitted curve for voltage bias from -9 mV to +9 mV. The red arrow points to the voltage that leads to the maximum cooling effect. The shaded blue region indicates the voltage region where net cooling (refrigeration) is observed. d, Measured Seebeck coefficient (S) of BPDT junctions. The red solid line is the best linear fit to the measured data, with the slope indicating the Seebeck coefficient. Inset shows the I-V characteristics of the junctions obtained by averaging 10 individual I-V curves. The green shaded region represents the standard deviation.

The physical processes that result in MJ-based cooling can be understood by considering the schematic of a HOMO-junction shown in Fig. 5.1d. The left electrode is grounded and

represents the electrode integrated into the calorimeter while the right electrode signifies the probe. When the probe is negatively biased as shown, electrons are injected into the probe electrode at an energy of $\mu_{Cal} + e|V_P|$ and leave the calorimeter electrode at an energy μ_{Cal}. Under these conditions charge transfer occurs not only at energies between $\mu_{Cal} + e|V_P|$and μ_{Cal} but also at energies within a few $k_B T$ (k_B is the Boltzmann constant) of the chemical potentials due to the thermal broadening of the Fermi-Dirac functions. Charge transfer at energies between the chemical potentials leads to Joule heating in the calorimeter. However, charge transfer through the junction at energies below the chemical potential of the calorimeter electrode leads to cooling in the calorimeter, while charge transfer at energies above the chemical potential of the probe leads to heating. Thus, in HOMO dominated junctions, when the probe is negatively biased and the voltage magnitude is appropriately chosen, net cooling (i.e. Peltier cooling dominating over Joule heating) occurs in the calorimeter as the transmission probabilities (see Fig. 5.1d) are larger at μ_{Cal} than at $\mu_{Cal} + e|V_P|$. The situation is reversed when the probe is positively biased resulting in only net heating in the calorimeter for HOMO dominated junctions. Similar arguments can be presented to understand cooling in LUMO dominated junctions (Fig. 5.1e).

Corresponding measurements are also performed on Au-Terphenyl-4,4’’-dithiol (TPDT)-Au junctions and Au-Au nanocontacts. The measured thermal power, *I-V* characteristics, and Seebeck coefficient are summarized in Fig. 5.3. In contrast to the BPDT case, TPDT MJs exhibit significantly smaller cooling due to their low electrical conductance, in spite of a slightly higher Seebeck coefficient of $+15.7 \pm 1.1$ μV/K. In Au-Au nanocontacts without molecules between the Au electrodes, there was no detectable cooling effect (Fig. 5.3c) due to the extremely small Seebeck coefficient — a result in excellent agreement with the

prediction of Eq. 1. This control experiment confirms that the molecules play a critical role in the observed cooling.

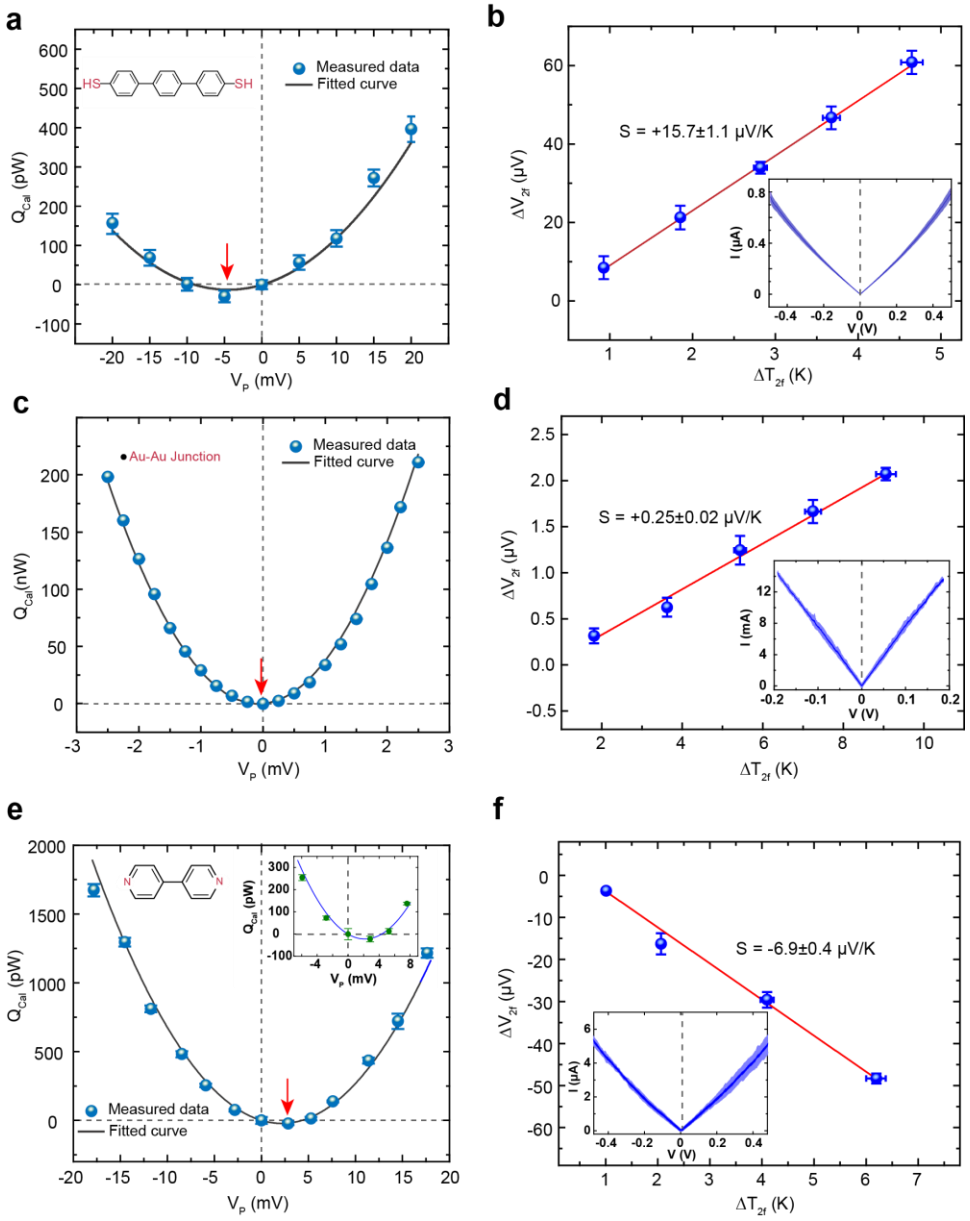

Figure 5.3: Measured Peltier effect in Au-TPDT-Au, Au-Au, and Au-BP-Au junctions.
a & b, As in Fig. 5.2c & d, but for TPDT junction. The black solid line indicates the fitted curve using transport parameters (low-bias conductance and Seebeck coefficient) input from independent characterizations of both properties. c & d, for Au-Au noncontacts in which negligible cooling effect is found. e & f, for BP junction. In contrast to BPDT and TPDT junctions, the maximum in cooling power is observed when a positive bias is applied, consistent with the physical picture of Peltier effect in LUMO-dominated molecular junctions (indicated by negative Seebeck coefficient in f).

Finally, we performed measurements using Au-4,4'-Bipyridine (BP)-Au MJs, in which transport is expected to be dominated by the lowest unoccupied molecular orbital (LUMO) level[66] (as also confirmed by our Seebeck measurements, see Fig. 5.3f). In these experiments, in contrast to the measurements in HOMO-dominated junctions, we observed net cooling in the calorimeter for a positive bias applied to the probe (Fig. 5.3e). The observed heat dissipation characteristics of Au-BP-Au junctions are consistent with the predictions of Eq. 1 using independent measurements of the electrical conductance and the Seebeck coefficient as reflected by the excellent agreement between the experimental data and the result from Eq. 1. The physical picture for the observed cooling behaviour in LUMO-dominated junctions is shown in Fig. 5.1e.

To identify the microscopic origin of the observed heating and cooling effects in our MJs, we employed an *ab initio* transport model based on density functional theory[196] (DFT) to compute the transmission function ($\tau(E)$). To investigate if our experimental observations are directly determined by the structure and properties of the molecules incorporated into the junction, we focus our computational analysis on single-molecule junctions. In Fig. 5.4a we summarize the results for the zero-bias transmission function for three junctions where the molecules under study (BPDT, TPDT, and BP) are attached to gold electrodes via atop positions (insets in Fig. 5.4b-d). For these calculations we used the DFT + Σ method to attenuate known self-interaction errors in DFT and account for image charge effects[39, 213]. Then, using $\tau(E)$ we computed within the Landauer theory the electrical conductance, the Seebeck coefficient, and the power released in the calorimeter (Eq. 1). Notice that since we are interested in the low-bias regime, the bias-dependence of the transmission is ignored.

For the Au-BPDT-Au and Au-TPDT-Au junctions, the transport at the Fermi energy (E_F) is dominated by the HOMO of the molecules (Fig. 5.4a), which results in a negative slope of the transmission at E_F and a positive Seebeck coefficient. In this example, the conductance of the BPDT junction is $1.1\text{x}10^{-3}$ G_0, where $G_0 = 2e^2/h = 12.9\ (\text{k}\Omega)^{-1}$ is the conductance quantum, while for TPDT the conductance is 1.5×10^{-4} G_0, i.e., almost an order of magnitude lower as expected from the exponential decay of the conductance with molecular length. The corresponding Seebeck coefficients at room temperature are +10.5 μV/K for BPDT and +11.1 μV/K for TPDT, which are in good accord with our experimental observations. The results for the computed cooling power in single molecule junctions (Fig. 5.4b & c) predict that these junctions exhibit cooling for negative bias in a voltage range of $V_P \in [-7\ mV, 0\ mV]$, in excellent agreement with the voltages range where cooling is observed in the experiments. The lower cooling power of TPDT is simply due to its lower conductance. Notice that the difference in power values with respect to the experiments is due to the fact that we are simulating single-molecule junctions instead of the many molecule junctions employed in the work. Finally, the BP junction exhibits a conductance of 8.8×10^{-5} G_0, consistent with previous experimental and theoretical work[66], the transport is dominated by the LUMO (Fig. 5.4a) with a negative Seebeck coefficient of -14.4 μV/K, and the cooling effect occurs at positive bias (Fig. 5.4d) in a range $V_P \in [0\ mV, +9\ mV]$, again in qualitative agreement with our observations. A direct quantitative comparison between theory and experiments is primarily limited by the uncertainty in the number of molecules in the junction (note however that the Seebeck coefficient is independent of the number of molecules). These results strongly suggest that the observed cooling and heating are determined by the intrinsic properties of individual molecules.

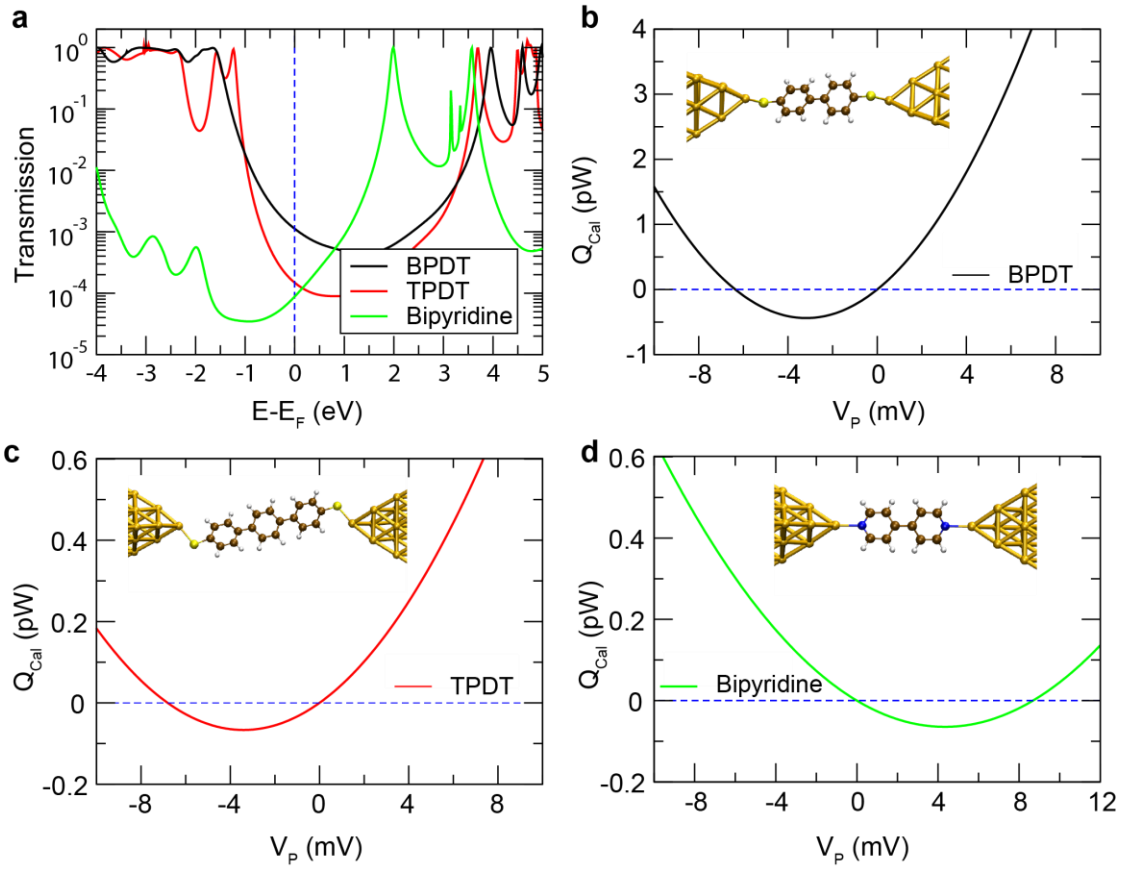

Figure 5.4: Computed heating/cooling effect in the molecular junctions employed in this experiment.
a, Calculated zero-bias transmission function as a function of energy, measured with respect to the Fermi energy (EF), for BPDT, TPDT, and BP junctions. The transmission and its derivative at EF determine the electrical conductance and the Seebeck coefficient of the molecular junctions, respectively. b-d, Calculated heating and cooling power at different voltages for BPDT, TPDT, and BP single-molecule junctions, respectively. The insets show the geometries used to compute the different transport properties.

5.4 Conclusion

In conclusion, we have experimentally observed cooling in molecular junctions. Our experimental results also link the charge transmission characteristics of a molecule to the Peltier effects measured in MJs. Furthermore, the experimental platform reported here allows the seamless characterization of electrical, thermal and thermoelectric transport properties on the same material in a unified manner. This work should stimulate further systematic exploration of atomic and molecular scale thermal transport[1, 15, 174, 214] and quantification of the thermoelectric figure of merit[18, 19, 45, 115] in a variety of interesting molecules, nanostructures, and materials.

5.5 Methods and Supporting Information

5.5.1 Preparation and Characterization of Microdevices

The microdevices were custom-fabricated using standard nano-fabrication techniques (Fig. 5.5). The suspended regions (80 μm × 60 μm) are connected to the surrounding substrate via thin and long beams that result in a thermal resistance of ~3.3 MK/W and a stiffness of ~3.85 N/m. The planar surface of the microdevice was coated by a gold thin film of ~50 nm (e-beam evaporation), on which a self-assembled monolayer of molecules was formed.

5.5.2 Molecular Monolayer Preparation and Junction Formation

To obtain the desired monolayers of molecules, we first prepared dilute ethanol or toluene solutions of BPDT, TPDT, and BP molecules (purity >95%, Sigma Aldrich). Immediately after the deposition of Au layers on the device surfaces we immersed the devices in 500 μM solutions to initiate self-assembly of molecules on Au surface. The microdevices were incubated for ~12 hours in a nitrogen-filled glove box and, following monolayer formation, they were rinsed thoroughly in ethanol or toluene to remove unbound molecules. Devices were dried in a nitrogen environment. Experiments were performed with commercially available AFM cantilevers from NanoAndMore (ARROW-CONTR, nominal force constant ~0.1 N/m). Prior to experimental measurements the AFM tips were coated with a thin layer of sputtered Au (~100 nm) and cleaned by oxygen-plasma to eliminate possible contamination. Measurements were initiated by making a gentle contact with the monolayer of molecules using a contact force of about 1 nN, which prevented penetration of the AFM tip into the monolayer and ensured stable and repeatable MJs with ~100 molecules. This estimate of the number of molecules in the junction (~100) was obtained by comparing the measured electrical conductance with previously reported

values of the single-molecule electrical conductance. Similar values were also obtained by employing a simple, contact-mechanics model that is based on Hertzian theory.

5.5.3 Thermoelectric Voltage Measurement

The Seebeck coefficients of the MJs were measured using an alternating current scheme. Briefly, a sinusoidal electric current at frequency f (0.5 Hz) was supplied to the Pt resistor, which induced sinusoidal perturbation of the temperature of the suspended microdevice with an amplitude ΔT_{2f} and frequency $2f$. Subsequently, we used a lock-in amplifier (Stanford Research Systems, SRS 830) to measure the thermoelectric voltage (ΔV_{2f}) at $2f$ = 1Hz arising from the applied ΔT_{2f}. The Seebeck coefficient of the junction (S) was found from $S = S_{Au} - \Delta V_{2f}/\Delta T_{2f}$. where S_{Au} is the Seebeck coefficient of the Au thin film deposited on our calorimeter, which was assumed to be ~1.76 μV/K[215].

5.5.4 Computational Techniques

The transmission functions and the different transport properties of the single-molecule junctions used in this work were obtained with our previously published first-principle transport method[196]. Briefly, this method is based on the combination of density functional theory (DFT) and non-equilibrium Green's function (NEGF) techniques, and it is implemented in the quantum-chemistry code TURBOMOLE[216]. The first step in this method is the description of the electronic structure of the junctions within DFT. For all calculations we used the BP86 exchange-correlation functional[217] and the Gaussian basis set def-SVP[218]. The total energies were converged to a precision of better than 10^{-6} atomic units, and structure optimizations were carried out until the maximum norm of the Cartesian gradient fell below 10^{-4} atomic units. To construct the molecular junctions, we first placed the relaxed molecules in between two gold clusters with

20 atoms that end in a single atom (atop binding). Then, we performed a new geometry optimization by relaxing the positions of all the atoms in the molecule as well as the four gold atoms that are closest to the molecule on each cluster, while the other gold atoms were kept frozen. The size of the gold cluster was then increased to 63 atoms on each side to describe correctly both the metal-molecule charge transfer. Finally, the central region, consisting of the molecule and one or two Au layers was coupled to ideal gold surfaces, which serve as infinite electrodes and are treated consistently with the same functional and basis set within DFT[196].

To address the known problems of DFT-based methods to accurately describe the energy gap and metal-molecule level alignment, we used the self-energy corrected DFT + □ method that partially cures the self-interaction errors in the standard exchange-correlation functional and, in turn, takes into account image charge effects[213]. We have described in detail the implementation of this method in past work[39]. Briefly, there are two key steps in this method. First, we shift the HOMO and LUMO of the molecules such that they correspond to the negative ionization potential and to the negative electron affinity, respectively. These two latter energies are computed in separate calculations of the molecule in gas phase. Then, to account for the renormalization of the levels when the molecule is brought into the junction, we shift the energy of the occupied states up in energy and the unoccupied states down in energy. These shifts are calculated by describing the screening of the metallic electrodes in a classical way as the interaction of point charges in the molecule with two perfectly conductive infinite surfaces.

The last step in our transport method is the use of the information about the electronic structure of the junctions to determine the zero-bias transmission function. This is done with the help of NEGF techniques, as explained in our past work[39]. Finally, the transmission function was used, in the spirit of the Landauer theory, to compute the different transport properties. In

particular, the linear conductance *G* and Seebeck coefficients *S* are given in terms of the zero-bias transmission function *τ(E)* as:

$$G = G_0 K_0(T) \; and \; S = -\frac{K_1(T)}{eTK_0(T)} \tag{2}$$

where *T* is the absolute temperature, *e* is the electron charge and the coefficients $K_n(T)$ are given by $K_n(T) = \int_{-\infty}^{+\infty}(E - E_F)^n \tau(E)\left[-\frac{\partial f(E,T)}{\partial E}\right] dE$. Here, E_F is the Fermi energy and $f(E,T)$ is the Fermi-Dirac function. Finally, the power released in the calorimeter was calculated with the help of Eq. 1 in the text. In particular, we verified that the low-bias expansion of that equation applies in the voltage range investigated in this work.

5.5.5 Nanofabrication Process of Suspended Calorimetric Devices

The detailed steps for fabricating the suspended calorimetric microdevices are shown in Fig. 5.5. Briefly, a low-stress silicon nitride (SiN_x) film that is 500 nm thick is first deposited onto a silicon wafer using LPCVD (Step 1). Subsequently, a 30 nm thick Pt serpentine line is patterned onto the SiN_x layer using lift-off (Step 2). Then, Au leads with a thickness of 100 nm are defined on the SiN_x layer using the same lift-off process (Step 3). The topology of the suspended region and the beams is created using RIE etching through the SiN_x layer on the front side (Step 4). Windows in the SiN_x layer, located on the backside of the silicon wafer, are then etched using RIE (Step 5). Subsequently, a through-hole in the silicon handler wafer is created by a KOH etch to release the suspended device (Step 6). After releasing the device, a 100 nm thick Al_2O_3 film is deposited on the whole device using atomic layer deposition (ALD) (Step 7) and serves to electrically isolate the Pt serpentine from the Au layer that will be deposited in the final step. Finally, the microdevice is coated with a 50 nm thick Au film that is deposited using

sputtering (Step 8). Immediately after the deposition of the Au thin film, the microdevice is immersed into a molecular solution to form a self-assembled monolayer (SAM) of molecules.

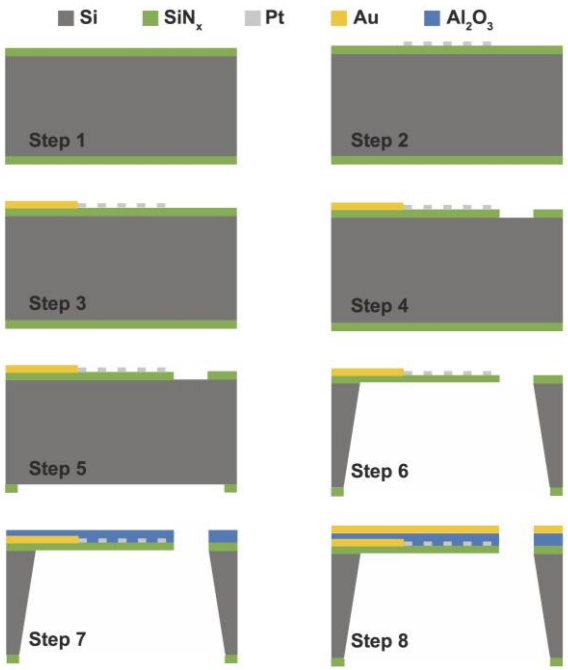

Figure 5.5: Nanofabrication of the suspended calorimetric devices.

5.5.6 Measurement of the Thermal Resistance and Time Constant of the Calorimetric Devices

The thermal resistance of the suspended microdevices was calibrated using an approach similar to that described in our previous work[174]. Briefly, the temperature rise of the device was measured by supplying a range of dc electrical currents to the integrated Pt serpentine line, which dissipated known amounts of heat in the suspended region of the microdevice. Figure 5.6a plots the measured temperature rise (ΔT) against the power input (Q). The thermal resistance of the microdevice can be readily obtained by using $R_S = \Delta T / Q$, which was estimated to be 3.35 ($\pm$0.01) $\times 10^6$ K/W.

To calibrate the thermal time constant of the microdevice, we supplied a sinusoidal heat current with fixed amplitude (I_f = 4 μA) and systematically varied the frequency of the current while measuring its temperature response. The Joule heating (Q_{2f}) occurs at a frequency 2f and produces temperature oscillations in the microdevice with an amplitude of ΔT_{2f}. This 2f component of the temperature change of the microdevice can be related to the voltage drop across the Pt thermometer at 3f, V_{3f}, using the relationship $V_{3f} = \Delta T_{2f} \alpha I_f R/2$, where α is the temperature coefficient of resistance and R is the nominal resistance of the Pt thermometer. The measured amplitude of the temperature fluctuations, normalized to the amplitude of the measured value at the lowest frequency, is plotted against the frequency in Fig. 5.6b. We note that the cut-off frequency (-3dB point) is at ~4 Hz. Therefore, the thermal time constant (τ) of the microdevice can be obtained using $\tau = (2\pi f_{-3dB})^{-1}$ ~ 40 ms.

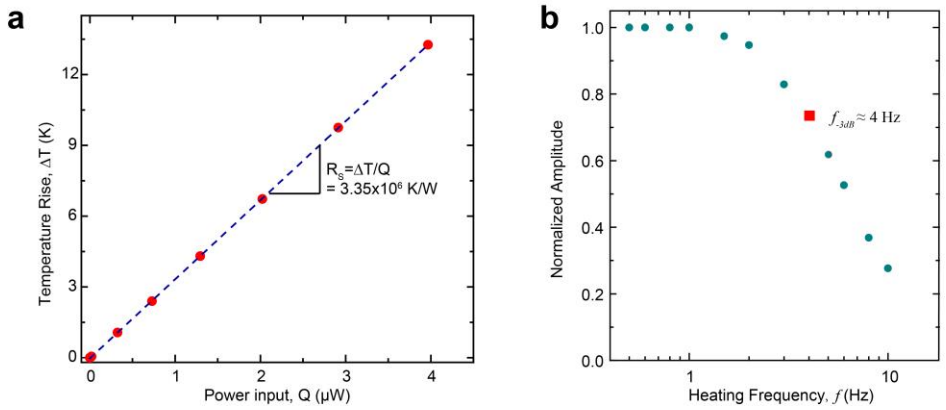

Figure 5.6: Calibration of the thermal resistance and thermal time constant of the calorimetric devices.
a, Measured temperature rise of the device as a function of the input power. The thermal resistance is given by the slope of the fitted curve. b, Normalized temperature rise of the device as the frequency of the sinusoidal heat input is varied. The red square indicates the -3dB point.

5.5.7 Surface Characterization of the Microdevices

The surface topography of the Au-coated microdevices was characterized by atomic force microscopy (AFM). As shown in Fig. 5.7, the RMS roughness of the suspended region was

found to be less than 0.4 nm within a scanning area of 500 nm by 500 nm. We note that this flatness is comparable to that for template-stripped Au surfaces and facilitates the formation of self-assembled monolayer of molecules on the Au surface.

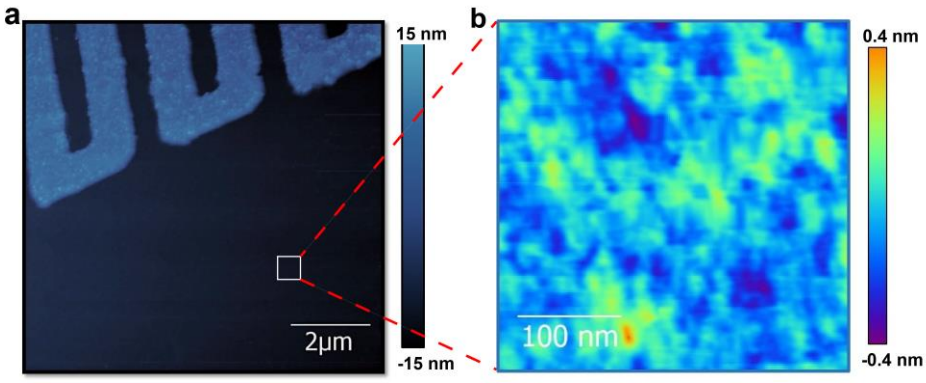

Figure 5.7: Surface topography of the suspended microdevices obtained by Atomic Force Microscopy (AFM). a, The Pt serpentine thermometer can be seen in (a). b, AFM scans performed on the planar region of the microdevice reveal a RMS roughness of ~0.4 nm within a 500 nm by 500 nm area.

5.5.8 Calibration of the Spring Constant of the AFM Probes

The spring constant of the AFM probes is estimated using the equipartition theorem. Briefly, the spring constant of the AFM probes (k) and the temperature (T) of the thermal reservoir that the probe is connected to are related by $k \langle x^2 \rangle = k_B T$ where k_B is the Boltzmann constant is the displacement of the end of the tip due to random thermal fluctuation in the probe. To obtain the mean square displacement, $\langle x^2 \rangle$, we monitored the thermally-driven deflections of the AFM cantilever with a position-sensitive photodiode detector. From a time series of the AFM cantilever displacement we computed the power spectral density (PSD) of the thermally driven oscillations. As shown in Fig. 4.8, the PSD features a peak at ~13 kHz that corresponds to the resonant frequency of the AFM cantilever. The mean square displacement $\langle x^2 \rangle$ was obtained by integrating the PSD and was found to be ~0.039 nm^2. Finally, by substituting the estimated value of $\langle x^2 \rangle$ into the equipartition theorem the spring constant can be calculated to be ~0.1 N/m.

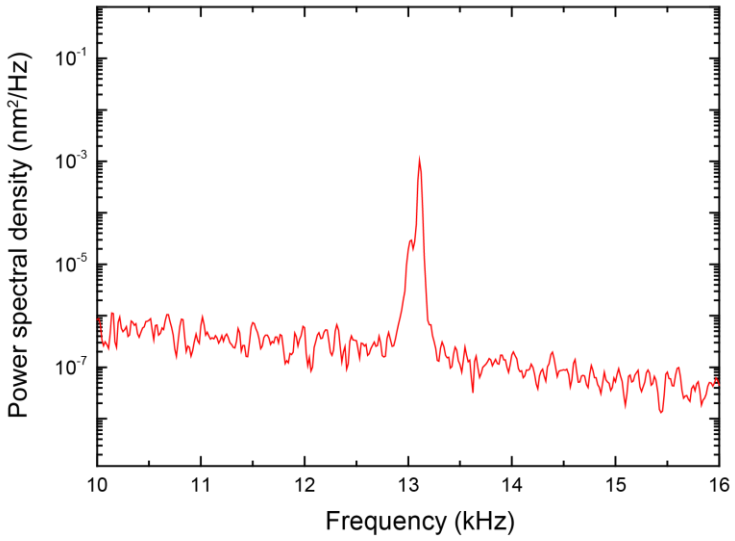

Figure 5.8: Power spectral density (PSD) of the deflection of AFM cantilever.
The peak frequency at ~13 kHz corresponds to the resonance frequency of the cantilever, and the thermally-driven, mean squared displacement of the cantilever is about 0.039 nm^2.

5.5.9 Evaluation of the Stiffness of the Suspended Calorimetric Devices

Thermal fluctuations of suspended microdevices need to be minimized to sub-nanometer levels for creating stable molecular junctions, which requires that the suspended devices have sufficiently high mechanical stiffness. To measure the stiffness of the calorimetric devices we employed an approach similar to that used in a previous work[219]. Briefly, we employed an AFM cantilever with a known spring constant (k_{Can}) of ~0.75 N/m and placed it in close proximity to a solid silicon (Si) substrate. The substrate was first displaced towards the cantilever and the force exerted on the cantilever as a function of the displacement was recorded (Fig. 5.9). Subsequently, we systematically repeated the same experiments with a suspended device (suspended region attached to a Si substrate via thin and long beams, see Fig. 5.1). The measured force vs. displacement curves are shown in Fig. 5.9. It can be seen that the slope of the force vs. displacement curve (m_1) recorded on the solid substrate is greater than the curve (m_2) obtained with the compliant device. The difference in force exerted on the cantilever in the two

experiments is attributable to the compliance of the suspended device. Specifically, it can be shown that the stiffness of the suspended device (k_{Sus}) can be related to the stiffness of the cantilever (k_{Can}) by the following expression$k_{Sus} = k_{Can}/[\frac{m_1}{m_2} - 1]$, which yields a stiffness for the microdevice of 3.85 ± 0.11 N/m. This stiffness is significantly higher than the stiffness of the AFM probes used in the measurement (~0.1 N/m) and thus does not limit the stability of our junctions.

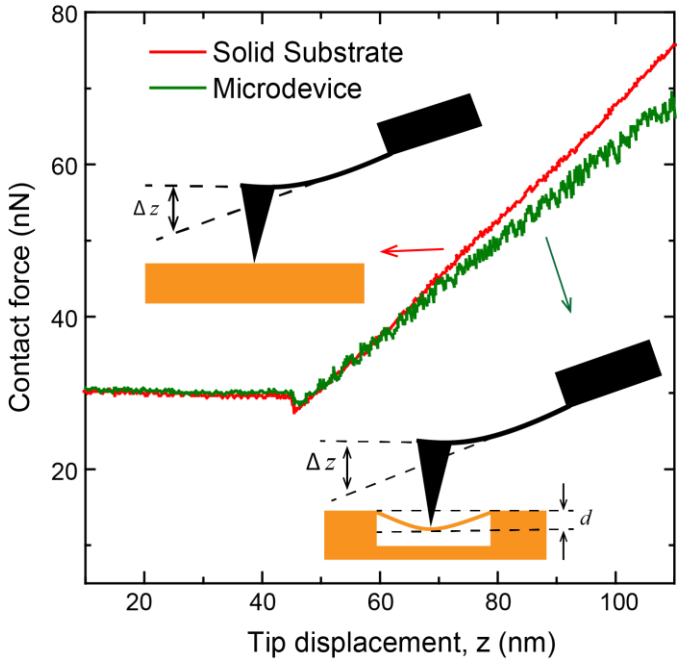

Figure 5.9: Stiffness calibration of the suspended calorimeter.
Force-displacement curves of an AFM probe on the calorimeter and a solid substrate. The insets show the differences in deflection in the two different experiments. The stiffness of the microdevice calorimeter can be estimated from these measurements as described in the text.

5.5.10 Analysis of the Uniformity of the Temperature Distribution of the Suspended Calorimeters

In measuring the heating and cooling power of the molecular junctions, one important question is whether the temperature of the suspended region is uniform when heating or cooling occurs in a localized area. To address this issue, we employed a COMSOL-based finite element analysis to analyze the temperature distribution within the microdevice in the presence of a finite

heat flux (300 nW) applied to a small spot (~20 nm^2) on the surface. Figure 5.10 presents the meshing topology used in the simulation and the calculated result. It can be clearly seen that the temperature drop occurs primarily along the beams connecting the suspended region to the thermal reservoir and there are negligible thermal gradients across the suspended region. This ensures that the temperature reported by the Pt thermometer integrated on the suspended region can be readily used to estimate the thermal power applied on the microdevice.

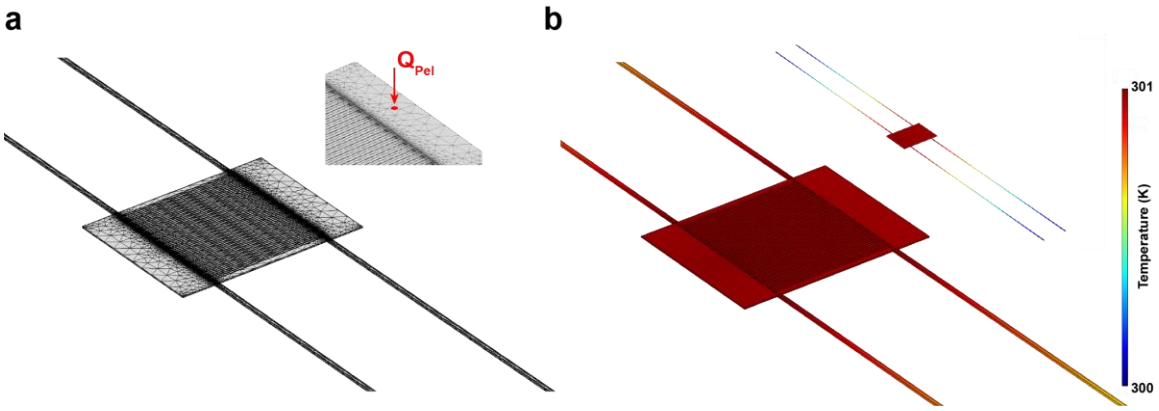

Figure 5.10: Modelling of the temperature distribution on the calorimetric microdevice.
a, Meshing structure used in the simulation. A known amount of thermal power (300 nW) is applied to a small spot with an area of ~20 nm^2 at the edge of the suspended calorimeter device (see inset). b, Calculated temperature field when the temperature increases by ~1 K on the suspended region. The temperature gradient is primarily restricted to the beams (see inset).

5.5.11 Ultralow Noise Measurement Environment

All measurements described in this work were performed using a ultra-high vacuum scanning probe microscope (RHK UHV 7500), which was housed in an ultra-low-noise facility that features excellent vibration-isolation (meeting the stringent NIST-A criterion) and temperature stability (<100 mK drift over 24 hours).

5.5.12 Characterization of the Self-assembled Monolayer of Molecules

We employed X-ray photoelectron spectroscopy (XPS) and ellipsometry to determine the monolayer thickness of the self-assembled monolayer. The representative measured results are presented and the estimated thicknesses are summarized in Fig. 5.11. The XPS experiments were performed on a Kratos Axis Ultra system using a monochromatic Al X-ray source at a setting of 8 mA and 14 kV. The estimated thickness is based on the exponential attention of the substrate photoelectrons in the presence of the self-assembled monolayer[220, 221, 222, 223] (as shown in Fig. 5.11).

The ellipsometry measurements were performed on the Woollam M-2000 Ellipsometer. Incident light beams at angles of 55, 65 and 75 degree, over the wavelengths from 400-1700 nm were used for this characterization and the data were fit with an optical model (using CompleteEASE^{TM} V4.86) to extract the thickness of the monolayer. It can be seen in Fig. 5.11 that the two measurement approaches yield consistent results, which agree well with previously reported thicknesses[87, 224, 225, 226].

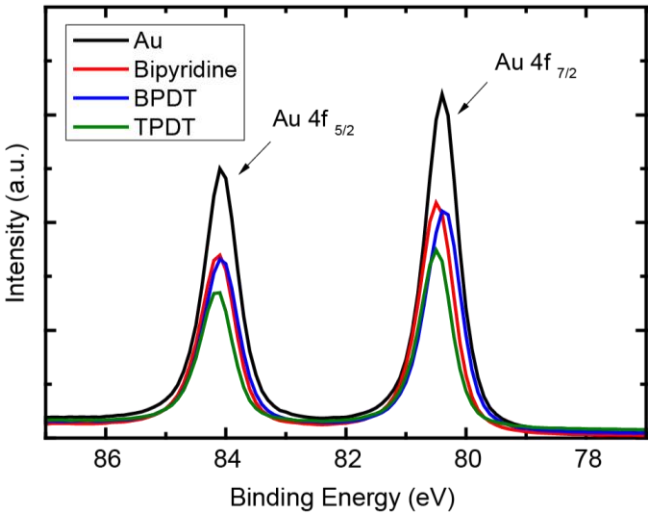

	BPDT	TPDT	Bipyridine
XPS (nm)	1.29 ± 0.14	1.85 ± 0.19	1.19 ± 0.16
Ellipsometry (nm)	1.47 ± 0.07	1.86 ± 0.08	0.91 ± 0.08

Figure 5.11: Characterization of the self-assembled monolayer using XPS and Ellipsometry.

The number of molecules in the junctions can be estimated by applying a simple, contact-mechanics model (Hertzian theory). Specifically, the radius of contact between the Au AFM tip and the SAM can be estimated from Hertzian contact mechanics[227] to be $r = \sqrt[3]{R_{tip}F/E}$, where R_{tip} is the radius of the tip, F is the apparent load on the contact, and E is the Young's modulus. Taking F to be 16 nN which sums the pull-off load of ~15 nN and the applied load of 1 nN, R_{tip} = 100 nm, and E = 79 GPa for Au, we estimate the contact radius r to be 2.7 nm, corresponding to a contact area of ~23 nm^2. Based on the expected packing density of the benzene dithiol molecules on the Au[228] substrate of ~5×10^{14} mole/cm^2 we estimate that the junction contains approximately 100-110 molecules. Moreover, we also employed the well-known Johnson-Kendall-Roberts (JKR) model[229] which was developed based on the classic Hertzian contact mechanics to calculate the contact area and didn't find significant difference in estimating the number of molecules compare to the classic model. Furthermore, the number of molecules in the junction can also be justified from the electrical conductance measurement. By comparing the reported value of the single-molecule junction, BPDT for example which is ~2.6 MΩ ($5 \times 10^{-3} G_0$)[230] to the measured electrical conductance of the SAM which is ~37 μS (27 KΩ), we can estimate the number of the molecules in the junction to be approximately 100, by assuming the electrical conduction of the molecules are independent from each other.

5.5.13 Electric Circuitry

As depicted in Fig. 4.1, the low-bias electrical conductance of the molecular junctions is measured by applying a small voltage bias (below 20 mV) across the junctions and measuring the electric current using a current amplifier (Keithley 428). The current-flow in the molecular junctions generates both Peltier and Joule effects in the electrodes. The thermal power (heating or cooling) was measured by monitoring the temperature change of the suspended calorimeter using the integrated Pt thermometer. This was accomplished by measuring the electrical resistance change of the Pt resistor in a half-Wheatstone bridge configuration whose voltage output was first amplified by an instrumentation amplifier (AD 524) with a gain of 100, and then supplied into a second voltage amplifier (SRS 760) with a gain of 10. Furthermore, current-voltage (I-V) characteristics of the molecular junctions were measured by linearly increasing the voltage bias (from ~ -0.5 V to 0.5 V) and measuring the resultant electric current. The approach employed for measuring the Seebeck coefficients of molecular junctions is shown in Fig. 5.12.

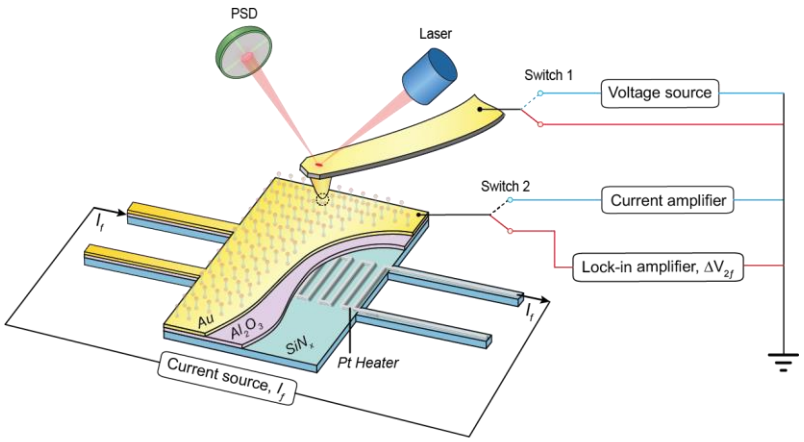

Figure 5.12: Schematic describing the approach employed for thermoelectric voltage measurements on molecular junctions.

Temperature change (ΔT) of the microdevice due to the Peltier cooling/Joule heating in the molecular junction can be estimated by $\Delta T = V_{Cal}/I_{in}R_{Pt}\alpha$, where V_{Cal} is the voltage output

across the Pt thermometer, I_{in} is the input electric current (see Fig. 5.1a) and R_{Pt} and α are the resistance the temperature coefficient of resistance of the Pt thermometer, respectively. We note that the Joule heating induced by I_{in} is estimated to elevate the temperature of the microdevice by ~10 K.

5.5.14 Details of Applying the Time Averaging Scheme in Data Processing

To implement the time averaging scheme measurements of heating and cooling in AMJs, we applied repeated sequences of three level voltage biases across junctions and recorded the resulting electrical conductance and the temperature rise of the suspended calorimeter for an extended period of time. Depending on the desired signal to noise ratio and the magnitude of the thermal power output, the number of three-level periods over which data were collected was varied. Specifically, for the data shown in Fig. 5.2b the number of periods over which data were averaged at each bias are as follows: 450 (9 mV), 720 (8 mV), 1320 (7 mV), 600 (5 mV), 1500 (2 mV), and 2000 (1 mV), respectively. In general, the number of periods required to resolve signals increased with decreasing power output.

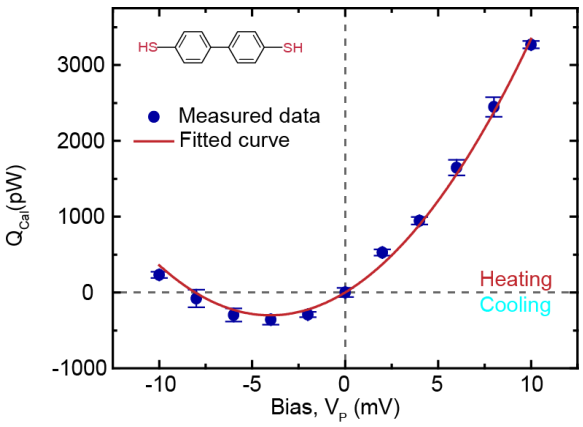

Figure 5.13: Second independent data set for the voltage-dependent cooling/heat generation in BPDT junctions.
The solid red line indicates the fitted curve using Eq. 1 and the measured Seebeck coefficient and electrical conductance (data not shown for the Seebeck coefficient and electrical conductance).

In performing these heat dissipation/cooling measurements we observed small changes in the electrical conductance of the junction (~5 - 10 %) during the time course of the measurement. In order to (systematically) account for the variations of the conductance we normalized all the measured power outputs by the electrical conductance relative to that measured at a bias of 3 mV. Finally, we note that these results are independent of the samples and were found to be repeatable with multiple probes and microdevices calorimeters. An additional data set from a different microdevice and probe obtained over a wider range of biases for BPDT MJs is shown in Fig. 5.13.

5.5.15 Description of the Temperature Resolution of the Pt Thermometer

To evaluate the temperature resolution of the Pt thermometer of the calorimeter, we followed the protocols developed by us in previous work[12, 13]. Briefly, our measurement applied an un-modulated electrical current into the Pt line to quantify the modulated temperature change due to the applied three-level voltage bias. The noise components in this experiment include contributions from the electronic system (amplifiers), thermal Johnson noise, shot noise, and the temperature fluctuation from the ambient environment. Following the procedure described in detail elsewhere[173] by us we estimate that the temperature resolution of our modulations based approach to be given by:

$$\Delta T_{Res} = \left[\int_0^{\infty} G_N(f) \left[\frac{\sin(2\pi f T)}{2\pi f T} \right]^2 \times \left[\frac{6\sin(\pi f \Delta t)}{1 + 2\cos(2\pi f \Delta t)} \right]^2 df \right]^{1/2} \quad (3)$$

where $G_N(f)$ is the power spectral density associated with temperature noise, $3\Delta t = 5$ seconds (i.e. the period of each three level cycle) and $2T$ is the total time over which each set of three level excitations were performed. For example, as described in the section above for the bias

with 1 mV amplitude, the three level excitation for this measurement was repeat for a total of 2000 cycles, where each cycle was 5 seconds long. Therefore, 2T = 2000×5 = 10,000 seconds for the 1 mV voltage amplitude experiments. Further, we note that we have previously[188] analyzed the noise spectral characteristics of resistance thermometers and had estimated $G_N(f)$. Using this information in conjunction with Eq. 3, we estimate, that for measurements performed for 2000 cycles, our temperature resolution is better than 0.1 mK, thus giving us a heat current resolution that is below 30 pW.

5.5.16 Physical Mechanisms of Cooling and Heat Dissipation in Molecular Junctions

To qualitatively understand the physical processes that result in cooling we consider the schematics shown in Fig. 4.14a-c where the left electrode is grounded and represents the electrode integrated into the calorimeter and the right electrode is negatively biased and represents the probe. In these scenarios electrons are injected into the right electrode (probe) at an energy of $\mu_{Cal} + e|V_P|$ and leave the left electrode (calorimeter) at an energy μ_{Cal}. This implies that if N electrons flow through the junction there is a net heat dissipation that is given by $Ne|V_P|$.

To understand the origin of cooling it is essential to first note that flow of charge occurs in a range of energies, *i.e.* at all energies between the chemical potentials of the electrodes and in a small range of energies (~few k_BT) above the chemical potential of the probe and below the chemical potential of the calorimeter. As is described in more detail below, the electrons flowing between the chemical potentials of the electrodes cause heating in both electrodes. However, the electrons flowing above the chemical potential of the probe ($\mu_{Cal} + e|V_P|$) produce heating in the calorimeter and cooling in the probe. Further, electrons flowing below the chemical potential of the calorimeter (μ_{Cal}) cause cooling in the calorimeter and heating in the probe. From this

discussion it is obvious that, for the given bias conditions, if the number of electrons transmitted below μ_{Cal} dominate the charge transfer then it is possible to achieve net cooling in the calorimeter. Below, we first describe the heating and cooling characteristics of electrons transmitted at various energies.

Heating/Cooling due to electrons transmitted between chemical potentials: Fig. 4.14a shows the scenario where an electron is transmitted at an energy E between the chemical potentials. In this case the electron must dissipate as heat some of its energy ($\mu_{Cal} + e|V_P| - E$) in the probe and the rest of energy of ($E - \mu_{Cal}$) in the calorimeter. Thus, charge transfer at energies between the chemical potentials results in heat generation in both the electrodes and the total heat generation per electron is $e|V_P|$.

Heating/Cooling due to electrons transmitted above the chemical potential of the probe: When electrons are transmitted at an energy $E > \mu_{Cal} + e|V_P|$ (see Fig. 5.14b) the electrons absorb energy $E - \mu_{Cal} - e|V_P|$ from the probe resulting in cooling in the probe and dissipate energy $E - \mu_{Cal}$ in the calorimeter. Notice that the net heat generation by the electron in the device $(E - \mu_{Cal})-(E - \mu_{Cal} - e|V_P|) = e|V_P|$. is still the same as that for electrons transmitted between the chemical potentials.

Heating/Cooling due to electrons transmitted below the chemical potential of the calorimeter: When electrons are transmitted at an energy $E < \mu_{Cal}$ (see Fig. 5.14c) they dissipate as heat some energy ($\mu_{Cal} + e|V_P| - E$) in the probe resulting in heating of the probe and they absorb some energy ($E - \mu_{Cal}$) in the calorimeter, resulting in cooling of the calorimeter. Again, notice that the net heat generation by the electron in the device $((E - \mu_{Cal})-(E - \mu_{Cal} - e|V_P|) = e|V_P|)$ is still the same as that for electrons transmitted between the chemical potentials.

Relationship between transmission function and cooling: From the qualitative description provided above it is clear that when the calorimeter electrode is grounded and the probe is negatively biased, net cooling can occur in the calorimeter if the cooling provided by electrons transmitted below μ_{Cal} is larger than the heating produced by electrons transmitted at other energies. This can happen only when the transmission probabilities are larger at m_{Cal} than those at $\mu_{Cal} + e|V_P|$. This in turn implies that the transmission function has a negative slope, implying a positive Seebeck coefficient. This prediction is consistent with Eq. 1, which suggests that when a negative bias is applied to the probe, the calorimeter can be cooled if the Seebeck coefficient of the junction is positive. From the qualitative arguments provided above it can also be seen that, for net cooling to be observed, the heat dissipation due to electrons transmitted between the chemical potentials must also be small as they result in only heat dissipation. For this reason, cooling can only be observed at low voltage biases. Finally, if the transmission function is only weakly dependent on energy then the cooling due to electrons transmitted below μ_{Cal} and heating due to electrons transmitted above $\mu_{Cal} + e|V_P|$ tend to cancel each other resulting in no observable cooling.

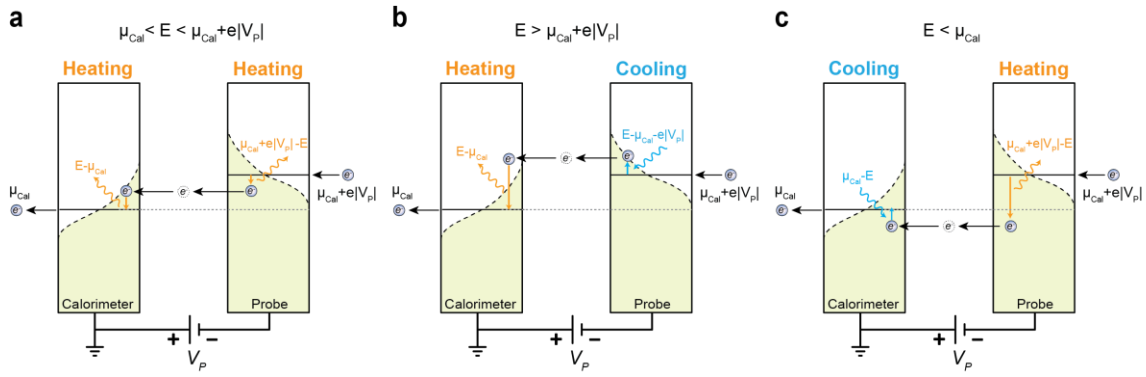

Figure 5.14: Schematic describing the physical mechanism involved in heating and cooling in molecular junctions.
a, The scenario where an electron is transmitted between the chemical potentials of the electrodes. b, The scenario where an electron is transmitted above the chemical potential of the probe. c, The scenario where an electron is transmitted below the chemical potential of the calorimeter.

Chapter 6: Radiative Heat Transport in Ångström Sized Gaps

Reproduced with permission from *Nature Communications*. See Ref.[198]

Longji Cui, Wonho Jeong, Victor Fernandez-Hurtado, Johannes Feist, Francisco J. Garcia-Vidal, Juan Carlos Cuevas, Edgar Meyhofer and Pramod Reddy

6.1 Abstract

Radiative heat transfer in the extreme near-field (gap-sizes <10 nm) is of great current interest[231, 232, 233, 234, 235]. Here, we report studies of radiative heat transfer for gap-sizes of a few Å to 5 nm, performed under ultra-high vacuum conditions between a stiff Au-coated probe featuring embedded Cr-Au thermocouples and a heated planar Au substrate. Past measurements[232, 236, 237] performed in ultra-high vacuum conditions showed large apparent near-field conductances that are larger than the predictions of state-of-the-art fluctuational electrodynamics[238, 239] calculations by more than three orders of magnitude. In order to understand the source of this discrepancy we systematically studied extreme near-field radiative heat transfer after subjecting Au surfaces to various surface cleaning procedures. We found that insufficiently cleaned samples lead to unexpectedly large thermal conductances and feature a small apparent tunnel barrier height[202] (1 eV) suggesting the presence of surface contamination. When the probe and substrate were systematically cleaned following protocols involving plasma-cleaning/locally crashing the tip into the substrate the apparent barrier heights were found to increase to values as large as 2.5 eV and the observed near-field conductances decreased to

extremely small values—below the detection limit of our probe—as expected by our computational results. Our results show that surface contaminants, that confound the interpretation of near-field radiative heat transfer measurements, can be reproducibly eliminated paving the way for systematic future studies.

6.2 Introduction

Study of radiative heat transfer at the nanoscale is of fundamental interest[231, 240, 241, 242, 243, 244, 245], with potential applications such as thermophotovoltaic energy conversion[234], non-invasive thermal imaging[235], heat assisted magnetic recording[246], thermal modulation[247, 248], heat rectification[249], and super-resolution thermal lithography[250]. It has been predicted[244, 251], based on theoretical framework of fluctuational electrodynamics[238], that the radiative heat flux can exceed the Planck's blackbody limit by several orders of magnitude when two surfaces are brought into the near-field (gap size smaller than the Wien's wavelength, ~10 μm at room temperature). With the advancement of new experimental techniques over the past decade, several measurements[200, 231, 240, 252, 253] have been performed to demonstrate this super-Planckian effect for gap sizes as small as 2 - 3 nanometers. Generally, the results from these measurements were found to be in good agreement with the predictions based on fluctuational electrodynamics for a broad range of materials and geometries.

In spite of the important progress described above, there remains significant disagreement in the literature about radiative heat transfer in the extreme near-field (gap size <10 nm). Specifically, recent measurements[232, 236, 237] for two gold (Au) coated surfaces with gap-size in the range of ~0.2 – 10 nm have suggested an extraordinarily large near-field enhancement—over 3 orders of magnitude larger than the predictions from conventional fluctuational electrodynamics. These surprising results question the validity of current theories of heat transfer

for these small gaps. Researchers have explored the possibility of reconciling the experimental data with computations, by relaxing the local approximation[251] that is often employed in calculations of near-field radiative heat transfer, however, such investigations[254, 255] suggest that the inclusion of non-local effects results in relatively modest changes to heat fluxes in the extreme near-field (down to gap-sizes of a few Å). Computations[256], based on microscopic Maxwell's equations, for plane parallel surfaces of sodium chloride have also shown that deviations from the predictions of fluctuational electrodynamics, e.g. via phonon tunneling and phonon conduction, occur only for gap-sizes <0.5 nm and are smaller than a factor of 10 even at gap-sizes of ~3 Å. Further, recent work by us[231], performed using cantilevers with embedded thermocouples, quantitatively measured the extreme near-field radiative heat transfer (down to ~3 nm gap-sizes) for both polar dielectric and metallic materials. In contrast to the tunneling current based measurement of gap-size employed by others[232, 236, 237], our measurements were performed using compliant cantilevers that enabled direct detection of mechanical contact ensuring that we performed measurements only under conditions where a vacuum gap was present between the surfaces that were being studied. However, due to the compliance of the cantilevers the smallest gaps that could be accessed were in the 2 – 3 nm range. Although our work found excellent agreement with the predictions of fluctuational electrodynamics down to gap-sizes of 2 – 3 nm (deviations were <15%), it remains unclear if large discrepancies between theory and experiment, as reported by recent experimental work[232, 236, 237], arise in gaps of a few Ångströms.

6.3 Experimental Results and Analysis

Towards resolving this important issue, we first experimentally studied radiative heat transfer, using custom-fabricated scanning thermal microscopy (SThM) probes, in gap-sizes that

were varied from 5 nm down to a few Å (Fig. 6.1). A key characteristic of these SThM probes is their high stiffness (~10000 N/m), which is in strong contrast to the compliant probes (~5 N/m)[257] used in our recent work[231], enabling measurements down to Å-sized gaps. These SThM probes also feature integrated Au-Cr thermocouples (Fig. 6.1a), located in close proximity to the probe tip to form a sensitive thermal sensor[173, 257] with a very small thermal time constant (~10 μs)[173] and a spherical Au tip with a diameter of ~300 nm. In order to study radiative heat transfer in nanoscale gaps we mounted the SThM probes into an ultra-high vacuum scanning probe instrument and recorded the change in the thermovoltage across the thermocouple. A SThM probe, that was initially at a temperature T_{probe}, was displaced at a constant speed (0.1 nm/s) by piezoelectric actuation towards a planar Au sample at an elevated temperature T_{sample}. The applied temperature differential $\Delta T = T_{sample} - T_{Probe}$, results in a radiative heat flow (Q) from the Au sample to the probe and elevates the probe temperature to $T_{probe} + \Delta T_{probe}$. From the thermal resistance network shown in Fig. 1a the near-field radiative thermal conductance (G_{Rad} = $(R_{Rad})^{-1}$), is determined to be $G_{Rad} = Q / \Delta T$, where Q can be related to the thermal resistance of the probe (R_P) by $Q = \Delta T_{probe} / R_{probe}$. We note that the resistance of the probe R_{probe} was independently measured to be $\sim 9 \times 10^4$ K/W, following an approach developed by us recently[258]. Further, ΔT_{probe} was related to the thermovoltage (V_{th}) generated across the Au-Cr thermocouple by $\Delta T_{probe} = V_{th} / S_{Au-Cr}$, where $S_{Au\text{-}Cr}$ = 16.3 μV/K is the Seebeck coefficient of the thermocouple[173]. We determined "contact" of the probe with the sample by applying a small AC bias of 1 mV at 10 kHz across the tip and the sample and monitoring the amplitude of the tunneling current at the same frequency using a lock-in amplifier. For the purposes of this experiment we defined contact as the situation when the tunneling current exceeds an amplitude

of 10 nA, corresponding to a tunneling resistance of ~0.1 MΩ, which is known to correspond to a very small gap-size[259, 260] (1 – 2 Å). We note that the effect of Joule heating due to the tunneling current is negligible (~5 pW) as it is much smaller than the radiative heat flux (see below).

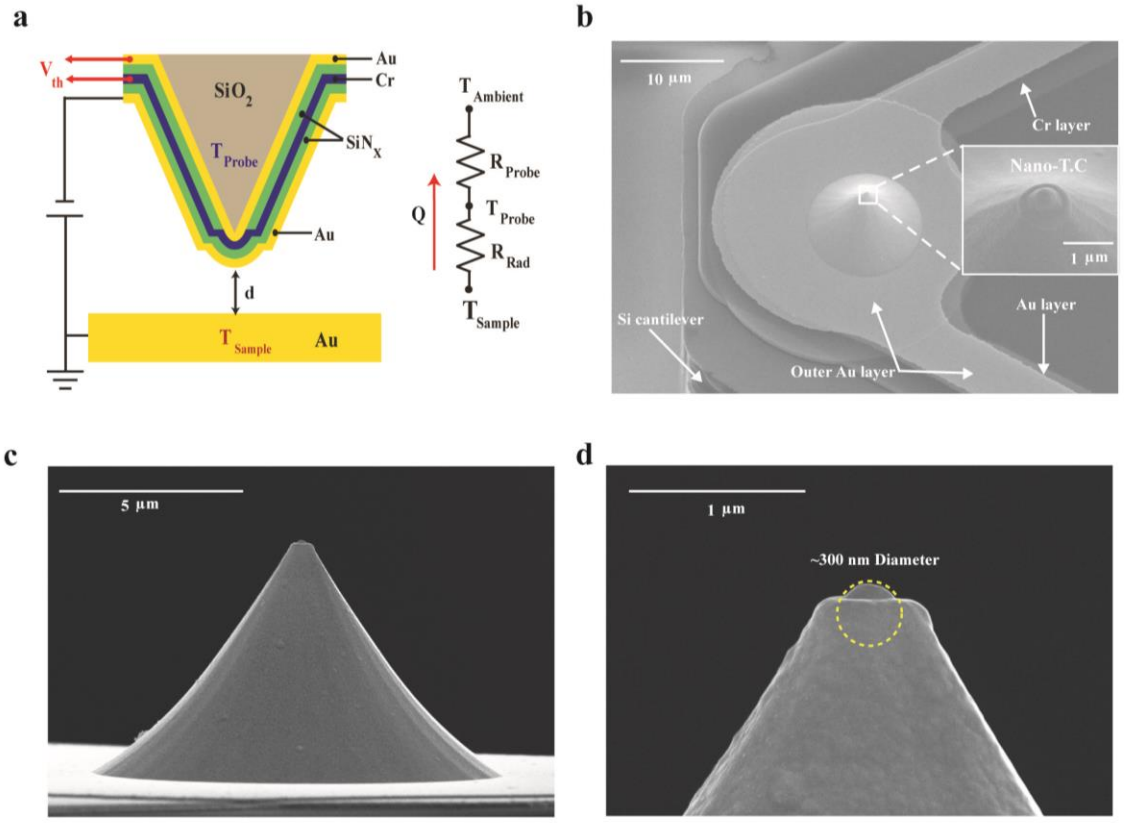

Figure 6.1: Experimental set-up and SEM images of Scanning Thermal Microscope (SThM) probe and the gold-coated tip.
(a) Schematic of the experimental set-up, in which a gold- coated SThM probe (cross-sectional view) is brought into close proximity of a heated gold substrate. The tunneling current across the nanogap is monitored by applying dc or ac voltages. Simultaneously, the thermoelectric voltage (Vth) generated by the Au-Cr thermocouple is recorded to monitor the temperature of the probe's tip. The diagram on the right shows the thermal resistance network representing the heat flow from the substrate, through the nanogap, to the probe. (b) SEM images showing the top view of a SThM probe. Inset, magnified image of the nano-thermocouple (Nano-T.C.) at the tip of the probe. (c-d) SEM images of the probe and its tip, which has a diameter of ~300 nm.

In the first set of experiments a probe, thoroughly cleaned in acetone to remove potential contaminants and residue from fabrication and handling, was loaded into a UHV scanning probe microscope along with a template stripped Au surface (within a few minutes after stripping the

sample) to study near-field radiative heat transfer. In this experiment the sample temperature T_{sample} was chosen to be 343 K, while the probe was held at a lower temperature (T_{probe} = 303 K), thus establishing a temperature differential (ΔT) of 40 K. This temperature differential was chosen to be significantly smaller than the average temperature of the sample and the probe $(T_{sample} + T_{probe})/2$ to ensure that experiments were conducted in the linear response regime. We note that applying larger temperature differentials (e.g. 100 K) does not dramatically affect the estimated conductances as discussed in more detail below (see Fig. 6.5b). Figure 6.2 shows the measured radiative thermal conductance (pink) and tunneling current (blue) from 15 independent measurements as the gap-size between the probe and the sample is reduced at a constant speed (~0.1 nm/s). The solid lines represent the mean value of the data whereas the transparent color represents the standard deviation. It can be seen from the data that the thermal conductance begins to increase monotonically as the gap-size is reduced below ~2.5 nm and reaches a value as large as ~30 nW/K at the smallest gap-size. This behavior is similar to what was reported in recent papers[232, 237]. As a comparison, the measured heat flux in these previous works begins to monotonically increase from ~5 nm, and the thermal conductance at the smallest gap is reported to be ~3 nW/K—a value smaller than that observed by us, possibly due to the smaller tip size of the probes employed (our probe's diameter is ~5 times larger). This experimentally observed conductance (30 nW/K) is almost three orders of magnitude larger than that predicted by calculations performed using fluctuational electrodynamics (see Fig. 6.5, calculation details explained later).

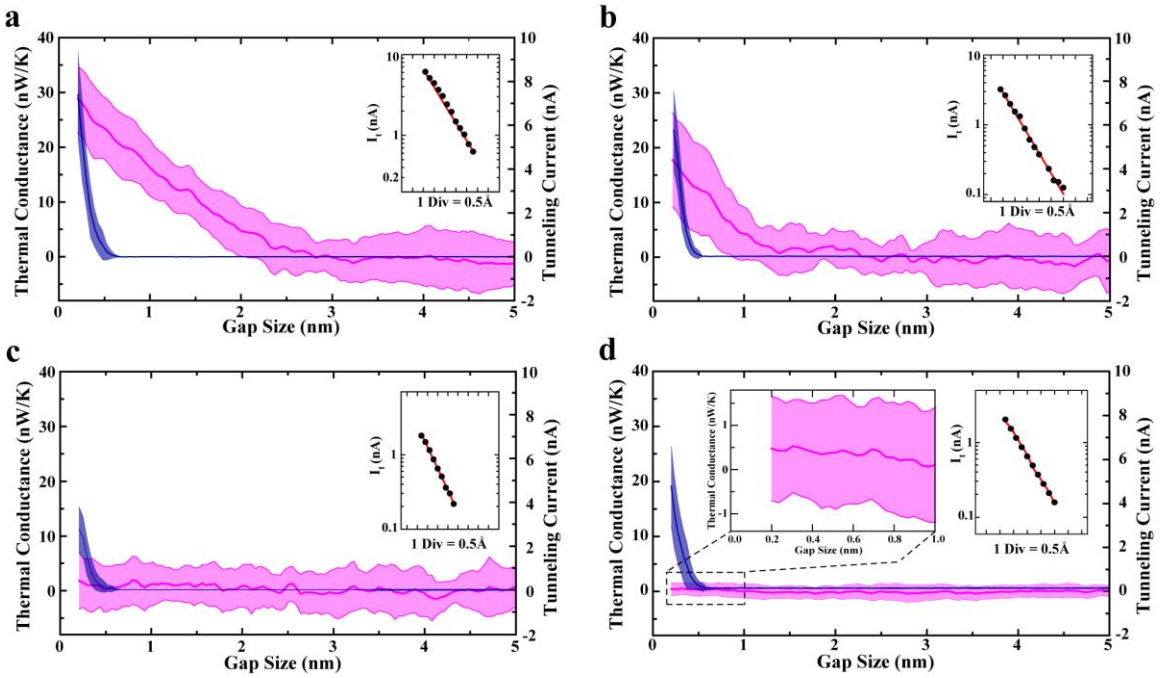

Figure 6.2: Measured thermal conductance (pink) and tunneling current (blue) between the gold-coated SThM probe and planar gold sample.
Each curve is averaged over 15 repeated measurements. The shaded region represents the standard deviation. The first three panels show representative experimental results from (a) organic solvent cleaned, (b) oxygen plasma cleaned, and (c) repeated oxygen plasma cleaned scenarios. The gold sample is heated while the probe is maintained at a lower temperature to create a temperature difference $\Delta T = 40$ K. Figure (d) shows the measurement results obtained in experiments where a large temperature differential (ΔT) of 130 K was applied. The thermal conductance data in the sub-nanometer region is shown on an expanded scale in the inset to facilitate visualization. Further, the measured tunneling currents vs. displacement are shown in insets for each of the plots and were used in the analysis of the apparent tunneling barrier , the estimated values of which are 1.05, 1.61, 1.71, and 1.92 eV for figures (a)–(d), respectively.

A possible explanation for the large thermal conductance observed in our experiments is the presence of contaminants that may bridge the tip and the sample before the Au on the tip contacts the Au atoms on the sample, thus providing a pathway for heat transfer via conduction. One may hypothesize that such contamination arises from imperfect removal of any molecules bound to the SThM probe during fabrication, contamination during storage and handling, or due to re-contamination of the tip due to diffusion of molecules present elsewhere on the sample or the tip. Given the small size of the SThM tip (diameter of ~300 nm), a direct characterization of its surface is challenging. Therefore, as a first test of our hypothesis that the sample is

contaminated we analyzed the tunneling current curves following a procedure reported elsewhere[202, 261]. Specifically, we fitted the tunneling current data to a tunneling barrier model to obtain the apparent barrier height (φ_{ap}, in eV) from $\rho_{ap} = \left(\frac{1}{1.025}\frac{d(\ln(I_t))}{dz}\right)^2$, where z is the gap-size in Å and I_t is the tunneling current. From the slope of the tunneling current shown in Fig. 6.2a we obtained a value for φ_{ap} of 1.05 eV. This low barrier height is in contrast to the large (~4.7 ± 1 eV) barrier heights[202] expected for ultra clean Au surfaces, and is indeed consistent with the presence of surface contamination[202, 261]. We note that careful analysis of tunneling current curves presented in previous works[237] also suggested low barrier heights (<1 eV) indicating the possibility of contamination.

In order to explore the feasibility of reducing/eliminating surface contamination effects we employed oxygen-plasma based techniques[262] for cleaning the probe (see Methods). Subsequently, we repeated the conductance measurements following an approach similar to that used in obtaining the data in Fig. 6.2a. The data obtained from this experiment is shown in Fig. 6.2b, in which we can clearly see that the thermal conductance is reduced by a factor of 2 and the thermal conductance starts to monotonically increase from a smaller gap-size of ~1 nm. Since this measurement employed the same probe, sample, and experimental procedures as that in Fig. 6.2a, we concluded that surface contaminants were the most probable reason for the observed spurious thermal conductances. This conclusion is further supported by our analysis of the tunneling current data (obtained from the cleaned sample and tip), which yielded a φ_{ap} of 1.61 eV: a value significantly higher than that obtained for the data in Fig. 6.2a.

Upon succeeding in attenuating the effect of potential surface contaminants we repeated the oxygen-plasma cleaning process (three times for both the probe and the sample) to

understand if the cleanliness can be further improved. Data obtained from experiments performed after these additional cleaning steps are shown in Fig. 6.2c. It can be seen that there is no discernible increase of thermal conductance until the contact of the probe and the sample is made. Further, the apparent barrier height was further increased to ~1.71 eV reflecting the increased cleanliness of the surface. The noise floor in thermal conductance (RMS value ~3 nW/K) measurements has significant contributions from low frequency noise associated with temperature drift of the ambient and from Johnson noise of the thermocouple, whose electrical resistance is ~5 kΩ. The data in Fig. 6.2c (corresponding to the solid line) shows that the thermal conductance is less than 2.5 nW/K for sub-nanometer gaps. To get a more refined estimate of this conductance we increased the temperature differential to 130 K by increasing the sample temperature to 445 K (the probe temperature increases to 315 K). Such increased temperature differentials resulted in an enhancement of the signal to noise ratio as the noise remains unchanged whereas the signal increases, to first order, proportionally to the applied temperature differential. This larger temperature differential results in deviations from the linear response regime, however, the expected deviations in the thermal conductance are small (see inset Fig. 6.5b). Further, application of this larger temperature differential enables a more direct comparison with past experiments[232, 236, 237] where similarly large temperature differentials were applied. Data obtained from these experiments (Fig. 6.2d) show a significantly reduced noise floor and establish an upper bound on the maximum possible thermal conductance at the smallest gaps (~2 Å) ~0.5 nW/K—a value much smaller than that reported in previous works[236, 237].

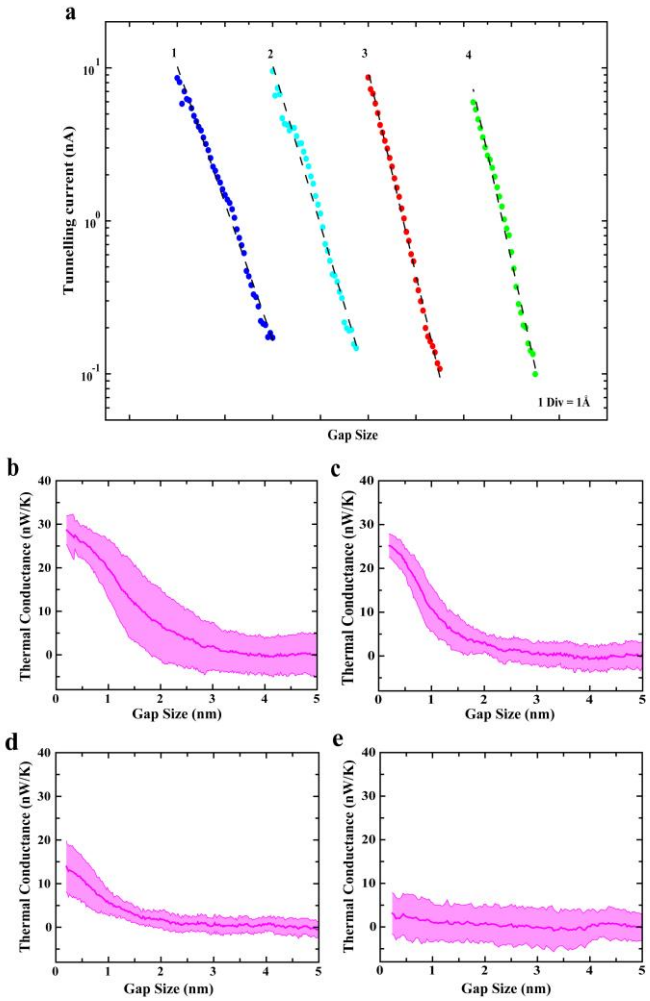

Figure 6.3: Apparent tunneling barrier and thermal conductance for probes cleaned by controllably crashing a probe into the substrate.
Solvent and plasma-cleaned probes were used in experiments where the probe was intentionally indented into the substrate by a few nanometers to create a direct point contact between the probe and the sample. This procedure resulted in gaps that featured larger apparent tunneling barrier heights. Specifically, was found from tunneling current vs. displacement curves (panel a) to monotonically increase from 1 eV (dark blue dots, for the probe in initial condition) to 1.37 eV to 2.24 eV to 2.46 eV in consecutive experiments where the tip was displaced into the substrate by 1 nm (light blue dots), 2 nm (red dots) and 5 nm (green dots), respectively. The thermal conductance corresponding to each of these scenarios is shown in Figs. b-e. It can be seen that the apparent near-field thermal conductance is systematically reduced as the apparent tunneling barrier height increases.

In addition to the approaches described above, we further explored the feasibility of cleaning the tip and the sample locally by "controlled crashing" of the tip into the sample. This *in situ* cleaning method has been reported previously to be effective in locally cleaning surfaces[202, 261, 263]. Data obtained from a probe that was first cleaned with liquid solvents and oxygen plasma

procedures (cf to Fig. 6.2) and subsequently pushed or indented into the gold substrate by increasing distances of a few nanometers are shown in Fig. 6.3. Specifically, the blue line in Fig. 6.3a shows the gap-dependent tunnelling current, which features an apparent tunnelling barrier of ~1 eV. Further, the corresponding thermal measurement (Fig. 6.3b) reveals large thermal conductances (~20 – 30 nW/K) in gaps below 1 nm that are consistent with the presence of contamination. Next, we gently indented the probe into the planar Au sample by displacing the tip by an additional 1 nm after an electrical conductance of $1G_0$ ($G_0 = 2e^2/h$, the quantum of electrical conductance), corresponding to a single-atom contact, was established. We expected that such a process would create a locally clean sample. Measurements performed after one such indent and withdraw cycle show that the apparent barrier height had increased to ~1.34 eV and the measured thermal conductance decreased modestly to a value of ~25 nW/K. In order to explore the feasibility of achieving greater cleanliness we performed a slightly more aggressive indentation, i.e. displacement of the tip into the sample substrate by 2 nm after making atomic contact (signalled by an electrical conductance of $1G_0$). Subsequent measurements revealed a much larger apparent barrier height ~2.24 eV. However, the spurious thermal conductance was not completely eliminated, resulting in a lowered thermal conductance of ~10 nW/K. This incomplete cleaning is possibly due to the local nature of the cleaning procedure, which results in removal of contaminants only directly under the tip while leaving the surrounding region unaffected. Finally, we displaced the probe by 5 nm into the sample after making atomic contact, which enabled us to attenuate the thermal conductance to negligible levels of ~2 nW/K (Fig. 6.3c) as limited by the noise floor of our technique (the applied temperature differential was 40 K). In this case the apparent barrier height was found to increase to 2.46 eV. These experiments

show that the effect of contamination can be systematically reduced by locally crashing the tip into the sample.

Finally, we performed one more set of experiments where we explored how robust the cleaning procedures were and if the tip and the sample can be potentially re-contaminated. Specifically, we placed the probe at a known separation from the sample by choosing a tunnelling current of ~1 nA (50 mV DC bias, corresponding to a gap-size of ~5 – 7 Å) and continuously measured the thermal conductance of the gap as a function of time. For a probe and sample that were presumably as clean as those used in obtaining the data shown in Fig. 6.2a (they were subjected to the same cleaning procedures) the thermal conductance was relatively unaffected (see Fig. 6.4a) over a long period of time (~1 hour). Similar measurements were also performed on probes and samples that are expected to have cleanliness similar to those used in obtaining the data shown in Figs. 6.2b and 6.2c. The data obtained from these experiments are shown in Figs. 6.4b and 6.4c, respectively. It can be seen that the thermal conductance in these experiments is also relatively stable. The low frequency noise seen in these plots is most probably due to ambient temperature drift. Taken together, these data suggest that the probability of contamination is relatively low for well-cleaned probes in an ultra-high vacuum environment.

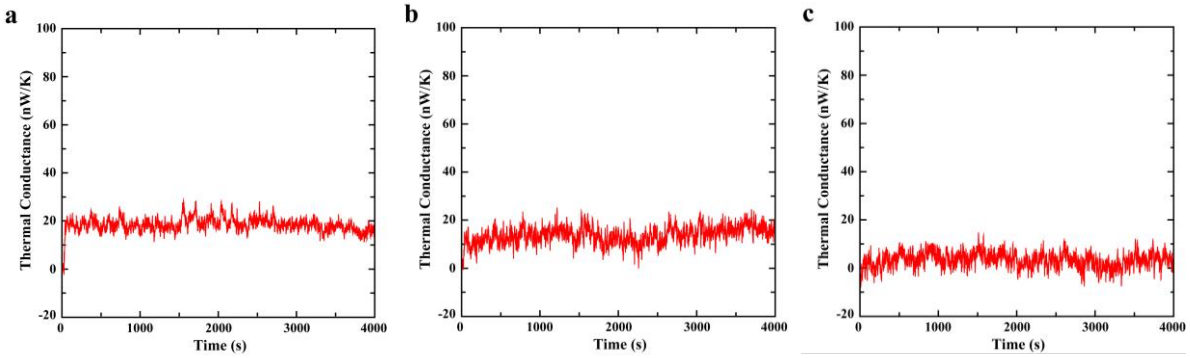

Figure 6.4: Measured time-dependent apparent thermal conductance for probe subjected to different cleaning procedures.

(a) – (c) Thermal conductance as a function of time for probes subjected to the cleaning procedures as described for Figs. 6.2a – 6.2c, respectively.

In order to determine whether our experimental results can be explained in the light of established NFRHT theories, we used the fluctuating-surface-current formulation of the radiative heat transfer problem[239, 264]. In practice, we made use of a combination of this formulation with the well-established boundary element method (BEM), as implemented in the SCUFF-EM solver [265]. This combination allows us to describe the radiative heat transfer between bodies of arbitrary shape and provides numerically exact results within the framework of fluctuational electrodynamics in the local approximation (in which the dielectric functions of the materials are assumed to depend only on frequency). In particular, this approach was successfully employed[231] by us to describe the NFRHT between compliant atomic force microscope based scanning thermal probes and substrates coated with metals/dielectrics for separations (or gaps) down to 2-3 nm. In order to simulate our experiments as accurately as possible, we considered tip-substrate geometries like the one shown in Fig. 6.5a. Here, we followed the SEM images of our thermal probes and modelled the gold tip with an irregular conical shape that ends in a hemispherical cap of radius 150 nm, while the substrate was modelled by a thick disk whose dimensions have been carefully chosen to avoid any finite-size effects. Following the approach taken in our previous work[231], we also simulated the roughness of our gold tips by including a random Gaussian noise in the profile of the tip apex (inset of Fig. 6.5a). To be precise, the maximum protrusion height of our roughness is 10 nm and the correlation length between protrusions is 17 nm. To evaluate the impact of the roughness in the radiative heat transfer in our system, we simulated an ensemble of 15 tips with different roughness profiles. We emphasize that the only input information in our simulations, apart from the geometry, is the frequency-dependent dielectric function of gold that we obtained from published work[266].

The results of the simulations for the total radiative thermal conductance between the gold tip and the gold substrate are shown in Fig. 6.5b for gap sizes from 1 Å to 5 nm. This figure displays the results for an ideal tip (no roughness) and for 15 tips featuring roughness (both mean value and standard deviation). It can be seen that the tip roughness has no major impact on the thermal conductance. More importantly, the thermal conductance for the smallest gap size is of the order of 30 pW/K, which is approximately 30 times smaller than the noise floor (~900 pW/K, RMS) in our large bias measurements (see Fig. 6.2d). This supports our conclusion that the large signals observed in our experiments before the cleaning procedure cannot be explained in terms of radiative heat transfer. For completeness, we note that the slow decay of the thermal conductance with the gap size (Fig. 6.5b) is characteristic of metals and it is due to the fact that radiative heat transfer is dominated by evanescent (in the vacuum gap) TE modes resulting from total internal reflection, the contribution of which saturates at single-nanometer gaps[231, 254]. On the other hand, the role of nonlocal effects in the dielectric function of gold have been studied[254] in the context of radiative heat transfer and have been shown to be very small for the gap sizes explored in our work.

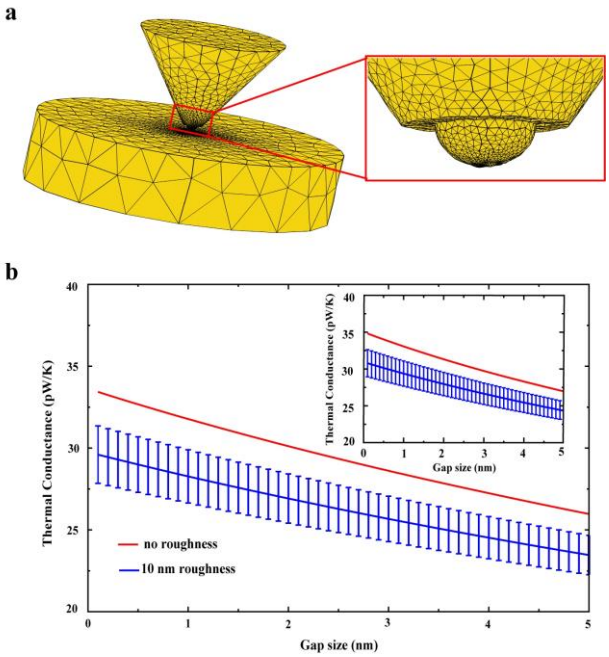

Figure 6.5: Computational prediction of the radiative thermal conductance.
(a) Tip-substrate geometries employed in our numerical simulations. Following the SEM images of our thermal probes, the tip was modelled as an irregular cone that ends in a hemisphere, while the substrate was modelled as a thick disk. The height of the cone was chosen to be 3 μm and the radius of its base was 1.9 μm. The radius of the disk is 4 μm and its thickness 2 μm. The solid black lines depict the triangular mesh employed in the BEM calculations. The right inset shows a blow-up of the tip apex region. (b) The computed total radiative thermal conductance as a function of the gap-size between the Au tip and substrate. The red solid line corresponds to the ideal tip (no roughness) and the blue line to the average obtained with 15 different tip with stochastically chosen roughness profiles (RMS roughness ~10 nm), while the error bars indicate the standard deviation. The tip diameter in these calculations is 300 nm, while the temperature of the probe and substrate were chosen to be 303 K and 343 K, respectively. Inset, similar to the main panel except that the probe and substrate temperatures are 315 K and 445 K, respectively.

6.4 Conclusion

To summarize, we report measurements of extreme near-field radiative heat transfer at gap-sizes ranging from a few Å to 5 nm. Our results suggest that observations of large deviations from the predictions of fluctuational electrodynamics are due to surface contamination effects. We also demonstrate, from measurements of apparent tunneling barrier heights, that such deviations can be systematically attenuated by carefully cleaning the surfaces. In contrast to previous studies[232, 236, 237], which observed both conductances as large as 3 nW/K (three to four orders larger than the predictions of fluctuational electrodynamics) and conductance

enhancements beginning at gap-sizes as large as 4 to 5 nm, our results (Fig. 6.2d) suggest that deviations, if any, are in the sub-nanometer regime and are much smaller in magnitude (~0.5 nW/K). These sub-nanometer level deviations could potentially result from monolayer level contaminations that may still be present on our surfaces and cannot be detected from our probes. These results taken along with those of our previous work[231] confirm that there are no observable differences between the predictions of fluctuational electrodynamics and those from experiments even at gap-sizes as small as a nanometer. Further, this work highlights the need for development of probes, e.g. based on the approach leveraged in our previous work[231], that can accurately resolve the small heat fluxes expected for Au surfaces at sub-nanometer gaps while independently quantifying the interaction forces with the substrate. Such approaches are crucial for drawing careful conclusions about near-field radiation. The insights obtained from this study will be critical for the development of high sensitive near-field measurements, and future technologies that leverage nanoscale radiative heat transfer.

6.5 Methods and Supporting Information

6.5.1 Determination of gap-size

In our experiments the SThM probe was displaced towards the substrate at a constant speed (0.1 nm/s), by a piezoelectric actuator, starting from an initial distance of ~5 nm until "contact" was established with the substrate. We define "contact" as the situation where a tunneling gap resistance $R = 0.1$ MΩ is reached, which, based on the measured apparent tunneling barrier φ_{ap} (~1 to 3 eV) is estimated to correspond to a gap-size of ~1.3 to 2.3 Å. To account for this separation all data presented in Figs. 6.2 and 6.3 feature a minimum gap of 2 Å.

6.5.2 Fabrication of Scanning Thermal Microscopy Probes

The steps involved in the fabrication of the scanning thermal microscopy (SThM) probes are shown in Fig. 6.6. A brief description of the steps is provide here: (Step 1) The nanofabrication starts with the deposition of a 500 nm thick low-stress low pressure chemical vapor deposition (LPCVD) silicon nitride (SiNx) on a silicon (Si) wafer. (Step 2) An 8 μm thick layer of low temperature silicon oxide (LTO) is deposited on top of the wafer and is annealed at 1000 °C for 1 hour to reduce the residual stress of SiNx and LTO layers. The LTO layer is later etched to create the sharp probe tip. Subsequently, a 100 nm thick chromium (Cr) layer is sputtered and lithographically patterned by wet etching. This Cr pattern is critical to create the LTO probe tip. (Step 3) The probe tip is created by wet etching in buffered HF (HF : NH_4F = 1 : 5), which takes ~100 minutes. In order to create a sharp tip, the etching status is frequently monitored. (Step 4) A gold (Au) line (Cr/Au: 5/90 nm thick) is lithographically defined by sputtering and wet etching. This Au line forms the first metal layer of the nanoscale Au-Cr thermocouple. Subsequently, a 70 nm thick layer of plasma enhanced chemical vapor deposition (PECVD) SiNx is deposited for the electrical insulation. (Step 5) A layer of Shipley Microposit S1827 photoresist (6 μm thick) is deposited on the wafer, and the photoresist and PECVD SiNx is slowly plasma-etched until a very small portion of Au is extruded at the tip apex. (Step 6) A Cr line (90 nm thick) is lithographically defined by sputtering and wet etching. This Cr line together with the very small Au extrusion establishes a nanoscale Au/Cr thermocouple at the tip apex. (Step 7) A 70 nm thick PECVD SiNx is deposited for the electrical insulation. Subsequently, a Au line (Cr/Au: 5/90nm thick) is lithographically defined by sputtering and wet etching. Note that this Au line is the outermost metal layer of the probe. (Step 8) Finally, the SThM probes are released by deep reactive ion etching (DRIE) to create the desired stiff SThM probes.

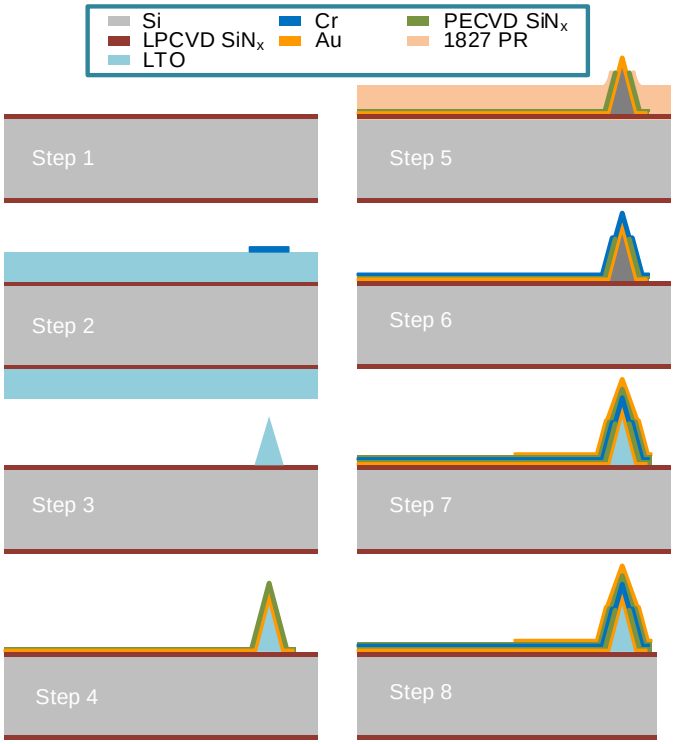

Figure 6.6: The steps involved in the fabrication of the SThM probes.

6.5.3 Estimation of the Stiffness of the Scanning Probes via Modelling

The stiffness of the probes was estimated by employing a finite element analysis using COMSOL^{TM}. In this computation, we included a 500 μm thick silicon (Si) block, which is the cantilevered portion of our probe into which a 8 μm tall tip made of silicon oxide (SiO_2) is added as shown in Fig. 6.7. The values of Young's modulus (E) and Poisson's ratio (ν) assumed in these calculations are as follows: Si (E = 170 GPa, ν = 0.28), SiO_2 (E = 70 GPa, ν = 0.17). Further, in order to estimate the stiffness of the probe, the following boundary conditions were assigned: a 100 nN of either a normal or a shear force was applied at the apex of SiO_2 tip, while the opposite end of the Si block was fixed (see Fig. 6.7). Note that we evaluated three sets of deflections where the normal deflection (i.e deflection in the z-direction, see Fig. 6.7a) is determined by the cantilever stiffness, whereas the shear deflections (x- or y- direction) are related to the transverse stiffness of the tip. From the computed deflections, the stiffness of our

probe was estimated to be ~10700 N/m in the normal direction and ~5300 N/m in the lateral directions (x and y directions labeled in Fig. 6.7).

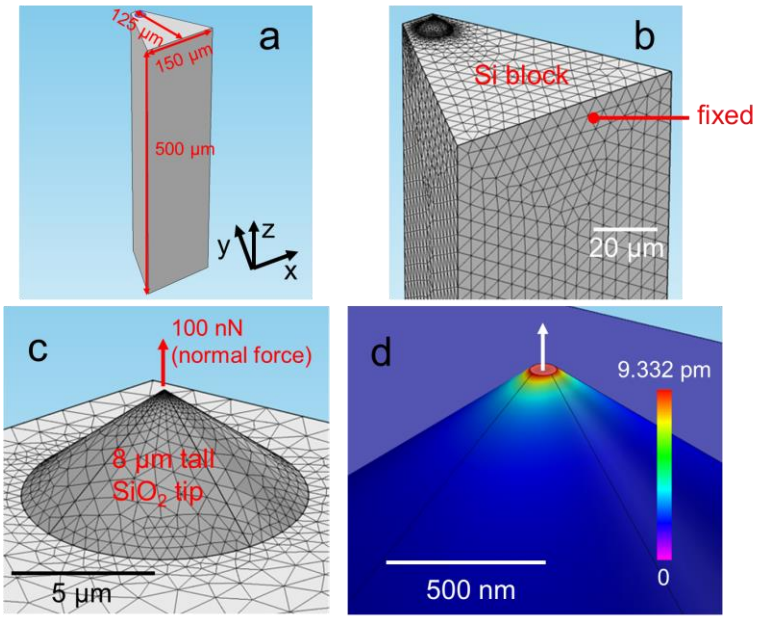

Figure 6.7: Finite element analysis of the stiffness of scanning thermal probes that comprise of a 500 µm thick silicon block and a 8 µm tall silicon oxide tip.
(a) schematic of the probe. (b) & (c) describe the finite element mesh employed in the calculations. (d) presents the calculated deflection of the probe in the z-direction upon application of a 100 nN of normal force.

6.5.4 Characterization of the Thermal Resistance of Scanning probes

To characterize the thermal resistance of the SThM probe, we follow a procedure developed by some of us recently. The first step in this process is to determine the heat flux Q into the probe when it contacts a hot surface and measure the temperature increase of the probe (ΔT^{P}) via the embedded thermocouple. The resistance of the probe can thus be found to be $R_{probe} = \Delta T^{P} / Q$. To accomplish this procedure, a suspended calorimeter with an integrated Pt resistance heater-thermometer was employed. If an AC current at a frequency ω, and amplitude I_{ω} is supplied to the Pt heater, temperature oscillations at a frequency 2ω and amplitude $T_{2\omega}$ are induced. When the SThM probe was placed in contact with the heated calorimeter (see inset Fig.

S3), an additional conduction path (via the probe) is established resulting in a heat current through the probe. This additional conduction path also reduces the amplitude of temperature oscillations by $\Delta T_{2\omega}$. The heat flux into the probe ($Q_{2\omega}$) can be readily estimated from $Q_{2\omega} = G_{sus} \Delta T_{2\omega}$ where G_{sus} is the thermal conductance of the suspended calorimeter. By measuring the temperature increase of the probe ($\Delta T_{2\omega}{}^{P}$) we obtain the probe resistance to be $R_{probe} = \Delta T_{2\omega}^{p} / Q_{2\omega}$. In Fig. 6.8, the measured temperature increase of the probe at frequency 2ω is plotted against the heat input into the probe. The slope of the plot is gives the probe resistance which we determined to be $R_{Probe} = 9 \times 10^{4}\text{K/W}$.

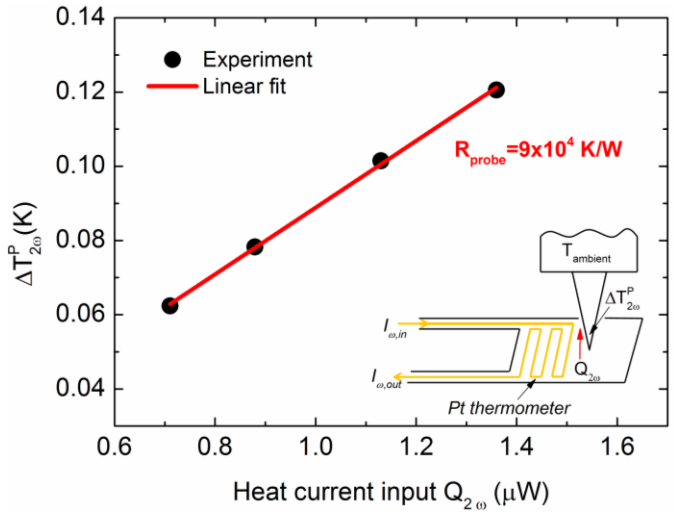

Figure 6.8: Measured amplitude of temperature oscillations of the probe as a function of the magnitude of the heat current input to the tip.
The slope of the line is used to determine the thermal resistance of the probe. Inset shows a schematic of the experiment where the scanning probe is placed in contact with the suspended calorimeter.

6.5.5 Characterization of the Temperature Drift of the Ambient and the Noise Spectrum

The thermoelectric voltage output from the thermocouple embedded in the SThM probe is characterized by noise contributions mainly from Johnson noise and low frequency temperature drift. This noise was quantified by experimentally determining the power spectral

density (Fig. 6.9) of the voltage output from the thermocouple using a SR 760 spectrum analyzer (Stanford Research Systems).

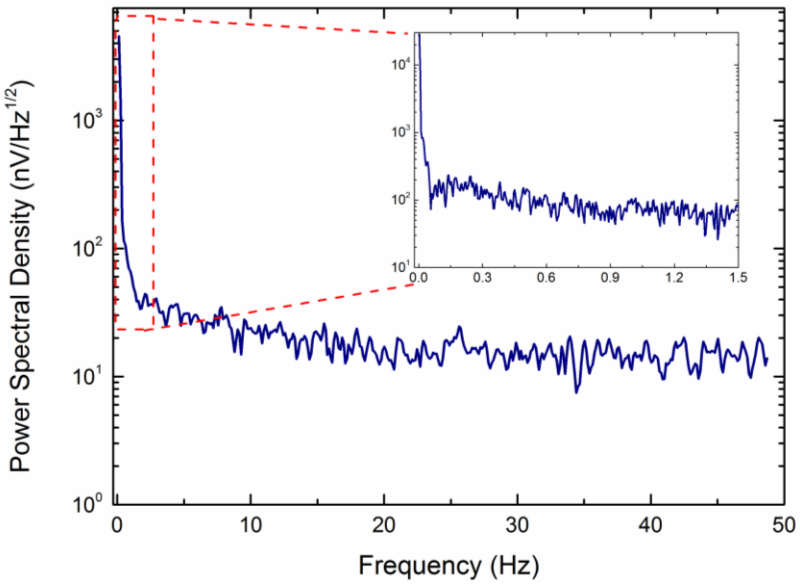

Figure 6.9: Noise characterization of thermoelectric voltage output from the scanning probes.
Measured power spectral density (PSD) of the thermoelectric voltage output from the probe for the frequency span from 0 to 50 Hz. The inset shows the PSD for the low frequency (0 to 1.5 Hz) region.

It can be seen that the measured noise power spectral density increases rapidly at low frequencies. The measured PSD at high frequencies agrees reasonably well with the expected Johnson noise (PSD [V/Hz$^{1/2}$]= $\sqrt{4k_BTR}$) and is estimated to be ~10 nV/Hz$^{1/2}$ for our scanning probes whose thermocouple resistance is ~5 kΩ. At lower frequencies there are significant contributions due to ambient temperature drift. To demonstrate this point, we measured the fluctuation of thermal conductance for a period of ~1 hour when the scanning probe was placed at a constant distance of ~100 nm from the substrate (Fig. 6.10). Under these conditions the thermal conductance between the tip and the sample is expected to be invariant with time. It can be seen that there is an apparent thermal conductance change of ~15 nW/K (peak-to-peak), similar to the noise level shown in Fig. 6.4 of the main manuscript which is likely due to

temperature drift of a few 10s of mK. Furthermore, by comparing the trend of the measured signal in Fig. 6.10 and Fig. 6.4, we can see that the low frequency noise present in the data of Fig. 6.4 is most likely due to the temperature drift of the ambient.

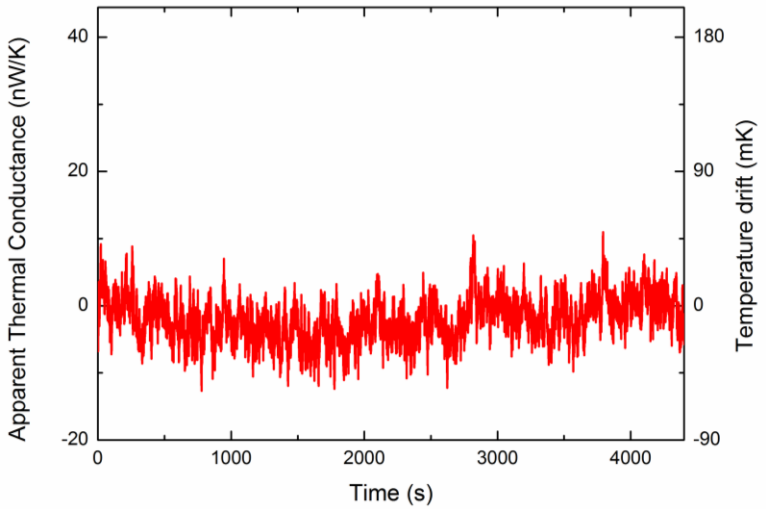

Figure 6.10: Fluctuations in temperature and radiative thermal conductances.
When the temperature of the scanning probe or the ambient temperature drifts, the thermoelectric voltage output from the scanning probe fluctuates. This manifests itself as a fluctuating, apparent thermal conductance. Data shown above was obtained from an experiment where the probe and the sample were separated by 100 nm and a temperature differential of 40 K was applied. The measured fluctuations in the temperature of the thermocouple (and the corresponding) radiative thermal conductance are shown.

Bibliography

1. Cui, L., Miao, R., Jiang, C., Meyhofer, E., Reddy, P. Perspective: Thermal and thermoelectric transport in molecular junctions. *J Chem Phys* **146,** 092201 (2017).

2. Aviram, A., Ratner, M. A. Molecular Rectifiers. *Chem Phys Lett* **29,** 277-283 (1974).

3. Nitzan, A., Ratner, M. A. Electron transport in molecular wire junctions. *Science* **300,** 1384-1389 (2003).

4. Tao, N. J. Electron transport in molecular junctions. *Nature Nanotechnology* **1,** 173-181 (2006).

5. Aradhya, S. V., Venkataraman, L. Single-molecule junctions beyond electronic transport. *Nature Nanotechnology* **8,** 399-410 (2013).

6. Xiang, D., Wang, X. L., Jia, C. C., Lee, T., Guo, X. F. Molecular-Scale Electronics: From Concept to Function. *Chem Rev* **116,** 4318-4440 (2016).

7. Chen, F., Hihath, J., Huang, Z., Li, X., Tao, N. J. Measurement of single-molecule conductance. *Annu Rev Phys Chem* **58,** 535-564 (2007).

8. Sun, L., Diaz-Fernandez, Y. A., Gschneidtner, T. A., Westerlund, F., Lara-Avila, S., *et al.* Single-molecule electronics: from chemical design to functional devices. *Chem Soc Rev* **43,** 7378-7411 (2014).

9. Nichols, R. J., Higgins, S. J. Single-Molecule Electronics: Chemical and Analytical Perspectives. *Annu Rev Anal Chem* **8,** 389-417 (2015).

10. Galperin, M., Ratner, M. A., Nitzan, A., Troisi, A. Nuclear coupling and polarization in molecular transport junctions: Beyond tunneling to function. *Science* **319,** 1056-1060 (2008).

11. Galperin, M., Ratner, M. A., Nitzan, A. Molecular transport junctions: vibrational effects. *J Phys-Condens Mat* **19,** 103201 (2007).

12. Bergfield, J. P., Ratner, M. A. Forty years of molecular electronics: Non-equilibrium heat and charge transport at the nanoscale. *Phys Status Solidi B* **250,** 2249-2266 (2013).

13. Lee, W., Song, B., Reddy, P. Measurement of thermoelectric and thermal transport properties of single-molecule junctions. *Annu Rev Heat Transfer* **16,** 259-286 (2013).

14. Rincon-Garcia, L., Evangeli, C., Rubio-Bollinger, G., Agrait, N. Thermopower measurements in molecular junctions. *Chem Soc Rev* **45,** 4285-4306 (2016).

15. Segal, D., Agarwalla, B. K. Vibrational Heat Transport in Molecular Junctions. *Annu Rev Phys Chem* **67,** 185-209 (2016).

16. Malen, J. A., Yee, S. K., Majumdar, A., Segalman, R. A. Fundamentals of energy transport, energy conversion, and thermal properties in organic-inorganic heterojunctions. *Chem Phys Lett* **491,** 109-122 (2010).

17. Dubi, Y., Di Ventra, M. Colloquium: Heat flow and thermoelectricity in atomic and molecular junctions. *Rev Mod Phys* **83,** 131-155 (2011).

18. Finch, C. M., García-Suárez, V. M., Lambert, C. J. Giant thermopower and figure of merit in single-molecule devices. *Phys Rev B* **79,** 033405 (2009).

19. Bergfield, J. P., Solis, M. A., Stafford, C. A. Giant thermoelectric effect from transmission supernodes. *Acs Nano* **4,** 5314-5320 (2010).

20. Nakpathomkun, N., Xu, H. Q., Linke, H. Thermoelectric efficiency at maximum power in low-dimensional systems. *Phys Rev B* **82,** 235428 (2010).

21. Vacek, J., Chocholousova, J. V., Stara, I. G., Stary, I., Dubi, Y. Mechanical tuning of conductance and thermopower in helicene molecular junctions. *Nanoscale* **7,** 8793-8802 (2015).

22. Henry, A., Chen, G. High Thermal Conductivity of Single Polyethylene Chains Using Molecular Dynamics Simulations. *Phys Rev Lett* **101,** 235502 (2008).

23. Liu, J., Yang, R. G. Length-dependent thermal conductivity of single extended polymer chains. *Phys Rev B* **86,** 104307 (2012).

24. Landauer, R. Spatial Variation of Currents and Fields Due to Localized Scatterers in Metallic Conduction. *Ibm J Res Dev* **1,** 223-231 (1957).

25. Landauer, R. Conductance Determined by Transmission - Probes and Quantized Constriction Resistance. *J Phys-Condens Mat* **1,** 8099-8110 (1989).

26. Imry, Y. *Introduction to mesoscopic physics*. Oxford University Press: New York, 1997.

27. Datta, S. *Quantum transport : atom to transistor*. Cambridge University Press: Cambridge, UK ; New York, 2005.

28. Butcher, P. N. Thermal and Electrical Transport Formalism for Electronic Microstructures with Many Terminals. *J Phys-Condens Mat* **2,** 4869-4878 (1990).

29. Paulsson, M., Datta, S. Thermoelectric effect in molecular electronics. *Phys Rev B* **67,** 241403 (2003).

30. Esfarjani, K., Zebarjadi, M., Kawazoe, Y. Thermoelectric properties of a nanocontact made of two-capped single-wall carbon nanotubes calculated within the tight-binding approximation. *Phys Rev B* **73,** 085406 (2006).

31. Sivan, U., Imry, Y. Multichannel Landauer Formula for Thermoelectric Transport with Application to Thermopower near the Mobility Edge. *Phys Rev B* **33,** 551-558 (1986).

32. Lake, R., Datta, S. Energy-Balance and Heat-Exchange in Mesoscopic Systems. *Phys Rev B* **46,** 4757-4763 (1992).

33. Ke, S. H., Yang, M., Curtarolo, S., Baranger, H. U. Thermopower of Molecular Junctions: An ab Initio Study. *Nano Lett* **9,** 1011-1014 (2009).

34. Leijnse, M., Wegewijs, M. R., Flensberg, K. Nonlinear thermoelectric properties of molecular junctions with vibrational coupling. *Phys Rev B* **82,** 045412 (2010).

35. Claughton, N. R., Lambert, C. J. Thermoelectric properties of mesoscopic superconductors. *Phys Rev B* **53,** 6605-6612 (1996).

36. Huser, F., Solomon, G. C. From Chemistry to Functionality: Trends for the Length Dependence of the Thermopower in Molecular Junctions. *J Phys Chem C* **119,** 14056-14062 (2015).

37. Solomon, G. C. Molecular Thermopower Feeling the Squeeze. *Nat Mater* **15,** 254-255 (2016).

38. Burkle, M., Zotti, L. A., Viljas, J. K., Vonlanthen, D., Mishchenko, A., *et al.* Ab initio study of the thermopower of biphenyl-based single-molecule junctions. *Phys Rev B* **86,** 115304 (2012).

39. Zotti, L. A., Burkle, M., Pauly, F., Lee, W., Kim, K., *et al.* Heat dissipation and its relation to thermopower in single-molecule junctions. *New J Phys* **16,** 015004 (2014).

40. Pauly, F., Viljas, J. K., Burkle, M., Dreher, M., Nielaba, P., *et al.* Molecular dynamics study of the thermopower of Ag, Au, and Pt nanocontacts. *Phys Rev B* **84,** 195420 (2011).

41. Burkle, M., Hellmuth, T. J., Pauly, F., Asai, Y. First-principles calculation of the thermoelectric figure of merit for [2,2]paracyclophane-based single-molecule junctions. *Phys Rev B* **91,** 165419 (2015).

42. Bergfield, J. P., Stafford, C. A. Thermoelectric Signatures of Coherent Transport in Single-Molecule Heterojunctions. *Nano Lett* **9,** 3072-3076 (2009).

43. Wang, Z. H., Carter, J. A., Lagutchev, A., Koh, Y. K., Seong, N. H., *et al.* Ultrafast flash thermal conductance of molecular chains. *Science* **317,** 787-790 (2007).

44. Mahan, G. D., Sofo, J. O. The best thermoelectric. *Proc Natl Acad Sci USA* **93,** 7436-7439 (1996).

45. Karlström, O., Linke, H., Karlström, G., Wacker, A. Increasing thermoelectric performance using coherent transport. *Phys Rev B* **84,** 113415 (2011).

46. Nozaki, D., Sevincli, H., Li, W., Gutierrez, R., Cuniberti, G. Engineering the figure of merit and thermopower in single-molecule devices connected to semiconducting electrodes. *Phys Rev B* **81,** 235406 (2010).

47. Miroshnichenko, A. E., Flach, S., Kivshar, Y. S. Fano resonances in nanoscale structures. *Rev Mod Phys* **82,** 2257-2298 (2010).

48. Bohm, D. *Quantum theory*. Prentice-Hall: New York, 1951.

49. Lambert, C. J. Basic concepts of quantum interference and electron transport in single-molecule electronics. *Chemical Society Reviews* **44,** 875-888 (2015).

50. Bernien, M., Wiedemann, D., Hermanns, C. F., Kruger, A., Rolf, D., *et al.* Spin Crossover in a Vacuum-Deposited Submonolayer of a Molecular Iron(II) Complex. *J Phys Chem Lett* **3,** 3431-3434 (2012).

51. Warner, B., Oberg, J. C., Gill, T. G., El Hallak, F., Hirjibehedin, C. F., *et al.* Temperature- and Light-Induced Spin Crossover Observed by X-ray Spectroscopy on Isolated Fe(II) Complexes on Gold. *J Phys Chem Lett* **4,** 1546-1552 (2013).

52. Aravena, D., Ruiz, E. Coherent Transport through Spin-Crossover Single Molecules. *J Am Chem Soc* **134,** 777-779 (2012).

53. Ghosh, D., Parida, P., Pati, S. K. Spin-crossover molecule based thermoelectric junction. *Appl Phys Lett* **106,** 193105 (2015).

54. Whitney, R. S. Most Efficient Quantum Thermoelectric at Finite Power Output. *Phys Rev Lett* **112,** 130601 (2014).

55. Whitney, R. S. Finding the quantum thermoelectric with maximal efficiency and minimal entropy production at given power output. *Phys Rev B* **91,** 115425 (2015).

56. Lambert, C. J., Sadeghi, H., Al-Galiby, Q. H. Quantum-interference-enhanced thermoelectricity in single molecules and molecular films. *Cr Phys* **17,** 1084-1095 (2016).

57. Garcia-Suarez, V. M., Lambert, C. J., Manrique, D. Z., Wandlowski, T. Redox control of thermopower and figure of merit in phase-coherent molecular wires. *Nanotechnology* **25,** (2014).

58. Al-Galiby, Q. H., Sadeghi, H., Algharagholy, L. A., Grace, I., Lambert, C. Tuning the thermoelectric properties of metallo-porphyrins. *Nanoscale* **8,** 2428-2433 (2016).

59. Sadeghi, H., Sangtarash, S., Lambert, C. J. Electron and heat transport in porphyrin-based single-molecule transistors with electro-burnt graphene electrodes. *Beilstein J Nanotech* **6,** 1413-1420 (2015).

60. Lee, W., Reddy, P. Creation of stable molecular junctions with a custom-designed scanning tunneling microscope. *Nanotechnology* **22,** 485703 (2011).

61. Reddy, P., Jang, S. Y., Segalman, R. A., Majumdar, A. Thermoelectricity in molecular junctions. *Science* **315,** 1568-1571 (2007).

62. Xu, B. Q., Tao, N. J. J. Measurement of single-molecule resistance by repeated formation of molecular junctions. *Science* **301,** 1221-1223 (2003).

63. Tan, A., Sadat, S., Reddy, P. Measurement of thermopower and current-voltage characteristics of molecular junctions to identify orbital alignment. *Appl Phys Lett* **96,** 013110 (2010).

64. Tsutsui, M., Morikawa, T., He, Y., Arima, A., Taniguchi, M. High thermopower of mechanically stretched single-molecule junctions. *Sci Rep* **5,** 11519 (2015).

65. Kim, Y., Jeong, W., Kim, K., Lee, W., Reddy, P. Electrostatic control of thermoelectricity in molecular junctions. *Nature Nanotechnology* **9,** 881-885 (2014).

66. Widawsky, J. R., Darancet, P., Neaton, J. B., Venkataraman, L. Simultaneous determination of conductance and thermopower of single molecule junctions. *Nano Lett* **12,** 354-358 (2012).

67. Moreland, J., Ekin, J. W. Electron-Tunneling Experiments Using Nb-Sn Break Junctions. *J Appl Phys* **58,** 3888-3895 (1985).

68. Muller, C. J., Vanruitenbeek, J. M., Dejongh, L. J. Conductance and Supercurrent Discontinuities in Atomic-Scale Metallic Constrictions of Variable Width. *Phys Rev Lett* **69,** 140-143 (1992).

69. Yanson, A. I., Bollinger, G. R., van den Brom, H. E., Agrait, N., van Ruitenbeek, J. M. Formation and manipulation of a metallic wire of single gold atoms. *Nature* **395,** 783-785 (1998).

70. Ludoph, B., van Ruitenbeek, J. M. Thermopower of atomic-size metallic contacts. *Phys Rev B* **59,** 12290-12293 (1999).

71. Smit, R. H., Noat, Y., Untiedt, C., Lang, N. D., van Hemert, M. C., *et al.* Measurement of the conductance of a hydrogen molecule. *Nature* **419,** 906-909 (2002).

72. Agrait, N., Yeyati, A. L., van Ruitenbeek, J. M. Quantum properties of atomic-sized conductors. *Phys Rep* **377,** 81-279 (2003).

73. Smit, R. H. M., Untiedt, C., van Ruitenbeek, J. M. The high-bias stability of monatomic chains. *Nanotechnology* **15,** S472-S478 (2004).

74. Martin, C. A., van Ruitenbeek, J. M., van der Zant, H. S. J. Sandwich-type gated mechanical break junctions. *Nanotechnology* **21,** 265201 (2010).

75. Xiang, D., Jeong, H., Lee, T., Mayer, D. Mechanically Controllable Break Junctions for Molecular Electronics. *Adv Mater* **25,** 4845-4867 (2013).

76. Reed, M. A., Zhou, C., Muller, C. J., Burgin, T. P., Tour, J. M. Conductance of a molecular junction. *Science* **278,** 252-254 (1997).

77. Malen, J. A., Doak, P., Baheti, K., Tilley, T. D., Segalman, R. A., *et al.* Identifying the Length Dependence of Orbital Alignment and Contact Coupling in Molecular Heterojunctions. *Nano Lett* **9,** 1164-1169 (2009).

78. Malen, J. A., Doak, P., Baheti, K., Tilley, T. D., Majumdar, A., *et al.* The Nature of Transport Variations in Molecular Heterojunction Electronics. *Nano Lett* **9,** 3406-3412 (2009).

79. Widawsky, J. R., Chen, W., Vazquez, H., Kim, T., Breslow, R., *et al.* Length-Dependent Thermopower of Highly Conducting Au-C Bonded Single Molecule Junctions. *Nano Lett* **13,** 2889-2894 (2013).

80. Li, Y. Q., Xiang, L. M., Palma, J. L., Asai, Y., Tao, N. J. Thermoelectric effect and its dependence on molecular length and sequence in single DNA molecules. *Nat Commun* **7,** 11294 (2016).

81. Evangeli, C., Gillemot, K., Leary, E., Gonzalez, M. T., Rubio-Bollinger, G., *et al.* Engineering the Thermopower of C-60 Molecular Junctions. *Nano Lett* **13,** 2141-2145 (2013).

82. Macia, E. DNA-based thermoelectric devices: A theoretical prospective. *Phys Rev B* **75,** 035130 (2007).

83. Balachandran, J., Reddy, P., Dunietz, B. D., Gavini, V. End-Group-Induced Charge Transfer in Molecular Junctions: Effect on Electronic-Structure and Thermopower. *J Phys Chem Lett* **3,** 1962-1967 (2012).

84. Xue, Y. Q., Ratner, M. A. End group effect on electrical transport through individual molecules: A microscopic study. *Phys Rev B* **69,** 085403 (2004).

85. Balachandran, J., Reddy, P., Dunietz, B. D., Gavini, V. End-Group Influence on Frontier Molecular Orbital Reorganization and Thermoelectric Properties of Molecular Junctions. *J Phys Chem Lett* **4,** 3825-3833 (2013).

86. Bilan, S., Zotti, L. A., Pauly, F., Cuevas, J. C. Theoretical study of the charge transport through C-60-based single-molecule junctions. *Phys Rev B* **85,** 205403 (2012).

87. Tan, A., Balachandran, J., Sadat, S., Gavini, V., Dunietz, B. D., *et al.* Effect of length and contact chemistry on the electronic structure and thermoelectric properties of molecular junctions. *J Am Chem Soc* **133,** 8838-8841 (2011).

88. Baheti, K., Malen, J. A., Doak, P., Reddy, P., Jang, S. Y., *et al.* Probing the chemistry of molecular heterojunctions using thermoelectricity. *Nano Lett* **8,** 715-719 (2008).

89. Lee, S. K., Buerkle, M., Yamada, R., Asai, Y., Tada, H. Thermoelectricity at the molecular scale: a large Seebeck effect in endohedral metallofullerenes. *Nanoscale* **7,** 20497-20502 (2015).

90. Rincon-Garcia, L., Ismael, A. K., Evangeli, C., Grace, I., Rubio-Bollinger, G., *et al.* Molecular design and control of fullerene-based bi-thermoelectric materials. *Nat Mater* **15,** 289-293 (2016).

91. Venkataraman, L., Klare, J. E., Nuckolls, C., Hybertsen, M. S., Steigerwald, M. L. Dependence of single-molecule junction conductance on molecular conformation. *Nature* **442,** 904-907 (2006).

92. Mishchenko, A., Vonlanthen, D., Meded, V., Burkle, M., Li, C., *et al.* Influence of Conformation on Conductance of Biphenyl-Dithiol Single-Molecule Contacts. *Nano Lett* **10,** 156-163 (2010).

93. Wang, K., Hamill, J. M., Wang, B., Guo, C. L., Jiang, S. B., *et al.* Structure determined charge transport in single DNA molecule break junctions. *Chem Sci* **5,** 3425-3431 (2014).

94. Yee, S. K., Malen, J. A., Majumdar, A., Segalman, R. A. Thermoelectricity in Fullerene-Metal Heterojunctions. *Nano Lett* **11,** 4089-4094 (2011).

95. Lee, S. K., Ohto, T., Yamada, R., Tada, H. Thermopower of benzenedithiol and C60 molecular junctions with Ni and Au electrodes. *Nano Lett* **14,** 5276-5280 (2014).

96. Evangeli, C., Matt, M., Rincon-Garcia, L., Pauly, F., Nielaba, P., *et al.* Quantum thermopower of metallic atomic-size contacts at room temperature. *Nano Lett* **15,** 1006-1011 (2015).

97. Zerah-Harush, E., Dubi, Y. Enhanced Thermoelectric Performance of Hybrid Nanoparticle-Single-Molecule Junctions. *Phys Rev Appl* **3,** 064017 (2015).

98. Beebe, J. M., Engelkes, V. B., Miller, L. L., Frisbie, C. D. Contact resistance in metal-molecule-metal junctions based on aliphatic SAMs: Effects of surface linker and metal work function. *J Am Chem Soc* **124,** 11268-11269 (2002).

99. Yaliraki, S. N., Kemp, M., Ratner, M. A. Conductance of molecular wires: Influence of molecule-electrode binding. *J Am Chem Soc* **121,** 3428-3434 (1999).

100. Kim, Y., Lenert, A., Meyhofer, E., Reddy, P. Temperature dependence of thermopower in molecular junctions. *Appl Phys Lett* **109,** 033102 (2016).

101. Champagne, A. R., Pasupathy, A. N., Ralph, D. C. Mechanically adjustable and electrically gated single-molecule transistors. *Nano Lett* **5,** 305-308 (2005).

102. Osorio, E. A., Bjornholm, T., Lehn, J. M., Ruben, M., van der Zant, H. S. J. Single-molecule transport in three-terminal devices. *J Phys-Condens Mat* **20,** 374121 (2008).

103. Xiang, D., Jeong, H., Kim, D., Lee, T., Cheng, Y. J., *et al.* Three-Terminal Single-Molecule Junctions Formed by Mechanically Controllable Break Junctions with Side Gating. *Nano Lett* **13,** 2809-2813 (2013).

104. Song, H., Kim, Y., Jang, Y. H., Jeong, H., Reed, M. A., *et al.* Observation of molecular orbital gating. *Nature* **462,** 1039-1043 (2009).

105. Park, H., Lim, A. K. L., Alivisatos, A. P., Park, J., McEuen, P. L. Fabrication of metallic electrodes with nanometer separation by electromigration. *Appl Phys Lett* **75,** 301-303 (1999).

106. Park, J., Pasupathy, A. N., Goldsmith, J. I., Chang, C., Yaish, Y., *et al.* Coulomb blockade and the Kondo effect in single-atom transistors. *Nature* **417,** 722-725 (2002).

107. Maeng, J., Jo, G., Kwon, S. S., Song, S., Seo, J., *et al.* Effect of gate bias sweep rate on the electronic properties of ZnO nanowire field-effect transistors under different environments. *Appl Phys Lett* **92,** 233120 (2008).

108. Osorio, E. A., Moth-Poulsen, K., van der Zant, H. S. J., Paaske, J., Hedegard, P., *et al.* Electrical Manipulation of Spin States in a Single Electrostatically Gated Transition-Metal Complex. *Nano Lett* **10,** 105-110 (2010).

109. Javey, A., Kim, H., Brink, M., Wang, Q., Ural, A., *et al.* High-kappa dielectrics for advanced carbon-nanotube transistors and logic gates. *Nat Mater* **1,** 241-246 (2002).

110. Gabor, N. M., Zhong, Z. H., Bosnick, K., Park, J., McEuen, P. L. Extremely Efficient Multiple Electron-Hole Pair Generation in Carbon Nanotube Photodiodes. *Science* **325,** 1367-1371 (2009).

111. Jarillo-Herrero, P., Kong, J., van der Zant, H. S. J., Dekker, C., Kouwenhoven, L. P., *et al.* Orbital Kondo effect in carbon nanotubes. *Nature* **434,** 484-488 (2005).

112. Jeong, W., Kim, K., Kim, Y., Lee, W., Reddy, P. Characterization of nanoscale temperature fields during electromigration of nanowires (vol 4, 4975, 2014). *Sci Rep-Uk* **4,** 4975 (2014).

113. E. Fermi, J. Pasta, and S. Ulam, Los Alamos Report LA-1940 978 (1955).

114. Segal, D., Nitzan, A., Hanggi, P. Thermal conductance through molecular wires. *J Chem Phys* **119,** 6840-6855 (2003).

115. Sadeghi, H., Sangtarash, S., Lambert, C. J. Oligoyne Molecular Junctions for Efficient Room Temperature Thermoelectric Power Generation. *Nano Lett* **15,** 7467-7472 (2015).

116. Klockner, J. C., Burkle, M., Cuevas, J. C., Pauly, F. Length dependence of the thermal conductance of alkane-based single-molecule junctions: An ab initio study. *Phys Rev B* **94,** 205425 (2016).

117. Lepri, S., Livi, R., Politi, A. Thermal conduction in classical low-dimensional lattices. *Phys Rep* **377,** 1-80 (2003).

118. Dhar, A. Heat transport in low-dimensional systems. *Adv Phys* **57,** 457-537 (2008).

119. Guedon, C. M., Valkenier, H., Markussen, T., Thygesen, K. S., Hummelen, J. C., *et al.* Observation of quantum interference in molecular charge transport. *Nature Nanotechnology* **7,** 304-308 (2012).

120. Markussen, T. Phonon interference effects in molecular junctions. *J Chem Phys* **139,** 244101 (2013).

121. Duda, J. C., Saltonstall, C. B., Norris, P. M., Hopkins, P. E. Assessment and prediction of thermal transport at solid-self-assembled monolayer junctions. *J Chem Phys* **134,** 094704 (2011).

122. Luo, T. F., Lloyd, J. R. Molecular dynamics study of thermal transport in GaAs-self-assembly monolayer-GaAs junctions with ab initio characterization of thiol-GaAs bonds. *J Appl Phys* **109,** 034301 (2011).

123. Luo, T. F., Lloyd, J. R. Non-equilibrium molecular dynamics study of thermal energy transport in Au-SAM-Au junctions. *Int J Heat Mass Tran* **53,** 1-11 (2010).

124. Goicochea, J. V., Hu, M., Michel, B., Poulikakos, D. Surface Functionalization Mechanisms of Enhancing Heat Transfer at Solid-Liquid Interfaces. *J Heat Trans-T Asme* **133,** 082401 (2011).

125. Hu, L., Zhang, L. F., Hu, M., Wang, J. S., Li, B. W., *et al.* Phonon interference at self-assembled monolayer interfaces: Molecular dynamics simulations. *Phys Rev B* **81,** 235427 (2010).

126. Li, N. B., Ren, J., Wang, L., Zhang, G., Hanggi, P., *et al.* Colloquium: Phononics: Manipulating heat flow with electronic analogs and beyond. *Rev Mod Phys* **84,** 1045-1066 (2012).

127. Segal, D., Nitzan, A. Heat rectification in molecular junctions. *J Chem Phys* **122,** 194704 (2005).

128. Segal, D. Heat flow in nonlinear molecular junctions: Master equation analysis. *Phys Rev B* **73,** 205415 (2006).

129. Diaz, E., Gutierrez, R., Cuniberti, G. Heat transport and thermal rectification in molecular junctions: A minimal model approach. *Phys Rev B* **84,** 144302 (2011).

130. Menezes, M. G., Saraiva-Souza, A., Del Nero, J., Capaz, R. B. Proposal for a single-molecule field-effect transistor for phonons. *Phys Rev B* **81,** 012302 (2010).

131. Li, Q., Duchemin, I., Xiong, S. Y., Solomon, G. C., Donadio, D. Mechanical Tuning of Thermal Transport in a Molecular Junction. *J Phys Chem C* **119,** 24636-24642 (2015).

132. Ren, J., Hanggi, P., Li, B. W. Berry-Phase-Induced Heat Pumping and Its Impact on the Fluctuation Theorem. *Phys Rev Lett* **104,** 170601 (2010).

133. Zhan, F., Li, N. B., Kohler, S., Hanggi, P. Molecular wires acting as quantum heat ratchets. *Phys Rev E* **80,** 061115 (2009).

134. Choy, C. L. Thermal-Conductivity of Polymers. *Polymer* **18,** 984-1004 (1977).

135. Freeman, J. J., Morgan, G. J., Cullen, C. A. Thermal-Conductivity of a Single Polymer-Chain. *Phys Rev B* **35,** 7627-7635 (1987).

136. Henry, A., Chen, G. Anomalous heat conduction in polyethylene chains: Theory and molecular dynamics simulations. *Phys Rev B* **79,** 144305 (2009).

137. Sasikumar, K., Keblinski, P. Effect of chain conformation in the phonon transport across a Si-polyethylene single-molecule covalent junction. *J Appl Phys* **109,** 114307 (2011).

138. Wang, R. Y., Segalman, R. A., Majumdar, A. Room temperature thermal conductance of alkanedithiol self-assembled monolayers. *Appl Phys Lett* **89,** 173113 (2006).

139. Kirsanskas, G., Li, Q., Flensberg, K., Solomon, G. C., Leijnse, M. Designing pi-stacked molecular structures to control heat transport through molecular junctions. *Appl Phys Lett* **105,** 233102 (2014).

140. Love, J. C., Estroff, L. A., Kriebel, J. K., Nuzzo, R. G., Whitesides, G. M. Self-assembled monolayers of thiolates on metals as a form of nanotechnology. *Chem Rev* **105,** 1103-1169 (2005).

141. Ge, Z. B., Cahill, D. G., Braun, P. V. Thermal conductance of hydrophilic and hydrophobic interfaces. *Phys Rev Lett* **96,** 186101 (2006).

142. Paddock, C. A., Eesley, G. L. Transient Thermoreflectance from Thin Metal-Films. *J Appl Phys* **60,** 285-290 (1986).

143. Tian, Z. T., Marconnet, A., Chen, G. Enhancing solid-liquid interface thermal transport using self-assembled monolayers. *Appl Phys Lett* **106,** 211602 (2015).

144. Cahill, D. G. Thermal-Conductivity Measurement from 30-K to 750-K - the 3-Omega Method. *Rev Sci Instrum* **61,** 802-808 (1990).

145. O'Brien, P. J., Shenogin, S., Liu, J. X., Chow, P. K., Laurencin, D., *et al.* Bonding-induced thermal conductance enhancement at inorganic heterointerfaces using nanomolecular monolayers. *Nat Mater* **12,** 118-122 (2013).

146. Losego, M. D., Grady, M. E., Sottos, N. R., Cahill, D. G., Braun, P. V. Effects of chemical bonding on heat transport across interfaces. *Nat Mater* **11,** 502-506 (2012).

147. Majumdar, S., Sierra-Suarez, J. A., Schiffres, S. N., Ong, W. L., Higgs, C. F., *et al.* Vibrational Mismatch of Metal Leads Controls Thermal Conductance of Self-Assembled Monolayer Junctions. *Nano Lett* **15,** 2985-2991 (2015).

148. Meier, T., Menges, F., Nirmalraj, P., Holscher, H., Riel, H., *et al.* Length-Dependent Thermal Transport along Molecular Chains. *Phys Rev Lett* **113,** 060801 (2014).

149. Schmidt, A. J., Cheaito, R., Chiesa, M. A frequency-domain thermoreflectance method for the characterization of thermal properties. *Rev Sci Instrum* **80,** 094901 (2009).

150. Shen, S., Henry, A., Tong, J., Zheng, R. T., Chen, G. Polyethylene nanofibres with very high thermal conductivities. *Nature Nanotechnology* **5,** 251-255 (2010).

151. Wang, X. J., Ho, V., Segalman, R. A., Cahill, D. G. Thermal Conductivity of High-Modulus Polymer Fibers. *Macromolecules* **46,** 4937-4943 (2013).

152. Ma, J., Zhang, Q., Mayo, A., Ni, Z. H., Yi, H., *et al.* Thermal conductivity of electrospun polyethylene nanofibers. *Nanoscale* **7,** 16899-16908 (2015).

153. Segal, D., Nitzan, A. Heating in current carrying molecular junctions. *J Chem Phys* **117,** 3915-3927 (2002).

154. Yang, Z., Chshiev, M., Zwolak, M., Chen, Y. C., Di Ventra, M. Role of heating and current-induced forces in the stability of atomic wires. *Phys Rev B* **71,** 041402 (2005).

155. Chen, Y. C., Zwolak, M., Di Ventra, M. Inelastic effects on the transport properties of alkanethiols. *Nano Lett* **5,** 621-624 (2005).

156. Pecchia, A., Romano, G., Di Carlo, A. Theory of heat dissipation in molecular electronics. *Phys Rev B* **75,** 035401 (2007).

157. Galperin, M., Nitzan, A., Ratner, M. A. Heat conduction in molecular transport junctions. *Phys Rev B* **75,** 155312 (2007).

158. D'Agosta, R., Sai, N., Di Ventra, M. Local electron heating in nanoscale conductors. *Nano Lett* **6,** 2935-2938 (2006).

159. Galperin, M., Saito, K., Balatsky, A. V., Nitzan, A. Cooling mechanisms in molecular conduction junctions. *Phys Rev B* **80,** 115427 (2009).

160. Romano, G., Gagliardi, A., Pecchia, A., Di Carlo, A. Heating and cooling mechanisms in single-molecule junctions. *Phys Rev B* **81,** 115438 (2010).

161. Hartle, R., Thoss, M. Resonant electron transport in single-molecule junctions: Vibrational excitation, rectification, negative differential resistance, and local cooling. *Phys Rev B* **83,** 115414 (2011).

162. Simine, L., Segal, D. Vibrational cooling, heating, and instability in molecular conducting junctions: full counting statistics analysis. *Phys Chem Chem Phys* **14,** 13820-13834 (2012).

163. Lykkebo, J., Romano, G., Gagliardi, A., Pecchia, A., Solomon, G. C. Single-molecule electronics: Cooling individual vibrational modes by the tunneling current. *J Chem Phys* **144,** 114310 (2016).

164. Huang, Z. F., Xu, B. Q., Chen, Y. C., Di Ventra, M., Tao, N. J. Measurement of current-induced local heating in a single molecule junction. *Nano Lett* **6,** 1240-1244 (2006).

165. Tsutsui, M., Taninouchi, Y., Kurokawa, S., Sakai, A. Effective temperature of Au nanocontacts under high biases. *Jpn J Appl Phys 1* **44,** 5188-5190 (2005).

166. Tsutsui, M., Kurokawa, S., Sakai, A. Bias-induced local heating in Au atom-sized contacts. *Nanotechnology* **17,** 5334-5338 (2006).

167. Tsutsui, M., Taniguchi, M., Kawai, T. Local Heating in Metal-Molecule-Metal Junctions. *Nano Lett* **8,** 3293-3297 (2008).

168. Reed, M. A. Inelastic electron tunneling spectroscopy. *Mater Today* **11,** 46-50 (2008).

169. Huang, Z. F., Chen, F., D'Agosta, R., Bennett, P. A., Di Ventra, M., *et al.* Local ionic and electron heating in single-molecule junctions. *Nature Nanotechnology* **2,** 698-703 (2007).

170. Ward, D. R., Corley, D. A., Tour, J. M., Natelson, D. Vibrational and electronic heating in nanoscale junctions. *Nature Nanotechnology* **6,** 33-38 (2011).

171. Ioffe, Z., Shamai, T., Ophir, A., Noy, G., Yutsis, I., *et al.* Detection of heating in current-carrying molecular junctions by Raman scattering. *Nature Nanotechnology* **3,** 727-732 (2008).

172. Schulze, G., Franke, K. J., Gagliardi, A., Romano, G., Lin, C. S., *et al.* Resonant electron heating and molecular phonon cooling in single C-60 junctions. *Phys Rev Lett* **100,** 136801 (2008).

173. Lee, W., Kim, K., Jeong, W., Zotti, L. A., Pauly, F., *et al.* Heat dissipation in atomic-scale junctions. *Nature* **498,** 209-+ (2013).

174. Cui, L., Jeong, W., Hur, S., Matt, M., Klockner, J. C., *et al.* Quantized thermal transport in single-atom junctions. *Science* **355,** 1192-1195 (2017).

175. Pop, E. Energy Dissipation and Transport in Nanoscale Devices. *Nano Res* **3,** 147-169 (2010).

176. Cahill, D. G., Braun, P. V., Chen, G., Clarke, D. R., Fan, S. H., *et al.* Nanoscale thermal transport. II. 2003-2012. *Appl Phys Rev* **1,** 011305 (2014).

177. Crossno, J., Shi, J. K., Wang, K., Liu, X. M., Harzheim, A., *et al.* Observation of the Dirac fluid and the breakdown of the Wiedemann-Franz law in graphene. *Science* **351,** 1058-1061 (2016).

178. Cuevas, J. C., Scheer, E. *Molecular electronics : an introduction to theory and experiment*. World Scientific: Singapore ; Hackensack, NJ, 2010.

179. Scheer, E., Agrait, N., Cuevas, J. C., Yeyati, A. L., Ludoph, B., *et al.* The signature of chemical valence in the electrical conduction through a single-atom contact. *Nature* **394,** 154-157 (1998).

180. van den Brom, H. E., van Ruitenbeek, J. M. Quantum suppression of shot noise in atom-size metallic contacts. *Phys Rev Lett* **82,** 1526-1529 (1999).

181. Wheeler, P. J., Russom, J. N., Evans, K., King, N. S., Natelson, D. Shot Noise Suppression at Room Temperature in Atomic-Scale Au Junctions. *Nano Lett* **10,** 1287-1292 (2010).

182. Schwab, K., Henriksen, E. A., Worlock, J. M., Roukes, M. L. Measurement of the quantum of thermal conductance. *Nature* **404,** 974-977 (2000).

183. Chiatti, O., Nicholls, J. T., Proskuryakov, Y. Y., Lumpkin, N., Farrer, I., *et al.* Quantum thermal conductance of electrons in a one-dimensional wire. *Phys Rev Lett* **97,** 056601 (2006).

184. Meschke, M., Guichard, W., Pekola, J. P. Single-mode heat conduction by photons. *Nature* **444,** 187-190 (2006).

185. Jezouin, S., Parmentier, F. D., Anthore, A., Gennser, U., Cavanna, A., *et al.* Quantum Limit of Heat Flow Across a Single Electronic Channel. *Science* **342,** 601-604 (2013).

186. Partanen, M., Tan, K. Y., Govenius, J., Lake, R. E., Makela, M. K., *et al.* Quantum-limited heat conduction over macroscopic distances. *Nat Phys* **12,** 460-464 (2016).

187. Gotsmann, B., Lantz, M. A. Quantized thermal transport across contacts of rough surfaces. *Nat Mater* **12,** 59-65 (2013).

188. Sadat, S., Meyhofer, E., Reddy, P. High resolution resistive thermometry for micro/nanoscale measurements. *Rev Sci Instrum* **83,** 084902 (2012).

189. Sadat, S., Meyhofer, E., Reddy, P. Resistance thermometry-based picowatt-resolution heat-flow calorimeter. *Appl Phys Lett* **102,** 163110 (2013).

190. Olesen, L., Laegsgaard, E., Stensgaard, I., Besenbacher, F., Schiotz, J., *et al.* Quantized Conductance in an Atom-Sized Point-Contact. *Phys Rev Lett* **72,** 2251-2254 (1994).

191. Krans, J. M., Muller, C. J., Vanderpost, N., Postma, F. R., Sutton, A. P., *et al.* Quantized Conductance in an Atom-Sized Point-Contact - Comment. *Phys Rev Lett* **74,** 2146-2146 (1995).

192. Olesen, L., Laegsgaard, E., Stensgaard, I., Besenbacher, F., Schiotz, J., *et al.* Quantized Conductance in an Atom-Sized Point-Contact - Reply. *Phys Rev Lett* **74,** 2147-2147 (1995).

193. Ashcroft, N. W., Mermin, N. D. *Solid state physics*. Holt: New York,, 1976.

194. Dreher, M., Pauly, F., Heurich, J., Cuevas, J. C., Scheer, E., *et al.* Structure and conductance histogram of atomic-sized Au contacts. *Phys Rev B* **72,** 075435 (2005).

195. Schirm, C., Matt, M., Pauly, F., Cuevas, J. C., Nielaba, P., *et al.* A current-driven single-atom memory. *Nature Nanotechnology* **8,** 645-648 (2013).

196. Pauly, F., Viljas, J. K., Huniar, U., Hafner, M., Wohlthat, S., *et al.* Cluster-based density-functional approach to quantum transport through molecular and atomic contacts. *New J Phys* **10,** 125019 (2008).

197. Jain, A., McGaughey, A. J. H. Thermal transport by phonons and electrons in aluminum, silver, and gold from first principles. *Phys Rev B* **93,** 081206 (2016).

198. Cui, L., Jeong, W., Fernandez-Hurtado, V., Feist, J., Garcia-Vidal, F. J., *et al.* Study of radiative heat transfer in Angstrom- and nanometre-sized gaps. *Nat Commun* **9,** 14479 (2018).

199. Balachandran, V., Bosisio, R., Benenti, G. Validity of the Wiedemann-Franz law in small molecular wires. *Phys Rev B* **86,** (2012).

200. Song, B., Ganjeh, Y., Sadat, S., Thompson, D., Fiorino, A., *et al.* Enhancement of near-field radiative heat transfer using polar dielectric thin films. *Nature Nanotechnology* **10,** 253-258 (2015).

201. Khan, A., Philip, J., Hess, P. Young's modulus of silicon nitride used in scanning force microscope cantilevers. *J Appl Phys* **95,** 1667-1672 (2004).

202. Olesen, L., Brandbyge, M., Sorensen, M. R., Jacobsen, K. W., Laegsgaard, E., *et al.* Apparent barrier height in scanning tunneling microscopy revisited. *Phys Rev Lett* **76,** 1485-1488 (1996).

203. Reecht, G., Scheurer, F., Speisser, V., Dappe, Y. J., Mathevet, F., *et al.* Electroluminescence of a Polythiophene Molecular Wire Suspended between a Metallic Surface and the Tip of a Scanning Tunneling Microscope. *Phys Rev Lett* **112,** (2014).

204. Cui, L., Miao, R., Wang, K., Thompson, D., Zotti, L. A., *et al.* Peltier cooling in molecular junctions. *Nature Nanotechnology* **13,** 122-127 (2018).

205. Garner, M. H., Li, H. X., Chen, Y., Su, T. A., Shangguan, Z., *et al.* Comprehensive suppression of single-molecule conductance using destructive sigma-interference. *Nature* **558,** 415-+ (2018).

206. Miao, R., Xu, H., Skripnik, M., Cui, L., Wang, K., *et al.* Influence of Quantum Interference on the Thermoelectric Properties of Molecular Junctions. *Nano Lett* (2018).

207. Xu, Y. F., Wang, X. X., Zhou, J. W., Song, B., Jiang, Z., *et al.* Molecular engineered conjugated polymer with high thermal conductivity. *Sci Adv* **4,** (2018).

208. Jang, S. Y., Reddy, P., Majumdar, A., Segalman, R. A. Interpretation of Stochastic events in single molecule conductance measurements. *Nano Lett* **6,** 2362-2367 (2006).

209. Callen, H. B. *Thermodynamics; an introduction to the physical theories of equilibrium thermostatics and irreversible thermodynamics*. Wiley: New York,, 1960.

210. Rowe, D. M. *Thermoelectrics handbook : macro to nano*. CRC/Taylor & Francis: Boca Raton, 2006.

211. Wold, D. J., Frisbie, C. D. Fabrication and characterization of metal-molecule-metal junctions by conducting probe atomic force microscopy. *J Am Chem Soc* **123,** 5549-5556 (2001).

212. Choi, S. H., Kim, B., Frisbie, C. D. Electrical resistance of long conjugated molecular wires. *Science* **320,** 1482-1486 (2008).

213. Quek, S. Y., Venkataraman, L., Choi, H. J., Louie, S. G., Hybertsen, M. S., *et al.* Amine-gold linked single-molecule circuits: Experiment and theory. *Nano Lett* **7,** 3477-3482 (2007).

214. Klöckner, J. C., Siebler, R., Cuevas, J. C., Pauly, F. Thermal conductance and thermoelectric figure of merit of C-60-based single-molecule junctions: Electrons, phonons, and photons. *Phys Rev B* **95,** 245404 (2017).

215. Lin, S. F., Leonard, W. F. Thermoelectric Power of Thin Gold Films. *J Appl Phys* **42,** 3634-3639 (1971).

216. Ahlrichs, R., Bar, M., Haser, M., Horn, H., Kolmel, C. Electronic-Structure Calculations on Workstation Computers - the Program System Turbomole. *Chem Phys Lett* **162,** 165-169 (1989).

217. Perdew, J. P. Density-Functional Approximation for the Correlation-Energy of the Inhomogeneous Electron-Gas. *Phys Rev B* **33,** 8822-8824 (1986).

218. Schafer, A., Horn, H., Ahlrichs, R. Fully Optimized Contracted Gaussian-Basis Sets for Atoms Li to Kr. *J Chem Phys* **97,** 2571-2577 (1992).

219. Frank, I. W., Tanenbaum, D. M., Van der Zande, A. M., McEuen, P. L. Mechanical properties of suspended graphene sheets. *J Vac Sci Technol B* **25,** 2558-2561 (2007).

220. Henderson, J. I., Feng, S., Bein, T., Kubiak, C. P. Adsorption of diisocyanides on gold. *Langmuir* **16,** 6183-6187 (2000).

221. Frey, S., Stadler, V., Heister, K., Eck, W., Zharnikov, M., *et al.* Structure of thioaromatic self-assembled monolayers on gold and silver. *Langmuir* **17,** 2408-2415 (2001).

222. Lu, Q., Liu, K., Zhang, H. M., Du, Z. B., Wang, X. H., *et al.* From Tunneling to Hopping: A Comprehensive Investigation of Charge Transport Mechanism in Molecular Junctions Based on Oligo(p-phenylene ethynylene)s. *Acs Nano* **3,** 3861-3868 (2009).

223. Bain, C. D., Whitesides, G. M. Attenuation lengths of photoelectrons in hydrocarbon films. *J Phys Chem-Us* **93,** 1670-1673 (1989).

224. Azzam, W., Wehner, B. I., Fischer, R. A., Terfort, A., Woll, C. Bonding and orientation in self-assembled monolayers of oligophenyldithiols on Au substrates. *Langmuir* **18,** 7766-7769 (2002).

225. Kamenetska, M., Quek, S. Y., Whalley, A. C., Steigerwald, M. L., Choi, H. J., *et al.* Conductance and Geometry of Pyridine-Linked Single-Molecule Junctions. *J Am Chem Soc* **132,** 6817-6821 (2010).

226. Diao, Y. X., Han, M. J., Wan, L. J., Itaya, K., Uchida, T., *et al.* Adsorbed structures of 4,4 '-bipyridine on Cu(111) in acid studied by STM and IR. *Langmuir* **22,** 3640-3646 (2006).

227. Johnson, K. L. *Contact mechanics*: Cambridge University Press, 1985.

228. Whelan, C. M., Smyth, M. R., Barnes, C. J. HREELS, XPS, and electrochemical study of benzenethiol adsorption on Au(111). *Langmuir* **15,** 116-126 (1999).

229. Johnson, K. L., Kendall, K., Roberts, A. D. Surface Energy and Contact of Elastic Solids. *Proc R Soc Lon Ser-A* **324,** 301-& (1971).

230. Guo, S. Y., Zhou, G., Tao, N. J. Single Molecule Conductance, Thermopower, and Transition Voltage. *Nano Lett* **13,** 4326-4332 (2013).

231. Kim, K., Song, B., Fernandez-Hurtado, V., Lee, W., Jeong, W. H., *et al.* Radiative heat transfer in the extreme near field. *Nature* **528,** 387-391 (2015).

232. Worbes, L., Hellmann, D., Kittel, A. Enhanced Near-Field Heat Flow of a Monolayer Dielectric Island. *Phys Rev Lett* **110,** 134302 (2013).

233. St-Gelais, R., Zhu, L. X., Fan, S. H., Lipson, M. Near-field radiative heat transfer between parallel structures in the deep subwavelength regime. *Nature Nanotechnology* **11,** 515-519 (2016).

234. Basu, S., Zhang, Z. M., Fu, C. J. Review of near-field thermal radiation and its application to energy conversion. *Int J Energ Res* **33,** 1203-1232 (2009).

235. De Wilde, Y., Formanek, F., Carminati, R., Gralak, B., Lemoine, P. A., *et al.* Thermal radiation scanning tunnelling microscopy. *Nature* **444,** 740-743 (2006).

236. Kittel, A., Muller-Hirsch, W., Parisi, J., Biehs, S. A., Reddig, D., *et al.* Near-field heat transfer in a scanning thermal microscope. *Phys Rev Lett* **95,** 224301 (2005).

237. Kloppstech, K., Konne, N., Beihs, S.-A., Rodriguez, A. W., Worbes, L., *et al.* Giant near-field mediated heat flux at the nanometer scale. *arXiv:151006311*.

238. Rytov, S. M., Kravtsov, I. A., Tatarskii, V. I. *Principles of statistical radiophysics*, 2. rev. and enl. edn. Springer-Verlag: Berlin ; New York, 1987.

239. Rodriguez, A. W., Reid, M. T. H., Johnson, S. G. Fluctuating-surface-current formulation of radiative heat transfer: Theory and applications. *Phys Rev B* **88,** 054305 (2013).

240. Song, B., Thompson, D., Fiorino, A., Ganjeh, Y., Reddy, P., *et al.* Radiative heat conductances between dielectric and metallic parallel plates with nanoscale gaps. *Nature Nanotechnology* **11,** 509-514 (2016).

241. Ottens, R. S., Quetschke, V., Wise, S., Alemi, A. A., Lundock, R., *et al.* Near-Field Radiative Heat Transfer between Macroscopic Planar Surfaces. *Phys Rev Lett* **107,** 014301 (2011).

242. Lim, M., Lee, S. S., Lee, B. J. Near-field thermal radiation between doped silicon plates at nanoscale gaps. *Phys Rev B* **91,** 195136 (2015).

243. Ito, K., Miura, A., Iizuka, H., Toshiyoshi, H. Parallel-plate submicron gap formed by micromachined low-density pillars for near-field radiative heat transfer. *Appl Phys Lett* **106,** 083504 (2015).

244. Polder, D., Vanhove, M. Theory of Radiative Heat Transfer between Closely Spaced Bodies. *Phys Rev B* **4,** 3303 (1971).

245. Jones, A. C., Raschke, M. B. Thermal Infrared Near-Field Spectroscopy. *Nano Lett* **12,** 1475-1481 (2012).

246. Challener, W. A., Peng, C. B., Itagi, A. V., Karns, D., Peng, W., *et al.* Heat-assisted magnetic recording by a near-field transducer with efficient optical energy transfer. *Nat Photonics* **3,** 220-224 (2009).

247. Cui, L., Huang, Y., Wang, J. Near-field radiative heat transfer between chiral metamaterials. *J Appl Phys* **112,** (2012).

248. Cui, L., Huang, Y., Wang, J., Zhu, K. Y. Ultrafast modulation of near-field heat transfer with tunable metamaterials. *Appl Phys Lett* **102,** (2013).

249. Otey, C. R., Lau, W. T., Fan, S. H. Thermal Rectification through Vacuum. *Phys Rev Lett* **104,** (2010).

250. Pendry, J. B. Radiative exchange of heat between nanostructures. *J Phys-Condens Mat* **11,** 6621-6633 (1999).

251. Joulain, K., Mulet, J. P., Marquier, F., Carminati, R., Greffet, J. J. Surface electromagnetic waves thermally excited: Radiative heat transfer, coherence properties and Casimir forces revisited in the near field. *Surf Sci Rep* **57,** 59-112 (2005).

252. Rousseau, E., Siria, A., Jourdan, G., Volz, S., Comin, F., *et al.* Radiative heat transfer at the nanoscale. *Nat Photonics* **3,** 514-517 (2009).

253. Shen, S., Narayanaswamy, A., Chen, G. Surface Phonon Polaritons Mediated Energy Transfer between Nanoscale Gaps. *Nano Lett* **9,** 2909-2913 (2009).

254. Chapuis, P. O., Volz, S., Henkel, C., Joulain, K., Greffet, J. J. Effects of spatial dispersion in near-field radiative heat transfer between two parallel metallic surfaces. *Phys Rev B* **77,** 035431 (2008).

255. Singer, F., Ezzahri, Y., Joulain, K. Near field radiative heat transfer between two nonlocal dielectrics. *J Quant Spectrosc Ra* **154,** 55-62 (2015).

256. Chiloyan, V., Garg, J., Esfarjani, K., Chen, G. Transition from near-field thermal radiation to phonon heat conduction at sub-nanometre gaps. *Nat Commun* **6,** (2015).

257. Kim, K., Jeong, W. H., Lee, W. C., Reddy, P. Ultra-High Vacuum Scanning Thermal Microscopy for Nanometer Resolution Quantitative Thermometry. *Acs Nano* **6,** 4248-4257 (2012).

258. Kim, K., Jeong, W., Lee, W., Sadat, S., Thompson, D., *et al.* Quantification of thermal and contact resistances of scanning thermal probes. *Appl Phys Lett* **105,** 203107 (2014).

259. Untiedt, C., Caturla, M. J., Calvo, M. R., Palacios, J. J., Segers, R. C., *et al.* Formation of a metallic contact: Jump to contact revisited. *Phys Rev Lett* **98,** 206801 (2007).

260. Sabater, C., Caturla, M. J., Palacios, J. J., Untiedt, C. Understanding the structure of the first atomic contact in gold. *Nanoscale Res Lett* **8,** 257 (2013).

261. Chen, C. J. *Introduction to scanning tunneling microscopy*, 2nd edn. Oxford University Press: Oxford ; New York, 2008.

262. Raiber, K., Terfort, A., Benndorf, C., Krings, N., Strehblow, H. H. Removal of self-assembled monolayers of alkanethiolates on gold by plasma cleaning. *Surf Sci* **595,** 56-63 (2005).

263. Vij, D. R. *Handbook of applied solid state spectroscopy*. Springer: New York, 2006.

264. Rodriguez, A. W., Reid, M. T. H., Johnson, S. G. Fluctuating-surface-current formulation of radiative heat transfer for arbitrary geometries. *Phys Rev B* **86,** 220302 (2012).

265. Reid, M. T. H., Johnson, S. G. Efficient computation of power, force and torque in BEM scattering calculations. *IEEE T Antenn Propag* **63,** 3588-3598 (2015).

266. Ordal, M. A., Long, L. L., Bell, R. J., Bell, S. E., Bell, R. R., *et al.* Optical-Properties of the Metals Al, Co, Cu, Au, Fe, Pb, Ni, Pd, Pt, Ag, Ti, and W in the Infrared and Far Infrared. *Appl Optics* **22,** 1099-1119 (1983).